

2

AD-A244 636



Technical Report  
923

# An Experimental Spatial Acquisition and Tracking System for Optical Intersatellite Crosslinks

D.J. Bernays  
E.P. Colagiuri-Cafarelli

3 December 1991

**Lincoln Laboratory**

MASSACHUSETTS INSTITUTE OF TECHNOLOGY

LEXINGTON, MASSACHUSETTS

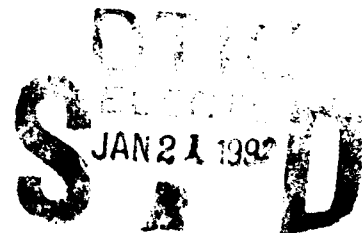


92-01597



Prepared for the Department of the Air Force  
under Contract F19628-90-C-0002.

Approved for public release; distribution is unlimited.



92 1 17 023

This report is based on studies performed at Lincoln Laboratory, a center for research operated by Massachusetts Institute of Technology. The work was sponsored by the Department of the Air Force under Contract F19628-90-C-0002.

This report may be reproduced to satisfy needs of U.S. Government agencies.

The ESD Public Affairs Office has reviewed this report, and it is releasable to the National Technical Information Service, where it will be available to the general public, including foreign nationals.

This technical report has been reviewed and is approved for publication.

FOR THE COMMANDER

*Hugh L. Southall*

Hugh L. Southall, Lt. Col., USAF  
Chief, ESD Lincoln Laboratory Project Office

Non-Lincoln Recipients

PLEASE DO NOT RETURN

Permission is given to destroy this document  
when it is no longer needed.

MASSACHUSETTS INSTITUTE OF TECHNOLOGY  
LINCOLN LABORATORY

**AN EXPERIMENTAL SPATIAL ACQUISITION  
AND TRACKING SYSTEM FOR  
OPTICAL INTERSATELLITE CROSSLINKS**

*D.J. BERNAYS*

*Group 42*

*E.P. COLAGIURI-CAFARELLI*

*Group 67*

TECHNICAL REPORT 923

3 DECEMBER 1991

Approved for public release; distribution is unlimited.

LEXINGTON

MASSACHUSETTS



## ACKNOWLEDGMENTS

This project was the culmination of several years of work. We are happy to thank Kim Winick, Gary Carter, and Dave McDonough for the initial studies, theoretical and experimental, which were the underpinnings for this project. Bob Taylor was responsible for building much of the low frequency electronics, while Dave Hodsdon, Doug White, Bob Parr, and Dave Materna from Group 63 designed, built, and tested the spatial tracking demodulator. In addition, thanks are due to Doug Marquis for help with the software, and John Kaufmann for considerable help on the system analysis. Finally, we thank Don Boroson, Eric Swanson, Roy Bondurant, Lori Jeromin, Steve Alexander, Fred Walther, Emily Kintzer, Sergio Cafarelli, and Vincent Chan for many encouraging and insightful discussions throughout this work.

## TABLE OF CONTENTS

Abstract	iii
Acknowledgments	v
List of Illustrations	ix
List of Tables	xi
1. INTRODUCTION	1
2. OVERVIEW OF LITE	3
2.1 LITE Acquisition Sequence Definition	3
2.2 LITE Link Budgets for GEO to LEO Acquisition, Spatial Tracking, and Communications	4
2.3 Microjitter Angular Disturbance Spectra	6
3. SPATIAL ACQUISITION AND TRACKING SYSTEM REQUIREMENTS	9
3.1 Acquisition System Requirements	9
3.2 Spatial Tracking System Requirements	9
4. SYSTEM OVERVIEW	11
5. OPTICAL LAYOUT COMMON TO BOTH ACQUISITION AND TRACKING SUBSYSTEMS	13
5.1 Signal Simulation	13
5.2 Jitter Simulation and Tracking Mirrors	13
5.3 Acquisition/Tracking Beam Switch	15
6. SPATIAL ACQUISITION SYSTEM IMPLEMENTATION	17
6.1 Acquisition System Overview	17
6.2 Spatial Acquisition System Laboratory Optical Layout	18
6.3 Acquisition Algorithm	18
6.4 Electronics	21
7. SPATIAL ACQUISITION SYSTEM THEORY OF OPERATION	29
7.1 Algorithm: to Obtain Subpixel Resolution	29
7.2 Probability of Error in Acquisition	32
7.3 Effects of Jitter	
8. SPATIAL ACQUISITION SYSTEM RESULTS	41
8.1 Signal Angle of Arrival vs Detected CCD Position	41
8.2 System Gain	41
8.3 Centroid Algorithm Gain Determination	41

8.4	Acquisition Sensor Noise Sources	45
8.5	Acquisition Range	48
8.6	Probability of Acquisition	48
8.7	Jitter	49
9.	HETERODYNE SPATIAL TRACKING SYSTEM	51
9.1	Heterodyne Receiver and Spatial Tracking Optical Elements	51
9.2	Detector/Preamps	51
9.3	Spatial Tracking Demodulator	52
9.4	Baseband Servo Electronics	54
9.5	Handoff Circuitry	54
9.6	Communications Link	57
10.	THEORY OF OPERATION FOR THE HETERODYNE SPATIAL TRACKER	59
10.1	Definition of Geometry	59
10.2	Derivation of IF Heterodyne Currents	59
10.3	Correlation-Based Tracking Discriminant Near Boresight	62
10.4	Noise Equivalent Angle for Commutated, Correlated Processor	65
10.5	Effects of LO Angular Disturbances	65
11.	SPATIAL TRACKER AND HANDOFF RESULTS	69
11.1	Beam Characterization	69
11.2	CNR vs Signal Optical Power	69
11.3	Near Boresight Discriminant Gain and Bias	73
11.4	Off Axis Discriminant Shape	76
11.5	Measured NEA in the Commutation Correlation Processor	76
11.6	Comparison of NEAs Achievable with Other Processing Architectures	81
11.7	Closed Loop Tracking and Disturbance Rejection	83
11.8	BER vs Optical Power, Jitter	87
11.9	Handoff Characterization	88
12.	CONCLUSIONS	99
	APPENDIX A. TORQUE MOTOR BEAM STEERER CONTROL	101
	APPENDIX B. CCD PRIMER	107
	APPENDIX C. DERIVATION OF NEA FOR COMMUTATING, CORRELATION TRACKER	113
	APPENDIX D. LIST OF ACRONYMS AND SYMBOLS	119
	REFERENCES	123

## LIST OF ILLUSTRATIONS

Figure No.		Page
1	GEO-LEO link acquisition sequence.	4
2	(a) PSD of jitter spectrum. (b) PSD of ACTS jitter spectral components.	7
3	Coherent receiver with integrated acquisition and tracking subsystems.	13
4	Optical layout for demonstration system.	14
5	Spatial acquisition using focal plane array.	17
6	CCD modes of operation.	19
7	Acquisition sequence.	20
8	Spatial acquisition subsystem block diagram.	21
9	CCD fixture.	24
10	CCD FET output.	25
11	Digital processing unit block diagram.	26
12	Maxblock geometry.	30
13	Calculated CCD sensor output vs focal plane translation, for a variety of gains and for several spot sizes.	31
14	Calculated CCD sensor output vs focal plane translation, for several airy distributions, and several gains.	33
15	(a) Calculated mean square error vs gain (K). (b) Calculated peak error vs gain (K).	34
16	Maxblock sum vs jitter amplitude.	39
17	Measured CCD-sensed-position vs disturbance mirror angle.	42
18	Measured maxblock sum vs signal arrival rate.	43
19	Measured CCD linearity for small ( $<2$ bw) angular motions.	44
20	Measured noise floor without pixel masking.	46
21	Measured probability of acquisition error, masked and unmasked.	47
22	Theoretical vs measured probability of acquisition error.	48
23	Effect of jitter on measured signal power.	50
24	Commutated correlation demodulator architecture.	53
25	Spatial tracking compensator block diagram.	55
26	Handoff spiral scan.	57

## LIST OF ILLUSTRATIONS (Continued)

Figure No.		Page
27	Geometry for heterodyne detection in the pupil plane.	60
28	Sum channel magnitude and tracking discriminant vs angular error.	63
29	Effects of LO motion on focal plane and pupil plane spatial trackers.	67
30	(a) LO beam profile, vertical. (b) LO beam profile, horizontal.	70
31	(a) Signal beam profile, vertical. (b) Signal beam profile, horizontal.	71
32	LO, signal beam wavefront optical phase distribution.	72
33	Communications channel carrier-to-noise ratio vs photon arrival rate.	74
34	(a) Small signal azimuth tracking discriminant. (b) Small signal elevation tracking discriminant.	75
35	(a) Large signal tracking Az discriminant at high signal photon arrival rate. (b) Large signal tracking Az discriminant at budgeted signal photon arrival rate. (c) Large signal tracking Az discriminant with averaging, at high signal photon arrival rate. (d) Large signal Az tracking discriminant, at budget signal photon arrival rate with averaging. (e) Large signal elevation tracking discriminant, with averaging at high photon arrival rate. (f) Large signal elevation tracking discriminant with averaging at budget photon arrival rate.	77
36	(a) NEA vs signal photon arrival rate, elevation. (b) NEA vs signal photon arrival rate, azimuth.	80
37	Comparison of NEAs for various processing architectures.	82
38	Set-up to measure closed loop transfer function and rejection ratio.	83
39	(a) Closed loop input/output transfer function, elevation, (b) Closed loop input/output transfer function, azimuth.	84
40	(a) Rejection ratio, elevation. (b) Rejection ratio, azimuth.	85
41	Residual jitter for open loop, closed loop systems.	86
42	IF spectrum for binary FSK signaling.	87
43	BER vs communications channel signal photon arrival rate.	88
44	(a) Spiral scan, no noise. (b) Az, EL drive signal for spiral scan. (c) Spiral scan with noise.	90
45	(a) Handoff spiral scan with tracking disabled (limited authority tracker). (b) Comparison of limited and full authority tracker.	94
46	(a) Effects of positive feedback on pull-in transient. (b) Effects of positive feedback on pull-in transient.	95
47	Improvement of pull-in transient by adjusting tracker authority limit.	96

## LIST OF ILLUSTRATIONS (Continued)

Figure No.		Page
48	(a) Pull-in trajectory with 0.4 bw/axis rms noise, budget input signal power. (b) Pull-in trajectory with 0.4 bw/axis rms noise, budget + 10 db signal input power.	97
49	(a) Pull-in trajectory with 2.1 bw/axis rms noise, budget signal power. (b) Pull-in trajectory with 2.1 bw/axis rms noise budget + 10 dB input signal power.	98
A-1	TMBS shaft position sensor.	102
A-2	Shaft position sensor demodulator.	103
A-3	TMBS shaft position sensor calibration.	104
A-4	TMBS current driver.	105
A-5	TMBS shaft angle vs drive current.	105
B-1	Angle-to-position conversion.	107
B-2	CCD drive voltage timing diagra.	108
B-3	CCD architectures.	110

## LIST OF TABLES

Table No.		Page
1	Link Budget for GEO-LEO Downlink Spatial Acquisition, Tracking and Communications	5
2	Spatial Tracking Requirements	9
3	CCD Characteristics	23

## 1. INTRODUCTION

Optical crosslinks between spaceborne platforms are attractive because they offer the potential of supporting high-data-rate communications (greater than 1 Gb/s) using small-aperture telescopes and with less weight and power than microwave-based links. However, the narrow beamwidth achievable at optical wavelengths ( $\sim 1 \mu\text{m}$ ) compared to microwave wavelengths ( $\sim 1 \text{ cm}$ ) demands highly accurate spatial acquisition and tracking to obtain good communication performance.

During acquisition a communication satellite may have attitude angular uncertainties of the order of 1 mrad, yet the full-width half-maximum field of view (FOV) of a diffraction-limited receiver is only  $4.4 \mu\text{rad}$  when using a 20-cm aperture at diode-laser wavelengths ( $\sim 0.86 \mu\text{m}$ ). Broadening the transmitted beam increases the probability of illuminating the receiver for acquisition, despite initial transmitter pointing errors, but reduces signal power at the receiver. As we will show, acquisition for a realistic optical link may entail searching more than  $10^4$  locations in less than a minute for a signal that has a photon arrival rate on the order of only  $10^5$  photons/s.

In addition to acquisition, angle tracking of a received signal is important to space-based laser communications systems. Typically, the input signal optical power required to maintain constant bit error rate (BER) in a heterodyne optical communications link increases drastically as the single axis tracking (tilt) errors exceed 0.3 to 0.5 beamwidth (bw). Because transient spatial tracking errors last for many symbol times in a high-speed communications system, relatively infrequent errors of this magnitude can significantly degrade the link BER. Studies have shown that the probability of burst errors must be reduced to a level similar to the desired probability of bit error in order to realize the desired BER in the presence of statistical tracking errors [1,2,3]. This may be achieved by reducing the sum of tracking biases and the rms level of tracking jitter to approximately 0.05 to 0.1 bw.

This report describes a design for an integrated acquisition and spatial tracking system that forms part of a high-speed optical heterodyne communications receiver. The baseline design is a receiver that could realistically serve as the low-earth-orbit (LEO) end of a geosynchronous orbit (GEO) to LEO communications link. The design was originally intended to be the ground receiver for Phase I, GEO to ground, of the Laser Intersatellite Transmission Experiment (LITE). First this report presents an overview of LITE and the requirements that the LEO receiver acquisition and tracking system must satisfy to support the communications link of which it is a part. Next, the acquisition and tracking portions of the system implementation are described in detail. Within each discussion data are presented to verify the performance of the acquisition and tracking subsystems in a laboratory breadboard of the receiver. A list of acronyms and symbols is included as Appendix D.

## 2. OVERVIEW OF LITE

The potential advantages of an optical intersatellite crosslink over microwave-based systems have been the subject of considerable research for several years at MIT Lincoln Laboratory and elsewhere. In 1985 MIT Lincoln Laboratory began the design for LITE [4]. The initial phase of this experiment was to demonstrate optical communications between a spaceborne package on the NASA Advanced Communications Technology Satellite (ACTS) and a ground-based heterodyne detection receiver at an astronomical site in the United States (probably Mt. Wilson). Subsequent phases would have demonstrated GEO-LEO and GEO-GEO communications links. Although the flight portion of LITE was cancelled due to funding constraints, an engineering model of the spaceborne platform is under development, and a laboratory demonstration of the heterodyne receiver intended for either ground or LEO has been completed. This report details the spatial acquisition and tracking portion of the LEO receiver. It includes a summary of the important GEO platform design features to help put the LEO receiver design in context. A more complete description of the GEO spatial acquisition, tracking, and pointing system may be found in Bondurant et al., and Kaufman and Swanson [5,6].

LITE included an intensity modulated (54 kHz, 50 percent duty cycle square wave) uplink beacon from the LEO platform to the direct detection ACTS receiver located in GEO. This beacon provided a tracking reference for the ACTS-based platform, which returned a constant amplitude, 2- or 4-ary, frequency shift keyed (FSK) modulated downlink to the heterodyne detection LEO receiver. The data rate on the downlink could be set to 27.5, 55, 110, or 220 Mb/s. Both ends of the communications link employed 30-mW semiconductor lasers operating at nominal wavelengths of 0.86  $\mu\text{m}$ . LITE included a demonstration of direct detection acquisition and spatial tracking of the uplink beacon by the GEO platform and a simultaneous demonstration of acquisition, spatial tracking, and data demodulation of the downlink by the LEO receiver.

### 2.1 LITE ACQUISITION SEQUENCE DEFINITION

The following acquisition sequence, illustrated in Figure 1, was developed to establish a communications link between the LEO and GEO terminals. First, the GEO transmitter illuminates the LEO receiver with a downlink beam broadened to 1 mrad from the 4.4- $\mu\text{rad}$  full-width half-maximum (FWHM) diffraction limit. The beam is broadened to guarantee illumination of the LEO platform despite the initial GEO platform pointing errors. The broadened beam illuminates the LEO platform with 48 dB less power density than the perfectly pointed, diffraction-limited communications beam.

Next, the LEO platform initiates a parallel search using a charged-coupled device (CCD) to acquire the broadened downlink within the LEO pointing uncertainty region, which is also 1  $\mu\text{rad}$ . The LEO platform then tracks the downlink with repeated CCD acquisitions well enough to maintain the downlink within 1 to 2  $\text{bw}$  of the communications receiver field of view (FOV), and simultaneously corrects much of the initial pointing error in the uplink beacon. This coarse tracking loop is limited in bandwidth to less than 1 Hz because of the 1-s integration time of the acquisition sensor. During coarse tracking the uplink beacon (broadened to 18  $\mu\text{rad}$  from its diffraction limit of 4.4  $\mu\text{rad}$ ) illuminates the GEO platform.

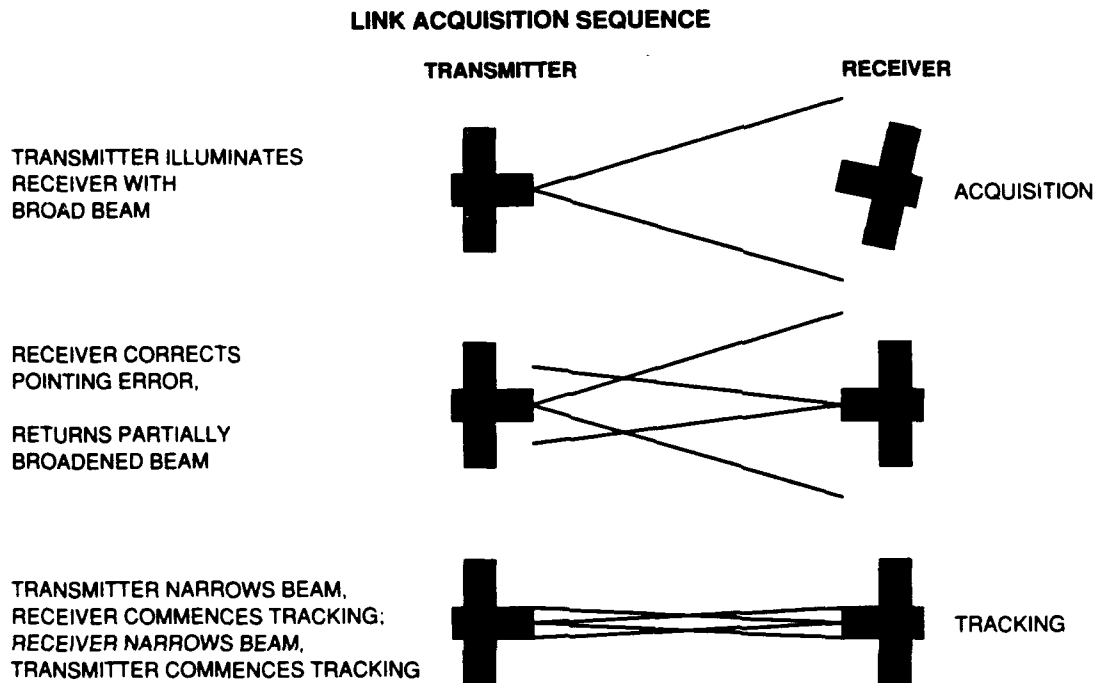


Figure 1. GEO-LEO link acquisition sequence.

The GEO platform employs a spiral scan serial search pattern to acquire the broadened uplink beacon. After uplink acquisition, the GEO platform initiates coarse spatial tracking of the uplink and narrows the downlink to the diffraction limit of  $4.4 \mu\text{rad}$ , which increases the power density of the downlink at the LEO platform by 48 dB. The consequent increase in detected downlink power enables a transition from CCD-based, low-frequency ( $\sim 1 \text{ Hz}$ ) spatial tracking to heterodyne, high-frequency ( $\sim 1 \text{ kHz}$ ) spatial tracking and data demodulation. At this time the LEO terminal also narrows the uplink beacon to the diffraction limit, increasing the optical power illuminating the GEO platform, which allows fine spatial tracking of the uplink by the GEO platform. This completes the acquisition and tracking sequence, and the link is then available for data communications.

## 2.2 LITE LINK BUDGETS FOR GEO TO LEO ACQUISITION, SPATIAL TRACKING, AND COMMUNICATIONS

Link budgets that indicate the expected signal photon arrival rates at the LEO terminal communications and tracking detectors during acquisition, spatial tracking, and communications between the GEO and LEO platforms are presented in Table 1; they are summaries of detailed link budgets previously presented [7,8,9].

**TABLE 1**

**Link Budget for GEO-LEO Downlink Spatial Acquisition,  
Tracking, and Communications**

	<b>Communications (2 Detectors)</b>	<b>Track (Az or EI) During Communications</b>	<b>Acquisition Sensor During Acquisition</b>
Transmit Laser (dBW)	-15.2	-15.2	-15.2
Transmit Optical Losses	-4.5	-4.5	-2.8
Transmit Aperture Gain (20 cm) Ideal, $(\pi D/\lambda)^2$	117.3	117.3	117.3
Transmit Spatial Pointing Loss	-1.0	-1.0	-3.0
Acquisition Beam Broadening (1 mrad)			-48.0
Space Loss (42,700 km)	-295.9	-295.9	-295.9
Receive Aperture Gain (20 cm) Ideal, $(\pi D/\lambda)^2$	117.3	117.3	117.3
Receive Optical Loss	-2.7	-2.7	-2.4
Communications/Track 80:20 Split	-1.0	-7.0	
Az/EI 50:50 Split		-3.0	
Received Power (dBW, $\lambda = 0.86 \mu\text{m}$ )	-85.7	-94.7	-132.7
in Photons/s	$1.2 \times 10^{10}$	$1.5 \times 10^9$	$2.3 \times 10^5$
in dB-Hz	100.7	91.7	53.7
Detector Quantum Efficiency (dB)	-1.4	-1.4	-5.2
Heterodyne Mode Matching Efficiency (dB)	-1.5	-1.5	
Finite Detector Size (dB)	-0.3	-0.3	
Front End Electronics Thermal Noise (dB)	-1.0	-1.0	
Communications Receiver Loss (dB)	-1.8		
Implementation Loss (dB)	-1.0	-1.0	
Detected Power (dB-Hz)	93.7	86.5	48.5
Required Post-Detection Power (dB-Hz)	90.9 [a] 88.4 [b] 84.2 [c]  (in Communications Channel)	72.9 [d]  (in Track Channel)	34.6 [e]  (at Acquisition Sensor)
Margin (dB)	2.8 @ 220 Mb/s 5.3 @ 110 Mb/s 9.5 @ 27.5 Mb/s	13.6	13.9

- a. Receiver sensitivity = 7.5 photons/bit for 4-ary FSK, 220 Mb/s with 15 MHz IF linewidth @  $10^{-2}$  BER
- b. Receiver sensitivity = 8.0 photons/bit for 4-ary FSK, 110 Mb/s with 2 chip combining and 15 MHz IF linewidth @  $10^{-2}$  BER
- c. Receiver sensitivity = 9.8 photons/bit for 4-ary FSK, 27.5 Mb/s with 8 chip combining and 15 MHz IF linewidth @  $10^{-2}$  BER
- d. From Equation (56), for commutated, correlation spatial tracking demodulator, and  $\eta = 1.0$ ,  $m^2 = 1.0$ , precorrelation bandwidth = 1.33 GHz, tracking bandwidth = 2.0 kHz, single axis NEA = 0.04 bw
- e. From Equation (22), for measured parameters of demonstration acquisition sensor, see Section 7.2

## **2.3 MICROJITTER ANGULAR DISTURBANCE SPECTRA**

Angular motions of the host platform result in disturbances in both the optical receiver and transmitter lines of sight (LOS); the spectral distribution of these disturbances determines the rejection that the spatial tracking system must provide. Little data are available that characterize such disturbances on actual host satellites. Two notable examples of measured spacecraft microjitter spectra are data taken on the Landsat-4 spacecraft [10] and on European Space Agency's (ESA) communication satellite OLYMPUS [11].

### **2.3.1 Microjitter During Spatial Tracking for LITE**

For LITE, considerable study was undertaken to estimate the on-orbit microjitter spectrum of the NASA ACTS satellite (see Reference 6 for a detailed description and additional references). The LEO platform dynamics were assumed to be similar to those on ACTS. A combination of measurements on a mock-up of a satellite similar to ACTS and NASTRAN modeling of the optical platform was used to predict the effects of various noise components on the receiver LOS. The major contributors to microjitter were noise in the earth sensor array used for spacecraft attitude control, mechanical vibration due to motion of the solar array drive, mechanical resonances in the RF antennas, and relatively high frequency jitter due to mass imbalances in the momentum wheels used for attitude stabilization. A comparison of the measured spectra for Landsat-4 and OLYMPUS and the predicted jitter spectra for ACTS are shown in Figure 2(a). In this figure the Landsat-4 and OLYMPUS curves are best fits to measurements of microjitter on those platforms. The power spectral density of the various expected jitter components on ACTS are plotted separately in Figure 2(b).

In the demonstration system the expected jitter environment on ACTS is simulated by driving each axis of the disturbance mirror pair with independent, Gaussian, white noise sources filtered with a single pole filter (at 35 Hz) in each axis. The spectrum of the filtered noise source in the demonstration system (rms jitter amplitude set to 2.1 bw) is shown in Figure 2(a).

### **2.3.2 Microjitter During Spatial Acquisition for LITE**

During acquisition the ACTS attitude control system was to be switched from the earth sensor array to gyro control. The resultant microjitter spectrum was identical in shape to the earth sensor array jitter spectrum, but reduced in amplitude from 100- to 2- $\mu$ rad rms. In addition, the solar array drive was to be turned off, which also removed the excitation of the RF antenna resonances. The microjitter during acquisition therefore was approximated as 1/50 of the earth sensor array noise plus the momentum wheel jitter.

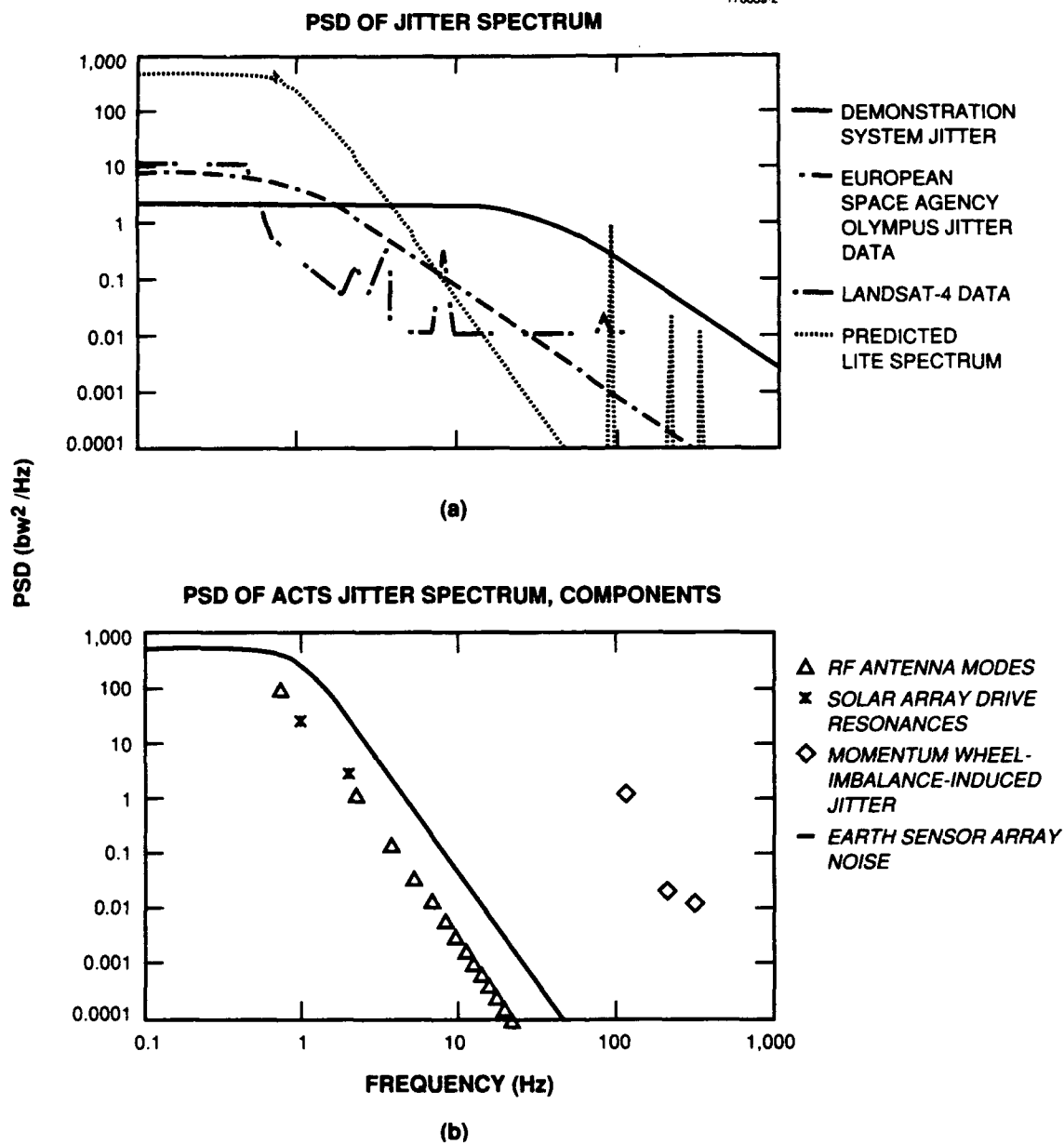


Figure 2. (a) PSD of jitter spectrum. (b) PSD of ACTS jitter spectral components.

### 3. SPATIAL ACQUISITION AND TRACKING SYSTEM REQUIREMENTS

#### 3.1 ACQUISITION SYSTEM REQUIREMENTS

The acquisition system on the LEO terminal must locate the broadened downlink with a high probability of success ( $> 0.99$ ) and a low false alarm rate ( $< 0.01$ ) for a budgeted signal photon arrival rate of  $2.3 \times 10^5$  photons/s. The initial 1 mrad or  $\sim 230$  bw angular uncertainty in locating the downlink must be reduced to less than 2 diffraction-limited bw. Acquisition must be performed in a time that is substantially less than  $\sim 1$  min. Finally, the acquisition system must sense the power surge that occurs when the downlink is narrowed, and it must initiate handoff to the spatial tracking system.

#### 3.2 SPATIAL TRACKING SYSTEM REQUIREMENTS

The heterodyne spatial tracking system must reduce the total angular misalignment between the received plane wave signal and the on-board Gaussian profile local oscillator (LO) beam to less than 0.1 bw in order to maintain acceptable heterodyne mixing efficiency in the receiver. This requirement was broken down as shown in Table 2.

**TABLE 2**  
**Spatial Tracking Requirements**

	<b>Az (bw)</b>	<b>EI (bw)</b>
Uncompensated Jitter	0.05	0.05
Sensor Noise (NEA)	0.04	0.04
Bias	0.025	0.025
Root-Sum-Square Sum per Axis	0.069	0.069
Root-Sum-Square Total Budget	0.097	

The jitter and bias disturbances are assumed to be independent. The tracking system is allocated no more than 20 percent of the total input signal power. It must operate at low signal-to-noise ratio (SNR) (less than unity within the total communications bandwidth at the output of the detector/amplifier front ends), in the presence of constant amplitude data modulation [FSK, phase shift keyed (PSK), or differential phase shift keyed (DPSK)], with the sun in the FOV, and must continue to function even in the presence of deep fades (as much as 10 dB below the communications threshold). In addition, because spatial tracking precedes frequency or phase tracking during link acquisition for LITE, the spatial tracker must operate with no detailed a priori knowledge of the heterodyne immediate frequency (IF) or phase, as long as the heterodyne IF of the received signal is within the input bandwidth of the front end amplifiers.

#### 4. SYSTEM OVERVIEW

The major system components are illustrated in Figure 3. The incoming optical signal is incident upon a large gimballed flat, referred to as the coarse pointing mirror (CPM), which can sweep the receiver FOV across a wide range of crosslink locations. The light is collected in a 20 cm, 40x telescope, relayed to a 2-axis fast steering mirror (FSM) for high-frequency, small-angle corrections, and relayed to either the acquisition sensor or the communications receiver as a function of the beamswitch position. The communications receiver is arranged as a balanced detector [12,13], with separate optical pickoffs for the azimuth and elevation track paths. The communications signal serves as a phase-coherent reference to the track channel outputs, from which an azimuth (elevation) tracking demodulator [14] is formed based upon the phase difference between each half of the azimuth (elevation) track channel. It can be shown that the angular misalignments in each axis between the LO and signal beam are proportional to these phase differences. The baseband error signal is processed appropriately and applied to the FSM to provide closed loop tracking of the angular error.

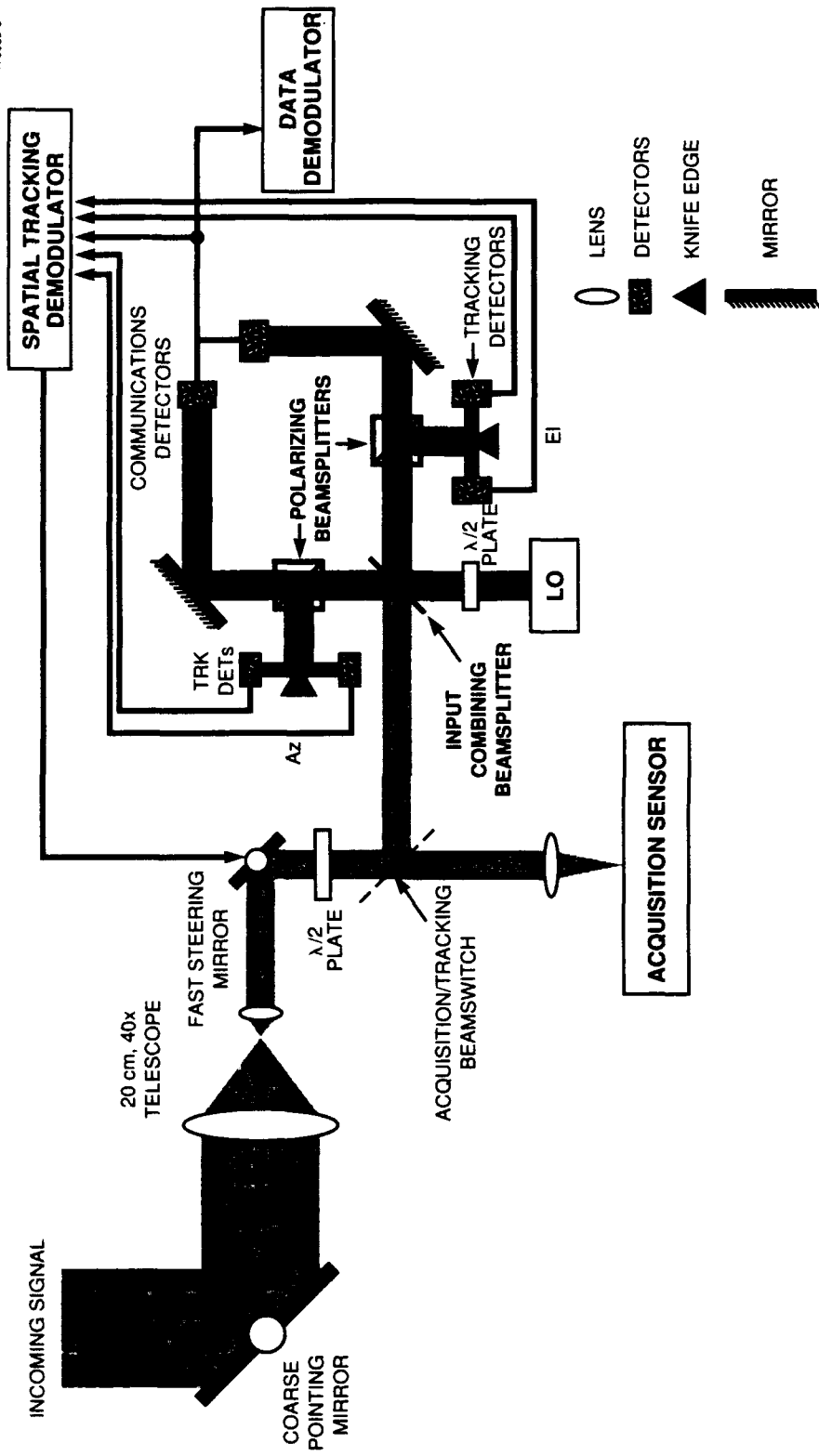


Figure 3. Coherent receiver with integrated acquisition and tracking subsystems.

## 5. OPTICAL LAYOUT COMMON TO BOTH ACQUISITION AND TRACKING SUBSYSTEMS

The optical layout used in the demonstration system was similar to that described previously [14,15]. Only that portion of the system beyond the 20-cm telescope was demonstrated, which meant that all of the optical processing was performed with 5-mm diameter beams, instead of 20-cm beams. A detailed optical layout is shown in Figure 4. This section describes that portion of the optical layout common to both the acquisition and tracking systems, i.e., from the signal laser to the acquisition/tracking beamswitch. The portions of the optical layout unique to acquisition and tracking are described in Sections 6.2 and 9.1, respectively.

### 5.1 SIGNAL SIMULATION

The received signal was simulated using a Hitachi HLP-8314 laser diode, operating in a single longitudinal mode at a nominal wavelength of  $0.86 \mu\text{m}$ . A Fujinon f/1.1, 7.7-mm focal length lens and a Special Optics anamorphic prism pair served to form the output of the laser into a circular Gaussian beam with a  $1/e$  (E field) radius of 2.5 mm. A pair of Optics For Research Faraday isolators, each with a clear aperture of  $5 \mu\text{m}$ , was used to reduce feedback to the signal laser. A neutral density filter was placed in front of the first isolator to further attenuate backscattering from the isolator crystal into the laser. A small percentage of the signal was picked off, using the inherent imperfection of the high-reflectance coating on the first fold mirror, and sent to a 300-MHz free spectral range Fabry-Perot interferometer (Coherent model 216) for monitoring purposes.

Approximately 4 mW of the 30-mW output of the signal laser were available beyond the neutral density filter and the Faraday isolators. This output was coupled into a short ( $\approx 3$  m) length of polarization-preserving, single-mode fiber. The use of the fiber made it possible to locate the signal laser on a separate table without affecting the alignment of the system. The output of the fiber was collimated using another Fujinon lens; it then passed through an Isomet acousto-optic modulator, which served as a high-speed intensity modulator, with more than 50 dB of dynamic range. The acousto-optic modulator was driven with up to 1 W of RF power at 82 MHz. At this drive power 67 percent of the input optical power was diffracted into the first order output beam. The zero order beam was blocked, and the first order diffracted beam was passed through a Special Optics 20x beam expander. A 5-mm iris at the output of the beam expander was used to block all but the center of the expanded beam, forming a reasonable approximation to the 5-mm diameter plane wave that would be present at the output of the 40x, 20-cm telescope in the actual receiver. Finally, a Karl Lambrecht Corporation half-wave plate was placed beyond the 5-mm iris to control the orientation of the signal polarization.

### 5.2 JITTER SIMULATION AND TRACKING MIRRORS

Two pairs of single-axis, flexure-mounted, General Scanning Z2046 torque motor beam steerers (TMBSs) with 1-cm square mirrors were used to form the 2-axis angular jitter source and the 2-axis FSM for closed-loop spatial tracking. Each TMBS was configured with a position sensor (Appendix A) and



velocity feedback to provide sufficient active damping to reduce the Q of the first resonance (109 Hz) to that of a critically damped, second-order system. Details of the drive circuitry are given in Appendix A. The response of each position sensor was flat to beyond 1.1 kHz, and measurements of shaft position using both the shaft-position sensors and an external optical monitor agreed to within 1 percent at frequencies less than 1 kHz. The measured linearity between TMBS current and angular position was better than 1 percent. The TMBSs were configured to have excellent linearity and critical damping in order that an undistorted spiral scan could be generated during handoff (see Sections 9.5 and 11.9.2) without requiring any optical feedback.

To minimize beam walk, a pair of 75-mm focal length lenses was used to relay an image plane located halfway between the jitter TMBS pair to an image plane located halfway between the tracking TMBS pair.

### 5.3 ACQUISITION/TRACKING BEAM SWITCH

A pair of 300-mm lenses was used to relay the image plane at the tracking mirrors through a beamswitch to either the input of the CCD acquisition sensor or the input combining beamsplitter of the communications receiver, depending on the beamswitch position. Just ahead of the beamswitch was a polarizing beamsplitter, used to direct a small percentage of the incoming signal power into a monitor port for independent observation of signal power or signal angle variations.

The beamswitch, formed from an aluminum wheel, rotated a 1-inch circular mirror in or out of the beam path. When the mirror was not in the path all of the signal was incident on the CCD acquisition sensor. When the mirror was in the path most of the signal was sent to the heterodyne tracker, while a small fraction (-48 dB) was incident on the acquisition sensor because the mirror was coated to provide 48-dB attenuation in transmission. The effect of the narrowing of the signal beam (during the transition between acquisition and tracking) was modeled as a 48 dB increase in received signal optical power. The net result was that a constant signal power level was incident upon the CCD sensor during both acquisition and subsequent tracking. Purely for experimental convenience, this allowed the CCD to continue to monitor the signal beam position while the heterodyne tracker was operating. The mirror was under computer control and could be moved in or out of the beam path in about 200 ms. The angular repeatability of the beam position following several beamswitch cycles was measured to be better than 0.1 bw.

## 6. SPATIAL ACQUISITION SYSTEM IMPLEMENTATION

### 6.1 ACQUISITION SYSTEM OVERVIEW

The acquisition system optics mapped the downlink uncertainty region onto the focal plane CCD acquisition sensor (Figure 5). (Appendix B provides a tutorial on the CCD.) A parallel search algorithm was employed to locate the downlink within the uncertainty region. Information from the acquisition sensor was passed to the overall acquisition/tracking computer controller, which determined the angular misalignment between the downlink and the communications receiver FOV. The acquisition/tracking controller then generated commands to reposition the tracking mirrors, redirecting the downlink to within the pull-in range of the heterodyne spatial tracker. When saturation of the CCD due to the narrowing of the downlink beam was detected, handoff from CCD-based acquisition to heterodyne spatial tracking was initiated.

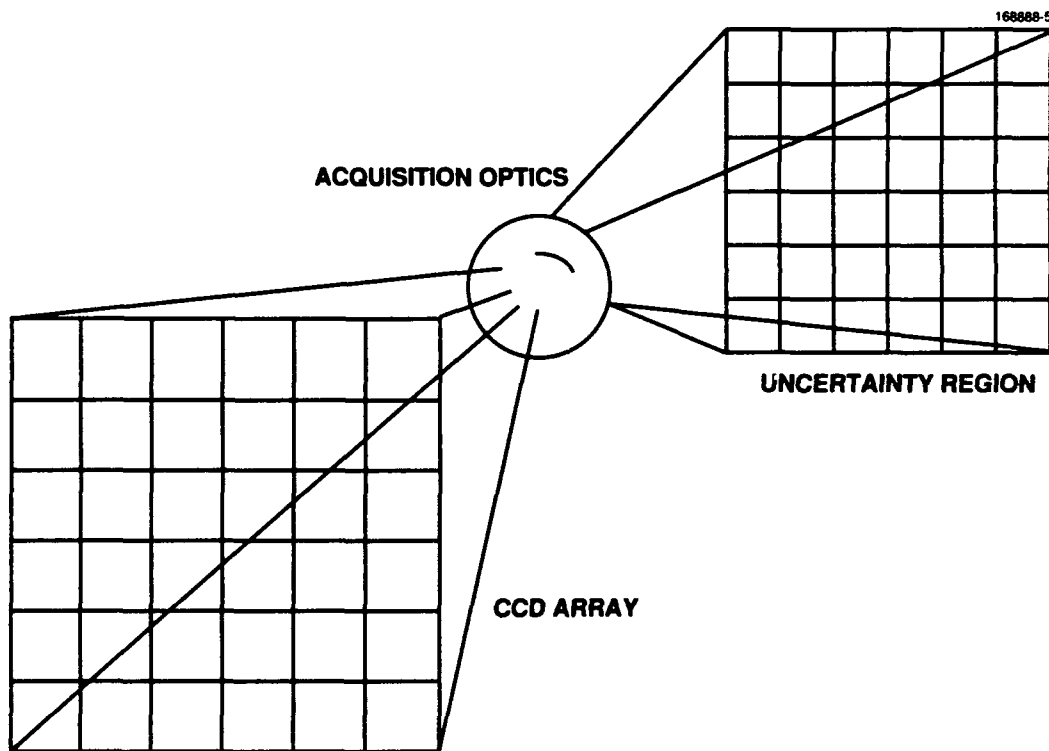


Figure 5. Spatial acquisition using focal plane array.

The frame integration period was chosen to be 1 s. This yielded a sufficiently high SNR that the required signal detection probability could be obtained at room temperature while maintaining sufficient dynamic range, within a reasonably prompt acquisition time. A shorter integration time would result in a smaller SNR, thereby increasing the signal power required to maintain the same probability of successful acquisition. For example, a factor of 2 reduction in integration time in the system would theoretically require a 2.45-dB increase in signal power to maintain a probability of success of 0.99 [Equation (22)]. A longer integration time would improve the SNR at the cost of increased acquisition time and the possibility of saturating the CCD with either accumulated dark current or signal. An electronic shutter with on/off times of approximately 5 ms was placed in front of the CCD to control the illumination of the CCD during acquisition.

Note that alternatives to the parallel search algorithm exist, such as the serial scan used in the LITE uplink acquisition system [5,6]. However, at a photon arrival rate low enough to require an integration time on the order of 1 s for acceptable probability of acquisition, a serial search of 40,000 possible locations was deemed impractical.

## **6.2 SPATIAL ACQUISITION SYSTEM LABORATORY OPTICAL LAYOUT**

The CCD acquisition sensor was located in the back focal plane of a 100-mm lens. The input to the spatial acquisition system (simulating the output of the 20-cm, 40x telescope) was a collimated beam 5 mm in diameter. The calculated diffraction-limited FWHM spot size at the CCD was  $17.7 \mu\text{m}$ , or two-thirds the width of a single pixel. The uncertainty region of  $\sim 230 \times 230$  diffraction-limited beamwidths therefore corresponded to an array of approximately  $153 \times 153$  pixels. In order to reduce processing time it was convenient to use a  $200 \times 200$  pixel subarray of the  $512 \times 512$  pixel CCD, which more than adequately covered the uncertainty region.

The focused spot size at the CCD was selected to provide sufficient resolution while maintaining adequate SNR in the pixels that contained the focused spot [16]. A spot size approximately equal to 1 pixel makes efficient use of the signal. For a spot much smaller than 1 pixel, the CCD cannot resolve beam motions within a pixel. When the spot is spread over several pixels, the presence of background and readout noise causes the SNR to drop with no attendant gain in resolution. The estimated effective spot size in the laboratory implementation, after accounting for acoustic and mechanical disturbances and imperfections of the lens, was between 0.85 and 0.9 pixel.

## **6.3 ACQUISITION ALGORITHM**

During spatial acquisition the CCD sensor operated in either frame integration mode or readout mode (Figure 6). During frame integration the clocks were disabled, which allowed charge, due both to dark current and any incident photons, to accumulate in the CCD. During readout the shutter was closed and the clocks were enabled to serially transfer the accumulated charge from the array to the output amplifier. The output amplifier developed a voltage proportional to the charge in each pixel, and a digital representation of this voltage was stored on a digital processing board in one of three memory maps of the CCD. The three memory maps included a signal frame, a background frame, and a difference frame.

The acquisition process required integrating both a background and a signal frame. The background frame was taken with the shutter closed during integration to characterize the dark noise in the array. The signal frame was taken with the shutter open during integration to gather charge from both dark current and signal photons. Using digital hardware the background frame was subtracted from the signal frame, forming a difference frame, to reduce the effects of pixel-to-pixel variations across the array in average dark current. The CCD was continuously read out between frame integrations to clear the array of accumulated dark current prior to the next frame integration.

176039-5

MODE	INTEGRATION (Accumulate Charge)	READOUT (Transfer Charge)
CLOCKS	DISABLED	ENABLED
SHUTTER	BACKGROUND FRAME ↓ CLOSED	SIGNAL FRAME ↓ OPEN
		CLOSED

Figure 6. CCD modes of operation.

Gain calibration of the CCD was not implemented in the system. Although pixels with particularly high or low gain could affect the accuracy of the acquisition system estimate of signal position, the response of only a few pixels (less than 0.1 percent) was significantly different from average (see Section 8.4.2), and the performance of the acquisition system was not limited by gain nonuniformity in the acquisition sensor. It is noted that it is theoretically possible to calibrate gain using a uniform illumination of the CCD.

The detailed acquisition sequence follows (Figure 7). Prior to the acquisition session a background frame was integrated, read out, and stored in memory. The session began with the integration of a signal frame. Next, as the signal frame was read out from the CCD, the background frame data was subtracted from the signal frame data, and the resultant difference frame was stored in memory. Using hardware processing, the  $200 \times 200$  pixel difference frame was scanned within 32 ms to identify the address of the  $2 \times 2$  pixel block with the largest total signal, referred to as the MAXBLOCK. Given that the focused spot size (FWHM) on the array was approximately 0.9 pixel, an estimated 75 to 82 percent of the signal energy would have been contained within the MAXBLOCK group. The MAXBLOCK address and the signal level of each pixel within the MAXBLOCK group was then sent to the acquisition/tracking controller. By using a simple first order algorithm (difference/sum) similar to that used for a quadrant detector, the acquisition/tracking controller obtained with subpixel resolution an estimate of the signal

location within the MAXBLOCK. Commands were then generated to position the track mirrors so that the signal was centered within the heterodyne receiver FOV. The location of the heterodyne receiver FOV relative to the acquisition sensor coordinates was determined by the acquisition/tracking system through a boresight procedure prior to the start of the acquisition sequence.

176039-6

<b>PROCESS</b>	
1. INTEGRATE BACKGROUND FRAME	SHUTTER: CLOSED CLOCKS: DISABLED
2. READOUT AND STORE BACKGROUND FRAME	SHUTTER: CLOSED CLOCKS: ENABLED
3. INTEGRATE SIGNAL FRAME	SHUTTER: OPEN CLOCKS: DISABLED
4. READOUT SIGNAL FRAME, SUBTRACT BACKGROUND FRAME, AND STORE DIFFERENCE FRAME	SHUTTER: CLOSED CLOCKS: ENABLED
5. LOCATE MAXBLOCK	
6. TRANSFER MAXBLOCK DATA TO CONTROLLER FOR SUB-PIXEL LOCATION ESTIMATION	
7. REPEAT (3) THROUGH (6) UNTIL POWER SURGE DETECTION	

*Figure 7. Acquisition sequence.*

A loop referred to as "coarse tracking" continued to update the CCD estimate of the location of the signal and adjust the tracking mirrors until a power surge was detected. This surge, the consequence of downlink beam narrowing, resulted in the saturation of the MAXBLOCK pixels and was detected by testing for the full-scale reading of the value of the MAXBLOCK sum. Upon surge detection the beamswitch redirected the signal to the heterodyne spatial tracker and the handoff procedure was initiated.

The minimum total acquisition time was the sum of the integration interval, the readout time, and the processing time. The integration interval was 1 s. With a frame readout rate of 1 MHz the readout of the  $200 \times 200$  subarray required 113 ms. In order to clear the CCD, however, the entire array was read, requiring 285 ms. The processing time to identify the MAXBLOCK location was 32 ms. The total acquisition time therefore was 1.32 s. This total increased to 2.6 s if a dark frame was taken prior to every signal acquisition instead of just at the beginning of the session. It was convenient (and within budgeted

time constraints) to integrate a new dark frame prior to every signal acquisition, thereby assuring that the dark frame stored in memory more accurately represented dark current levels at the time of acquisition.

This algorithm does not define a protocol for acquisition when the initial uncertainty is greater than the CCD FOV. If the signal were outside the CCD FOV, consecutive positional estimates in the coarse tracking loop would vary by more than a few pixels. One approach could be to program the acquisition/tracking controller to look for this condition and react to it by repositioning the CCD FOV and restarting the acquisition session.

#### 6.4 ELECTRONICS

The system electronics consisted of five units: the CCD imager, a multiphase clock generator and voltage generator, an analog signal conditioner, a digital memory and processing unit, and a microprocessor-based control board. The acquisition subsystem was under the control of the HP 9000/320-based acquisition/tracking computer controller, as shown in Figure 8.

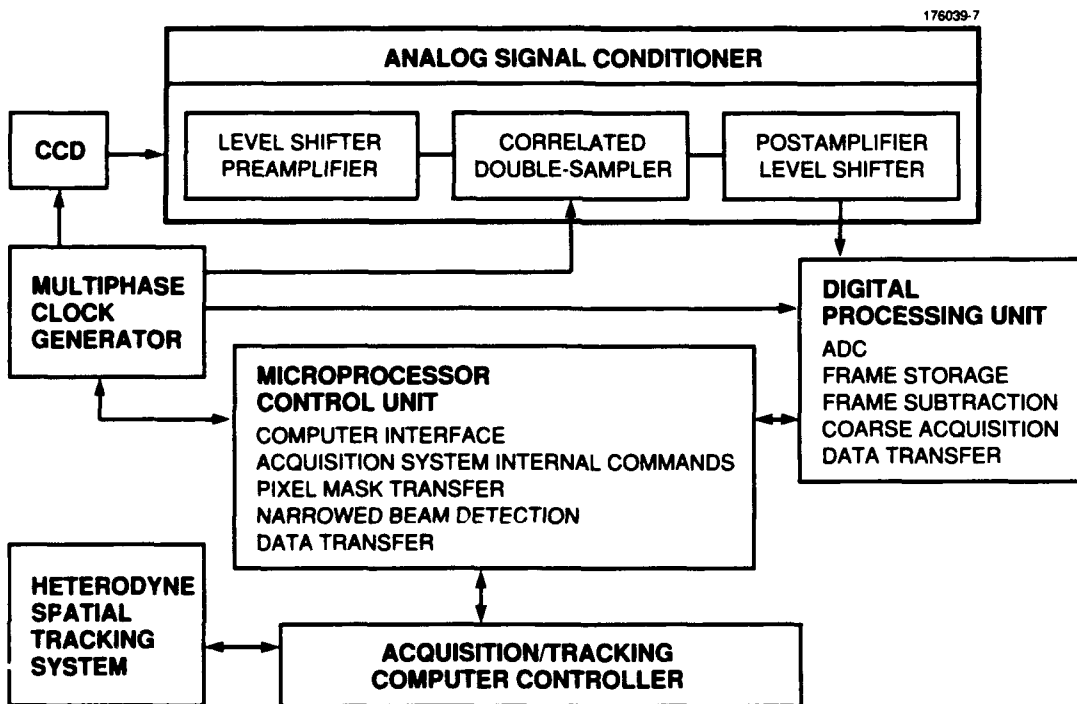


Figure 8. Spatial acquisition subsystem block diagram.

### 6.4.1 CCD

*Characterization.* Our acquisition sensor was required to be large enough to cover the 1-mrad uncertainty region with a resolution of better than 2 bw. A  $200 \times 200$  pixel subarray of the  $512 \times 512$  pixel TK512M used in conjunction with a 100-mm lens covered approximately 1.3 mrad in object space, or 295 beamwidths. Each pixel was square with  $27 \mu\text{m}$  on a side and had a FOV equal to 1.5 diffraction-limited beamwidths.

The TK512M is specified to have dark current less than  $10 \text{ nA/cm}^2$  at  $20^\circ\text{C}$ , or  $4.37 \times 10^5 \text{ e-/s/pixel}$ . Our particular sensor was measured to have an unusually low dark current density of  $130 \text{ pA/cm}^2$  or  $5.7 \times 10^3 \text{ e-/s/pixel}$  at room temperature [17]. (By thermoelectric cooling to  $-60^\circ\text{C}$ , dark current could likely have been reduced to close to  $1 \text{ e-/s/pixel}$ .)

The accumulated charge due to dark current may be represented as a bias plus shot noise. In a perfect CCD the dark current, and hence the bias, would be the same across the entire array. Unfortunately, due to substrate inhomogeneities there is a certain amount of pixel-to-pixel nonuniformity. These inhomogeneities result in highly repeatable pixel-to-pixel variations in dark current, which cause both variations in pixel bias and shot noise. Variations in pixel bias or average accumulated dark current may be removed by recording an unilluminated frame from the CCD and subtracting it from any subsequent frame. The limitations introduced due to increased dark-current-induced shot noise in pixels with unusually large dark current "blemishes" may be removed by pixel masking.

Read noise is generally a function of readout rate and device temperature. Most specifications are given for rates much slower than the 1 MHz readout rate of our system. The specification for the TK512M is  $10 \text{ e-}$  at a 200 kHz readout rate and  $-90^\circ\text{C}$ . Our sensor readout noise was measured to be 78 rms  $\text{e-/pixel}$  at a 1 MHz readout rate and room temperature [18].

Crosstalk, the lateral diffusion of electrons generated below the depletion region of the CCD, is only significant at wavelengths longer than  $0.75 \mu\text{m}$ . For our purposes, the crosstalk had to be low enough that the estimate of signal location was not noticeably affected. Measured values for our acquisition sensor were 8 percent between rows and 9 percent between columns [18]. These numbers represent the relative value of one pixel adjacent to a second pixel in which a signal (much smaller than a pixel) is centered. Optical imperfections, charge transfer inefficiency, and insufficient video bandwidth may have contributed to the measured values. It was determined that this level of crosstalk had a negligible effect on both the probability of acquisition and the accuracy of the estimate of signal location [18].

Table 3 summarizes the characteristics of the acquisition sensor necessary to meet system requirements [19] and the actual performance of the TK512M [17].

**TABLE 3**  
**CCD Characteristics**

Characteristic	Required	Measured: TK512M
Resolution	200 × 200	512 × 512
Quantum Efficiency	20-30 percent	30 percent
Full Well Charge	>10 <sup>5</sup>	8.5 × 10 <sup>5</sup>
Dark Current, $\Gamma_d$	<10 <sup>4</sup> e-/s/pixel	5685 e-/s/pixel
Blemishes	<<1 percent	0.05 percent
Read Noise, $N_r$	<200 rms e-/pix	78 rms e-/pix
Crosstalk		8-9 percent

**Packaging.** The CCD was mounted on a 44-pin, non-hermetic metal package (see Figure 9). This in turn was mounted on a board that provided space for connectors as well as filtering and circuit protection components. This board was attached to a 2-axis translation stage, to allow spatial alignment, and was enclosed in a light-tight box. A Uniblitz 225L shutter, controlled by a 122-B shutter drive unit, screwed into the front panel of the box. The time required for the shutter to either open or close was approximately 5 ms. A mounting fixture held the lens assembly and an optical interference filter in front of the shutter. Electrical inputs included three serial clock phases, three parallel clock phases, the reset pulse, and the transfer gate signal that provided charge isolation between the output register and the imaging area. The entire package was fastened to a mounting block that positioned the CCD subarray at the proper height in the beam path.

#### 6.4.2 Clock Generator

The programmable multiphase clock generator (PMPCG) was designed as a general-purpose system capable of providing the variety of clock signals typically required by a CCD [20]. The PMPCG had 14 channels with programmed bit patterns that could be read out at rates up to 30 Mb/s. The pattern for the TK512M operated at 25 Mb/s to clock serial data from the CCD at 1 MHz. The PMPCG provided the eight phases needed for CCD readout: serial and parallel clocks, reset, and transfer gate. It also provided the clamp and hold signals for the correlated double sampler, a clock for sampling and storage on the digital board, frame synchronization, and an internal control line for program sequencing.

The clock lines had to be well-defined with low noise and minimal overshoot at the CCD. They had to be able to drive capacitive loads up to 7500 pF with 10- to 15-V signals. This was accomplished by feeding the transistor-transistor logic (TTL) signals into a DS0026 line driver.

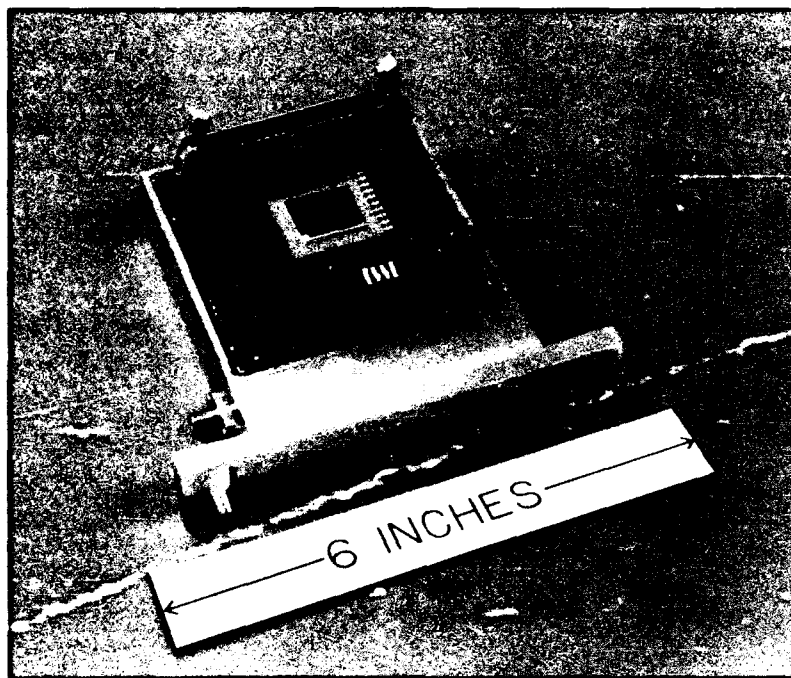


Figure 9. CCD fixture.

The clock generator provided adjustable amplitude and rise time for each phase. Pulse width was changed by altering pattern memory. Signal shape was found to be critical: fine-tuning resulted in significant performance improvement. With narrow pulse widths of 240 ns for each serial clock and only 80 ns for the reset pulse, clock stability and delays were also critical issues. The master clock was driven by a crystal oscillator with stability to within 100 PPM.

A number of techniques have been used by others [21,22] to improve performance. Holding two of the three serial clocks high during the parallel transfer to the serial shift register improves charge transfer efficiency (CTE). Raising the upper clock voltage levels also could improve CTE, but at the expense of higher dark current. Dark current can be reduced by holding serial clocks high and parallel clocks at a negative voltage during integration. The latter technique, "inverted channel operation," would have been implemented with different clock drivers if the dark current had been unacceptably high.

#### 6.4.3 Analog Signal Conditioner

The analog signal conditioner provided gain and offset for the CCD output signal as well as correlated double sampling (CDS). CDS, a technique commonly used with CCDs, removed reset noise caused by thermal noise from the resistance of the MOSFET reset switch, approximately 100 to 300 rms electrons. The output of the CCD field-effect transistor (FET) amplifier is shown in Figure 10. At the

start of a read cycle, a reset pulse set the output capacitor voltage to a reset potential through a MOS field effect transistor (MOSFET) switch. Following reset, the capacitor was charged an additional amount by the photoelectrons collected in the addressed pixel. Because of noise in the FET, the reset settling potential varied from cycle to cycle. Using CDS, each pixel voltage was measured in reference to its reset potential rather than a fixed voltage. This eliminated correlated noise, leaving only uncorrelated noise of the output MOSFET amplifier. Tektronix specified the uncorrelated noise to be less than 10 rms  $e^-$ /pixel.

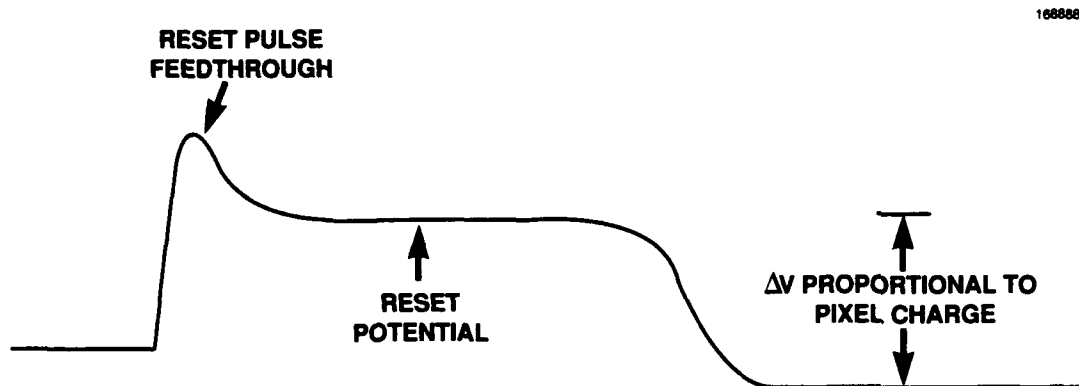


Figure 10. CCD FET output.

The analog output was fed into a buffer amplifier, followed by a fast-settling operational amplifier with gain and offset adjust to eliminate dc offset from the CCD signal. The CDS was based on the Analog Devices HTS-0010 sample/track-and-hold amplifier [23]. A post-amplifier and level shifter matched the signal to the analog-to-digital converter input range.

#### 6.4.4 Digital Processing Unit

The five primary responsibilities of the processing unit were analog-to-digital conversion, frame storage, background frame subtraction, coarse acquisition, and data transfer [24,25]. A block diagram of the digital processing unit is shown in Figure 11.

The input to the processing unit was the analog output of the post-amplifier. Analog-to-digital conversion was performed with the Datel ADC-500, a 12-bit, 2-MHz hybrid with an input range of 0 to 10 V.

The processing unit stored three frames: the background frame, the signal frame, and the difference frame. As the signal frame was read out from the CCD and stored, the background frame was subtracted from it using two's complement subtraction to provide the difference frame. The processing unit accommodated data from CCDs with dimensions of up to  $1024 \times 1024$  pixels. Each frame was stored in a bank of 18-pin,  $1 \text{ M} \times 1$  bit complementary metal-oxide semiconductor (CMOS) dynamic random access memory (DRAM) dual in-line packages.

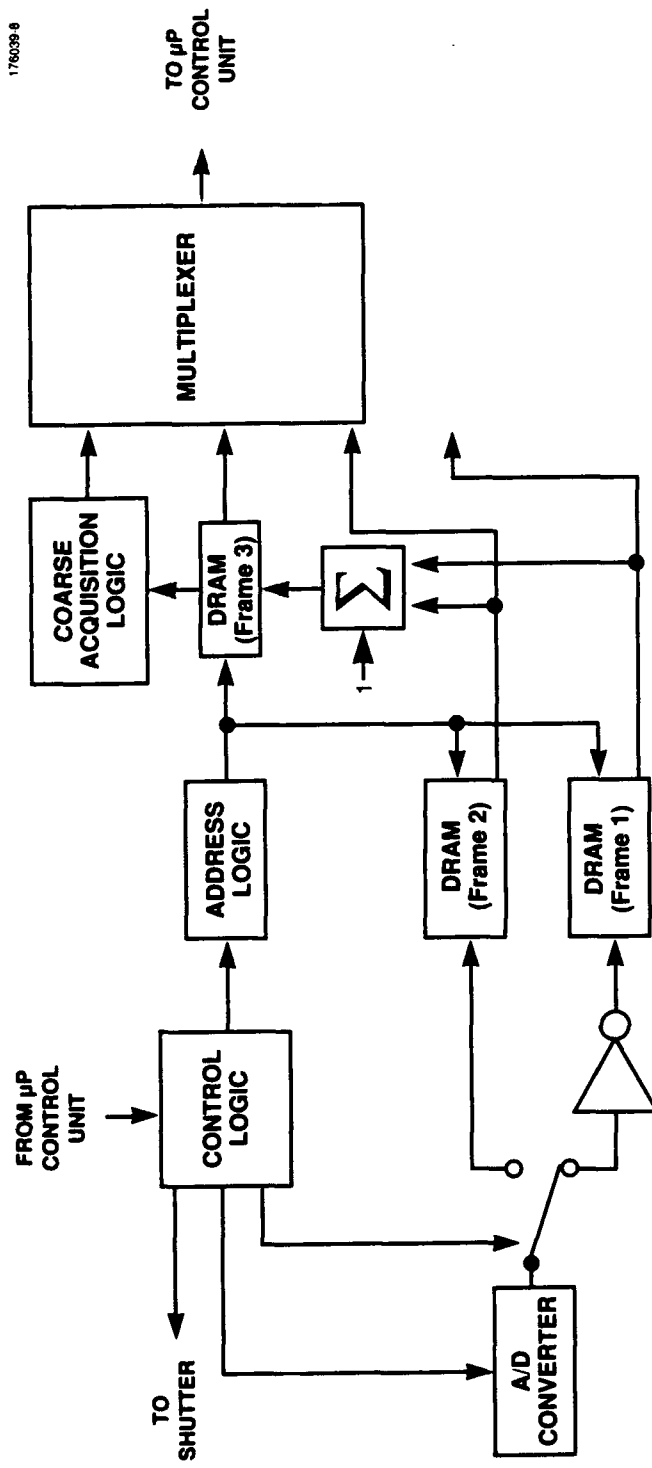


Figure 11. Digital processing unit block diagram.

Coarse acquisition was the process of finding the MAXBLOCK address. This was performed in hardware while the fine centroiding with subpixel accuracy was performed in software. These choices minimized the combination of processing time and hardware. Processing time to find the MAXBLOCK address within the  $200 \times 200$  pixel processing region was 32 ms. The most significant time constraint in processing was due to the access time of the DRAM used for data storage.

Frame data and the address of MAXBLOCK were transferred via an IEEE-488 bus through the microprocessor control board to the acquisition/tracking controller, which performed fine centroiding using a first-order algorithm.

#### **6.4.5 Microprocessor Control Board**

The microprocessor control board (see Figure 8) was responsible for interfacing with the acquisition/tracking controller and commanding the internal operations of the acquisition system. The unit was designed around a Motorola 68000 microprocessor receiving commands over an IEEE-488 bus. The control unit was also responsible for pixel mask transfer to the processing unit (see Section 8.4.2), beam narrowing detection (see Section 6.3), and data transfer from the processing unit to the acquisition/tracking controller.

## 7. SPATIAL ACQUISITION SYSTEM THEORY OF OPERATION

### 7.1 ALGORITHM TO OBTAIN SUBPIXEL RESOLUTION

The hardware processing of the CCD difference frame had as its output the MAXBLOCK address and the values of the each pixel of the  $2 \times 2$  pixel block which made up the MAXBLOCK group (Section 6.2). A simple first order algorithm was used to calculate a subpixel offset within the MAXBLOCK group, based on the value of each of the four MAXBLOCK pixels. This process, referred to as fine centroiding, improved the accuracy of the estimate of the signal position.

The MAXBLOCK location returned by the processing unit was the address,  $P1$ , of the lower left hand pixel of the MAXBLOCK group as shown in Figure 12(a). The complete estimate of the beam position was expressed as  $P1 + \Delta(Az,El)$ , where  $\Delta(Az,El)$  represented the subpixel offset of the beam location within the MAXBLOCK group.  $\Delta(Az,El)$  was defined with respect to a coordinate system in which the center of pixel  $P1$  was the origin. The following equations were used to calculate  $\Delta(Az,El)$  with  $V_i$  representing the value of pixel  $P_i$ :

$$\Delta_{Az} = 0.5 + K1 [(V4 + V3) - (V1 + V2)] / (V1 + V2 + V3 + V4) \quad (1)$$

and

$$\Delta_{El} = 0.5 + K2 [(V2 + V3) - (V1 + V4)] / (V1 + V2 + V3 + V4) \quad (2)$$

This algorithm normalized the signal to make the calculated offsets independent of received total signal power. The additive constant 0.5 resulted from defining the origin at the center of  $P1$ . Consider a spot evenly centered within  $P1$ ,  $P2$ ,  $P3$ , and  $P4$  such that the numerator equals zero in Equations (1) and (2). The offset along either axis from (0,0), the center of  $P1$ , should be 0.5, or half a pixel from the center of  $P1$ .

The gain factors  $K1$  and  $K2$  are dependent upon the size and shape of the focused signal beam relative to the size and shape of a CCD pixel. A poor selection of  $K$  yields discontinuities in the single axis transfer function between actual estimated beam position: low gain produces a staircase shape, high gain results in "hop-back." These discontinuities occur as the beam location is translated through the point at which the MAXBLOCK address changes, e.g., from  $P1$  to  $P1'$  in Figure 12(b). The discontinuity may be expressed analytically as the difference between  $(P1 + \Delta)$  and  $(P1' + \Delta')$ .

To examine the effects of the gain factor  $K$  on the calculated offset, consider the simple case of the translation along one axis of a uniformly illuminated square spot in the focal plane, where the spot is the same size as 1 pixel. Such a beam shape is impractical, but it will serve to clearly illustrate the offset variation as  $K$  changes. For this ideal case and when  $K = 0.5$ , the first order difference/sum algorithm yields a linear transfer function with unity gain between actual and estimated beam position. The effects of suboptimum  $K$  values have been calculated and are summarized in Figure 13.  $K = 0.5$  is correct only for a spot size equal to 1 pixel; the ideal gain must be increased for a larger spot and decreased for a smaller spot.

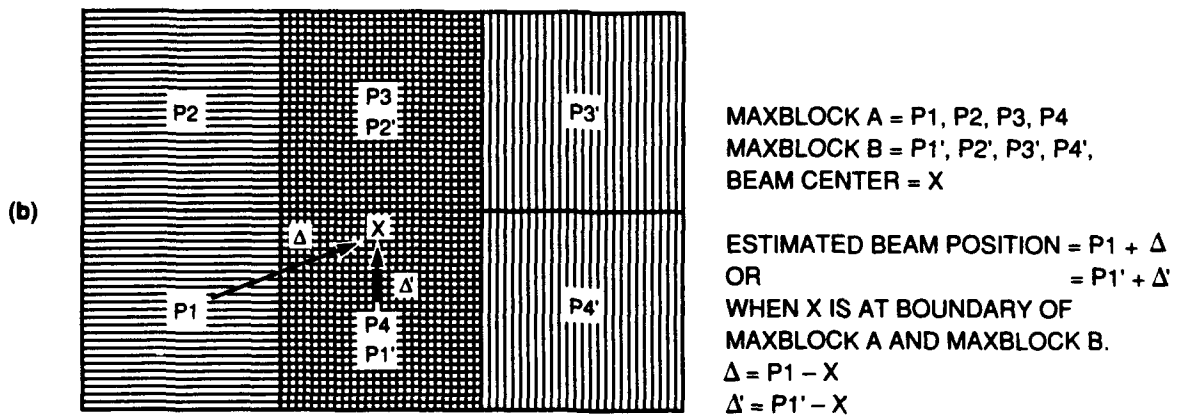
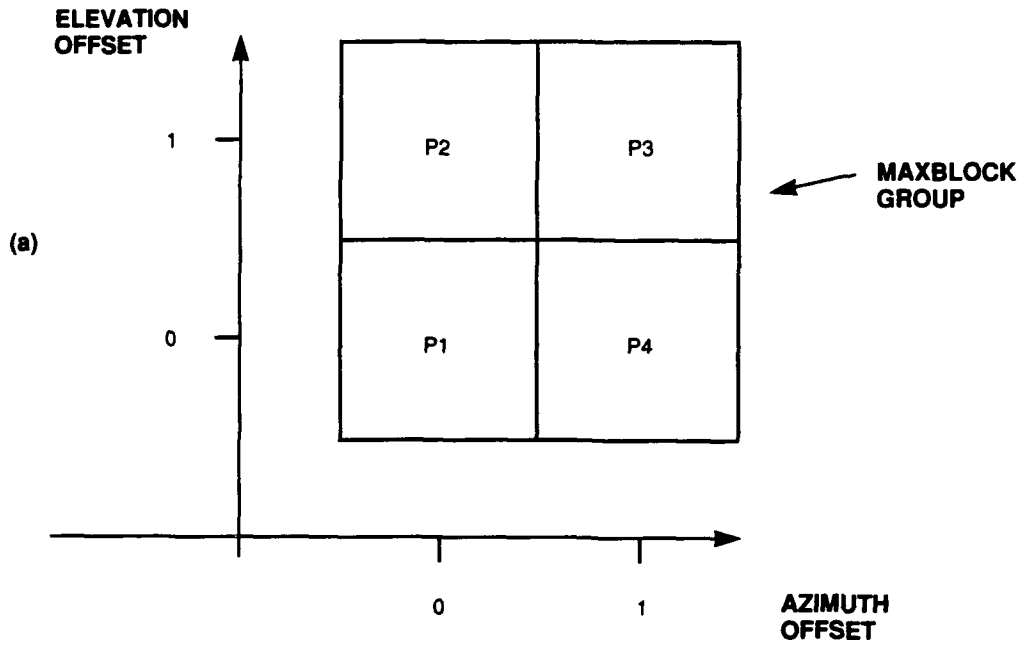


Figure 12. Maxblock geometry.

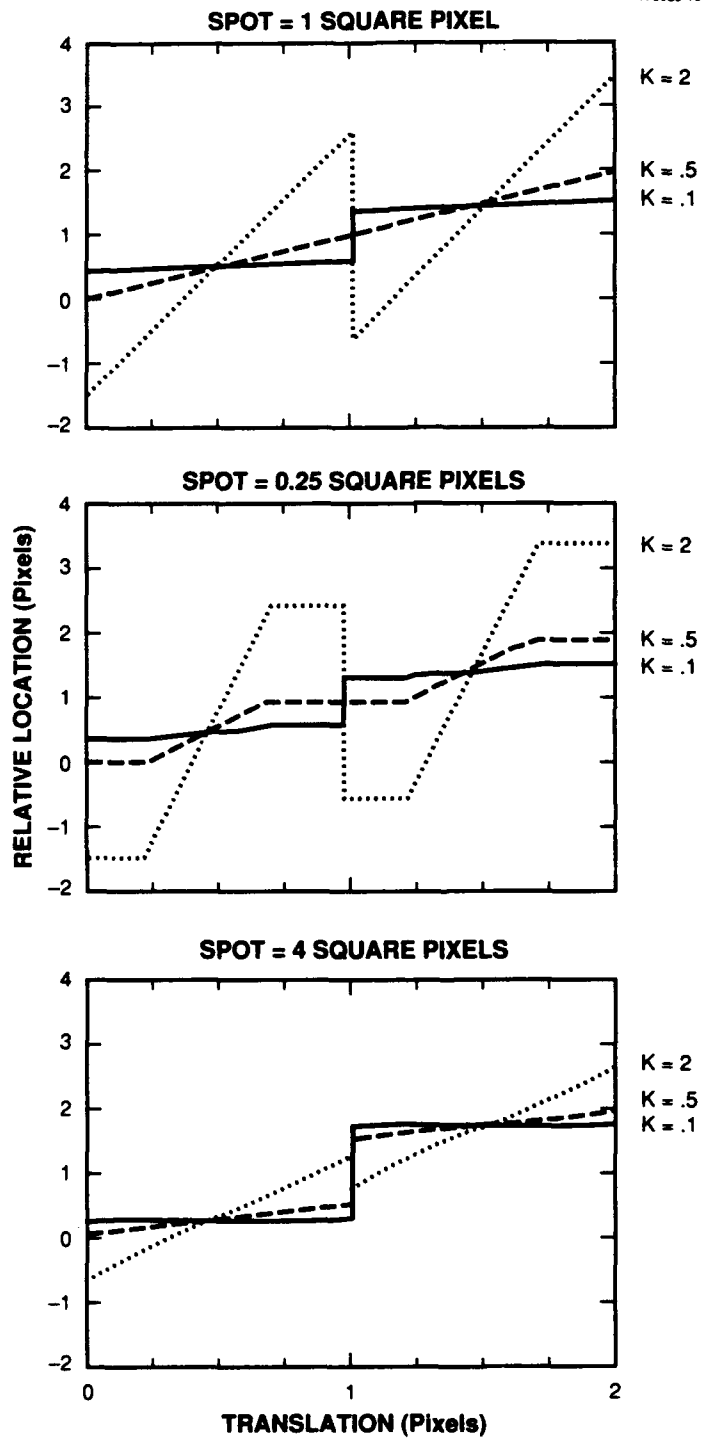


Figure 13. Calculated CCD sensor output vs focal plane translation, for a variety of gains and for several spot sizes.

In the more realistic case of a circularly truncated uniform plane wave at the input to the focusing lens, the focal plane distribution is an Airy disk. Using the first order difference/sum algorithm with various  $K$  values, the transfer functions between actual and estimated beam position were derived numerically for single axis translation for several Airy disk sizes. The results are summarized in Figure 14, which shows, for example, that when the full width half maximum diameter of the Airy disk is equal to 1 pixel, the  $K$  value yielding a continuous transfer function is 0.66. Plots of the mean square error and peak error, relative to a linear, unity gain transfer function are shown in Figure 15. As can be seen by comparing Figures 14 and 15, the  $K$  value which yields the minimum error is very close to the same  $K$  value which minimizes the hop-back or staircase discontinuities. The same analysis was performed for an untruncated Gaussian input beam, and the results were qualitatively the same.

## 7.2 PROBABILITY OF ERROR IN ACQUISITION

The performance of the acquisition algorithm, with MAXBLOCK location as its output, has been previously analyzed [26,16]. A missed acquisition is defined as the event in which the selected MAXBLOCK contains no significant signal power. When the diameter of the signal Airy disk is equal to one pixel width, any such MAXBLOCK will be more than 2 pixels away from the actual beam location. Missed acquisition will occur when the noise in some  $2 \times 2$  pixel block exceeds the signal plus noise in the  $2 \times 2$  block of pixels that actually contains the largest portion of the signal.

In order to simplify the analysis of the probability of missed acquisition, the following assumptions are made. First, an approximation to the union bound, where at least one such noise cell exists, is made. This should introduce negligible error when the probability of multiple noisy  $2 \times 2$  pixel groups is very small. This assumption is reasonable for situations where the probability of misacquisition is less than 1 percent. Second, in the calculations, the signal power lying outside the  $2 \times 2$  pixel group that contains the largest proportion of signal photoelectron is disregarded. For an Airy disk diameter of 0.9 pixel, numerical analysis indicates that between 18 and 25 percent of the signal photoelectrons fall outside of the  $2 \times 2$  MAXBLOCK group. Consequently, an average of 78 percent of the signal photoelectrons are collected within the MAXBLOCK group.

The following nomenclature is used:

$$M^2 = \text{number of } 2 \times 2 \text{ contiguous pixel groups in CCD array} = (200)^2$$

$$\Gamma_s = \text{detected signal rate parameter in photoelectrons/s}$$

$$\Gamma_d = \text{dark current noise rate parameter in } e^-/\text{s/pixel}$$

$$N_f^2 = \text{readout noise variance in } e^-^2/\text{pixel}$$

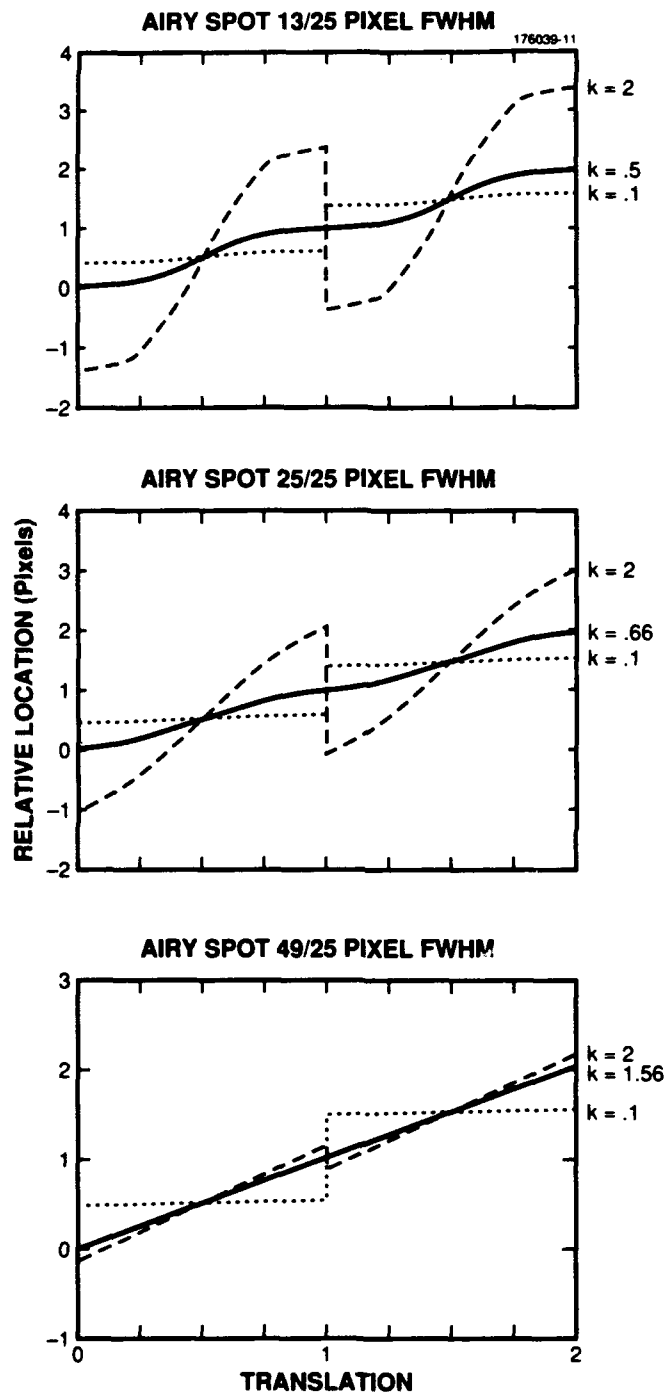


Figure 14. Calculated CCD sensor output vs focal plane translation, for several airy distributions, and several gains.

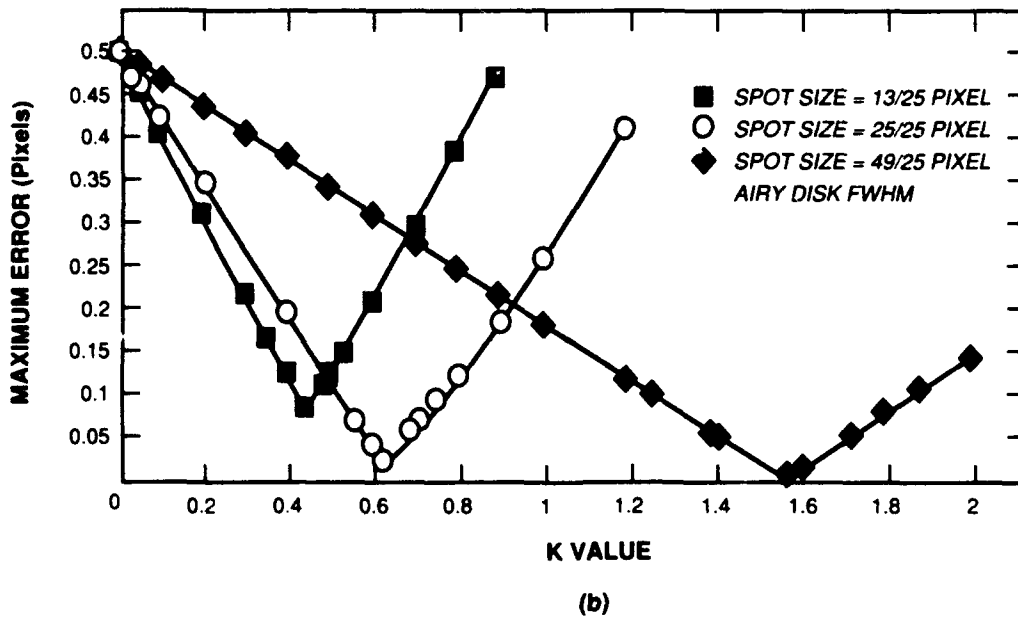
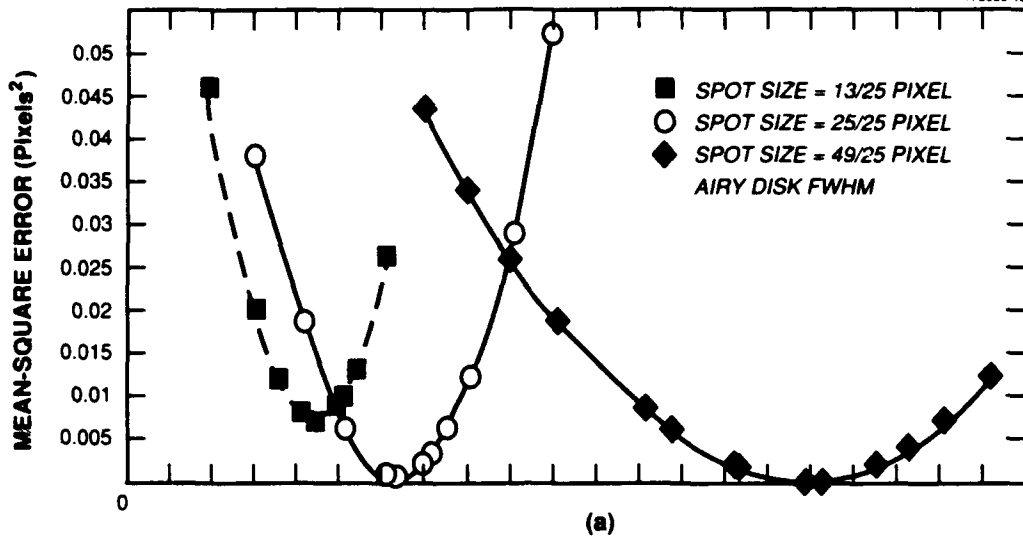


Figure 15. (a) Calculated mean square error vs gain (K). (b) Calculated peak error vs gain (K).

$N_q^2 = \text{ADC quantization noise variance in } e^-/\text{pixel (nominally 261)}$

$T = \text{CCD integration time in seconds (nominally 1)}$

With dark current and readout noise a pixel with no signal will have

$$\text{variance}_n = \Gamma_d T + N_f^2 \quad (3)$$

With some part of the spot illuminating a pixel, there is a Poisson-distributed contribution from the signal with mean equal to variance such that

$$\text{mean}_s = \text{variance}_s = C \Gamma_s T \quad (4)$$

where  $C$  is the fraction of the spot within the pixel ( $0 \leq C \leq 1$ ). The resulting variance of signal plus noise is therefore

$$\text{variance}_{s+n} = C \Gamma_s T + \Gamma_d T + N_f^2 \quad (5)$$

The signal is quantified with a uniform analog-to-digital converter. The resulting quantization error has zero mean and a variance of  $261 e^-/\text{pixel}$ . Following analog-to-digital conversion and background subtraction of an independent frame, a pixel without signal has

$$\text{mean}_n = 0 \quad (6)$$

$$\text{variance}_n = 2\Gamma_d T + 2N_f^2 + 2N_q^2 \quad (7)$$

while the pixel with signal has

$$\text{mean}_{s+n} = C \Gamma_s T \quad (8)$$

$$\text{variance}_{s+n} = C \Gamma_s T + 2\Gamma_d T + 2N_f^2 + 2N_q^2 \quad (9)$$

Summing over a group of  $2 \times 2$  contiguous pixels that contains no signal,

$$\text{mean}_{4n} = 0 \quad (10)$$

$$\text{variance}_{4n} = 8\Gamma_d T + 8N_f^2 + 8N_q^2 \quad (11)$$

while a group containing some signal would have a sum of

$$\text{mean}_{4(s+n)} = \left( \sum_{i=1}^4 c_i \right) \Gamma_s T \quad (12)$$

$$\text{var}_{4(s+n)} = \left( \sum_1^4 c_i \right) \Gamma_s T + 8\Gamma_d T + 8N_f^2 + 8N_q^2 \quad (13)$$

For this system, with a spot size of approximately 0.9 pixel,  $\sum_1^4 c_i \cong 0.78$ .

The value of the sum of the group of four pixels containing the signal is denoted  $\text{SIG}_4$  where mean =  $\text{mean}_4(s+n)$  and variance =  $\text{var}_4(s+n)$ , and the value of any other group of four pixels, not containing the signal, is denoted as  $\text{NOISE}_4$  where mean =  $\text{mean}_{4n}$  and variance =  $\text{var}_{4n}$ . The total number of groups of  $2 \times 2$  contiguous pixels is  $(M-1)^2$ , or approximately  $M^2$  for  $M \gg 1$ . A miss occurs when one or more of the  $M^2$  groups of four pixels exceeds the value of  $\text{SIG}_4$  and is therefore chosen during acquisition. Using the union bound  $P_{\text{UB}}$  to express the probability of this event,  $P$ , we have

$$P \leq P_{\text{UB}} = M^2 \cdot \text{prob}[\text{SIG}_4 - \text{NOISE}_4 < 0] \quad (14)$$

Using central limit theorem arguments the statistics are approximated as Gaussian.  $P_{\text{UB}}$  therefore can be written as

$$P_{\text{UB}} \approx M^2 \frac{1}{\sqrt{2\pi}\Omega} \int_{-\infty}^0 e^{-\left[\frac{(x-0.78\Gamma_s T)^2}{2\Omega^2}\right]} dx \quad (15)$$

$$\text{with } \Omega = \sqrt{\text{var}_{4(s+n)} + \text{var}_{4n}}$$

$$= \sqrt{0.78\Gamma_s T + 16\Gamma_d T + 16(N_f^2 + N_q^2)} \quad (16)$$

which is equivalent to

$$P_{\text{UB}} \approx M^2 \frac{1}{\sqrt{2\pi}} \int_w^\infty e^{-\left[\frac{x^2}{2}\right]} dx \quad (17)$$

$$\text{with } w \equiv \frac{0.78\Gamma_s T}{\Omega} \quad (18)$$

For  $w \geq 2$ , the error function,

$$\text{erf}(w) \equiv \frac{1}{\sqrt{2\pi}} \int_w^\infty e^{-\left[\frac{x^2}{2}\right]} dx \quad (19)$$

can be approximated by [27]

$$\text{erf}(w) \approx \frac{1}{\sqrt{2\pi w}} e^{-\frac{w^2}{2}} \quad (20)$$

Therefore the expression for  $P$  can be similarly bounded as

$$P \leq M^2 \frac{1}{\sqrt{2\pi w}} e^{-\frac{w^2}{2}} \quad (21)$$

with

$$w = \frac{0.78\Gamma_s T}{\sqrt{\left[0.78\Gamma_s T + 16\Gamma_d T + 16(N_f^2 + N_q^2)\right]}} \quad (22)$$

provided  $w \geq 2$ .

(Equality with the bound would assume complete independence of each trial, defined as each contiguous  $2 \times 2$  pixel block within the array. There is, however, some correlation due to the fact that each pixel is included in four separate trials.)

### 7.3 EFFECTS OF JITTER

Jitter on the signal received at the CCD will result in spreading of the beam over the array with a commensurate power reduction in the  $2 \times 2$  pixel block containing the largest proportion of the signal.

An analysis was done [28] to predict the effect of sinusoidal jitter on the MAXBLOCK sum. The signal is modeled as a Gaussian intensity distribution with an  $e^{-1}$  width of  $\sigma$  beamwidths in each axis. The FWHM beamwidth of theunjittered beam is 0.9 pixel. The period of the jitter is assumed to be much shorter than the integration time. The  $x$  and  $y$  axis jitters have equal amplitudes and frequencies of  $\omega_1$  and  $\omega_2$  rad/s, respectively. Any phase difference is unimportant over a long integration time, so for simplicity a zero phase offset is assumed. With the beam centered within a pixel, the beam has a normalized intensity distribution given by

$$I(\theta_1, \theta_2, x, y) = e^{-\frac{\left[(x - A \cos \theta_1)^2 + (y - A \cos \theta_2)^2\right]}{2\sigma^2}} \quad (23)$$

where  $\theta_1 = \omega_1 t$  and  $\theta_2 = \omega_2 t$ . Over a long integration time this can be treated as a time average of the intensity:

$$\bar{I}(x, y) = \langle I(\theta_1, \theta_2, x, y) \rangle \quad (24)$$

$$= \int_0^{2\pi} \int_0^{2\pi} I(\theta_1, \theta_2, x, y) \frac{d\theta_1 d\theta_2}{2\pi 2\pi} \quad (25)$$

Using the Fourier representation of  $I(\theta_1, \theta_2, x, y)$  Equation (23) can be written as

$$I(\theta_1, \theta_2, x, y) = 2\pi\sigma^2 \int_{-\infty}^{\infty} e^{-jz_1 A \cos \theta_1 - z_1^2 \frac{\sigma^2}{2}} e^{jz_1 x} \frac{dz_1}{2\pi} \times \int_{-\infty}^{\infty} e^{-jz_2 A \cos \theta_2 - z_2^2 \frac{\sigma^2}{2}} e^{-jz_2 y} \frac{dz_2}{2\pi} \quad (26)$$

where  $z_1$  and  $z_2$  are the Fourier variables. The time average Equation (25) then becomes

$$\bar{I}(x, y) = \int_0^{2\pi} \int_0^{2\pi} 2\pi\sigma^2 \int_{-\infty}^{\infty} e^{-jz_1 A \cos \theta_1 - z_1^2 \frac{\sigma^2}{2}} e^{jz_1 x} \frac{dz_1}{2\pi} \times \int_{-\infty}^{\infty} e^{-jz_2 A \cos \theta_2 - z_2^2 \frac{\sigma^2}{2}} e^{jz_2 y} \frac{dz_2 d\theta_1 d\theta_2}{2\pi 2\pi 2\pi} \quad (27)$$

Using the identity

$$J_0(-Az) = \int_0^{2\pi} e^{-jAz \cos \theta} \frac{d\theta}{2\pi} \quad (28)$$

where  $J_0(q)$  is the zero order Bessel function of the first kind, then Equation (27) becomes

$$\bar{I}(x, y) = 2\pi\sigma^2 \int_{-\infty}^{\infty} J_0(-Az_1) e^{-z_1^2 \frac{\sigma^2}{2}} e^{jz_1 x} \frac{dz_1}{2\pi} \times \int_{-\infty}^{\infty} J_0(-Az_2) e^{-z_2^2 \frac{\sigma^2}{2}} e^{jz_2 y} \frac{dz_2}{2\pi} \quad (29)$$

containing Fourier integrals,  $I'(x)$  and  $I'(y)$ , defined as follows

$$I'(x) = \int_{-\infty}^{\infty} J_0(-Az_1) e^{-z_1^2 \frac{\sigma^2}{2}} e^{jz_1 x} \frac{dz_1}{2\pi} \quad (30)$$

$$I'(y) = \int_{-\infty}^{\infty} J_0(-Az_2) e^{-z_2^2 \frac{\sigma^2}{2}} e^{jz_2 y} \frac{dz_2}{2\pi} \quad (31)$$

which can be evaluated using fast Fourier transform (FFT) techniques.

Calculating the signal power in the  $2 \times 2$  block of pixels for the intensity distribution above is done by integration over the pixel area, yielding signal power proportional to

$$P \approx \int_{x_1}^{x_2} I'(x) dx \int_{y_1}^{y_2} I'(y) dy \quad (32)$$

The results are shown in Figure 16. The curves show the count for the  $2 \times 2$  pixel block within which the signal is centered when no jitter is present, as well as the count for  $2 \times 2$  pixel blocks in the proximity. The block within which the signal is centered in the absence of jitter is referred to as (0,0). The count in the initial pixelblock decreases as increased jitter spreads the signal to blocks in the proximity. Eventually, more signal is collected in a pixel block other than the original. Because the search for MAXBLOCK returns the address of the block containing the largest count, as jitter increases, the MAXBLOCK location changes. The MAXBLOCK sum, represented by the envelope of the curves, continues to decrease with increasing jitter amplitude.

This analysis assumes uncorrelated sinusoidal jitter in each axis. It is recognized that this model may not accurately represent jitter on the LEO platform. Unlike symmetric jitter, asymmetric jitter may result in offset errors in the estimate of the signal location with jitter amplitudes of less than 1 bw. For the expected jitter amplitudes of 0.5 to 1.5 bw rms, however, the spiral scan handoff routine makes such errors in the estimate of the location inconsequential.

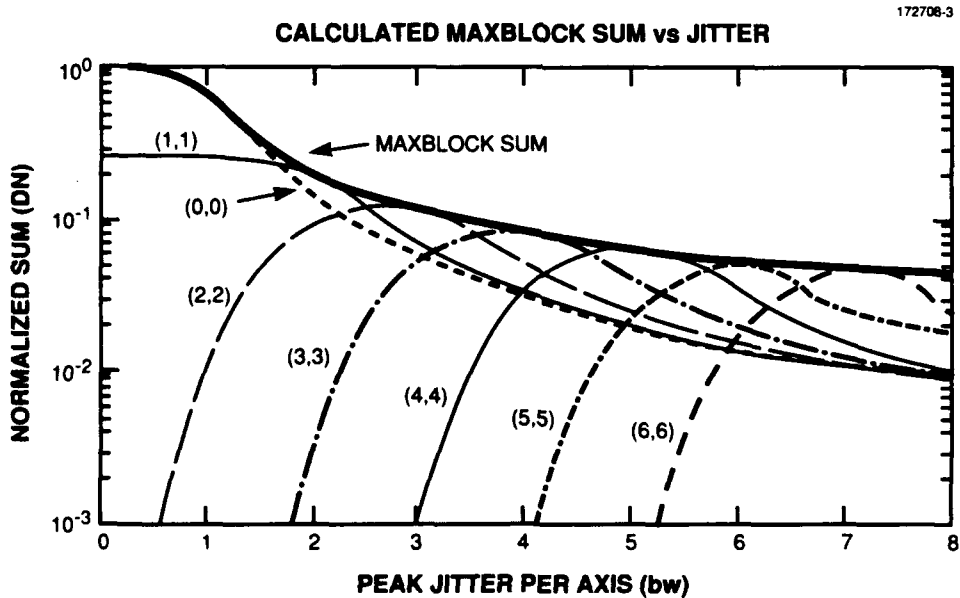


Figure 16. Maxblock sum vs jitter amplitude.

## 8. SPATIAL ACQUISITION SYSTEM RESULTS

### 8.1 SIGNAL ANGLE OF ARRIVAL vs DETECTED CCD POSITION

Signal angle of arrival was adjusted by varying the disturbance mirror position. Actual angle of arrival was proportional to commanded angle of arrival over a range greater than  $\pm 2$  mrad ( $> 400$  bw) with a maximum error of 0.1 bw, measured with an optical sensor. In order to calibrate the CCD linearity, CCD detected position was measured as a function of commanded signal angle of arrival and is plotted for the disturbance mirrors in Figure 17. For both disturbance and tracking mirrors, the error between the commanded mirror position and the position detected by the CCD was less than 0.3 pixel or approximately 0.33 bw.

### 8.2 SYSTEM GAIN

To calculate the acquisition system gain, the MAXBLOCK sum versus received power was measured. Each pixel value as well as the MAXBLOCK sum is represented in counts of digital numbers (DN) between 0 and  $2^{12}$ . At high DN, where we assume the SNR in the CCD is very high, most of the detected charge corresponded to photoelectrons, and very little to accumulated dark current. The slope of the MAXBLOCK sum vs incident power, combined with knowledge of the quantum efficiency (obtained in separate tests) allowed us to establish the system gain in electrons/DN. From the data in Figure 18, and using the measured quantum efficiency of 30 percent, the gain was determined to be 56 photoelectrons/DN. This gain is consistent for a previously measured [17] CCD output amplifier gain,  $K_{\text{CCD}}$ , of  $1.452 \mu\text{V}/e^-$ , and a gain of 30 through the analog electronics,  $K_{\text{analog}}$  with  $1 \text{ DN} = 10 \text{ V}/2^{12} = 2.44 \text{ mV}$  expressed as:

$$\text{photoelectrons / DN} = (2.44 \text{ mV / DN}) / (K_{\text{CCD}} \cdot K_{\text{analog}}) \quad (33)$$

### 8.3 CENTROID ALGORITHM GAIN DETERMINATION

When a suboptimum gain  $K$  was used in the centroid algorithm described in Section 7.1, the transfer function between mirror position and centroid location contained discontinuities as shown in Figure 19. By choosing gain factors either above or below the optimum we obtained transfer functions with either hop-back or staircase discontinuities. The  $K$  factor that yielded minimal deviation from a linear function was found to be between 0.65 and 0.68 in each axis. The discussion in Section 7.1 predicted that for an Airy disk with FWHM of 1 pixel width the gain factor  $K$  necessary to obtain the smallest maximum error is between 0.575 and 0.675. The smaller spot size of 0.9 pixel requires a smaller  $K$  value, between 0.525 and 0.625. The small discrepancy between observed and predicted transfer functions theoretically results in less than a 0.1 pixel maximum error [see Figure 15(b)] and is easily attributable to measurement error and a combination of beam aberration (resulting in a focal plane beam profile that was not exactly an Airy disk) and focus error.

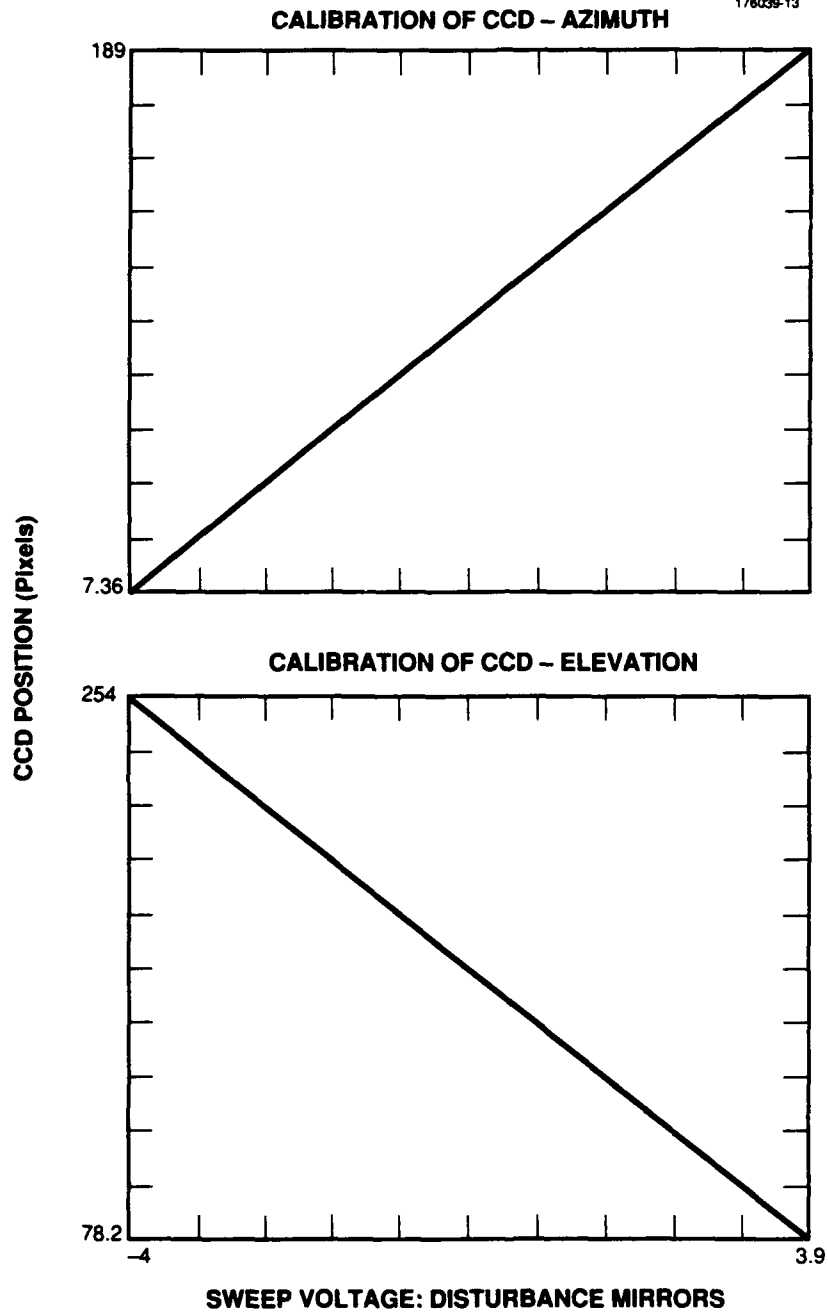


Figure 17. Measured CCD-sensed-position vs disturbance mirror angle.

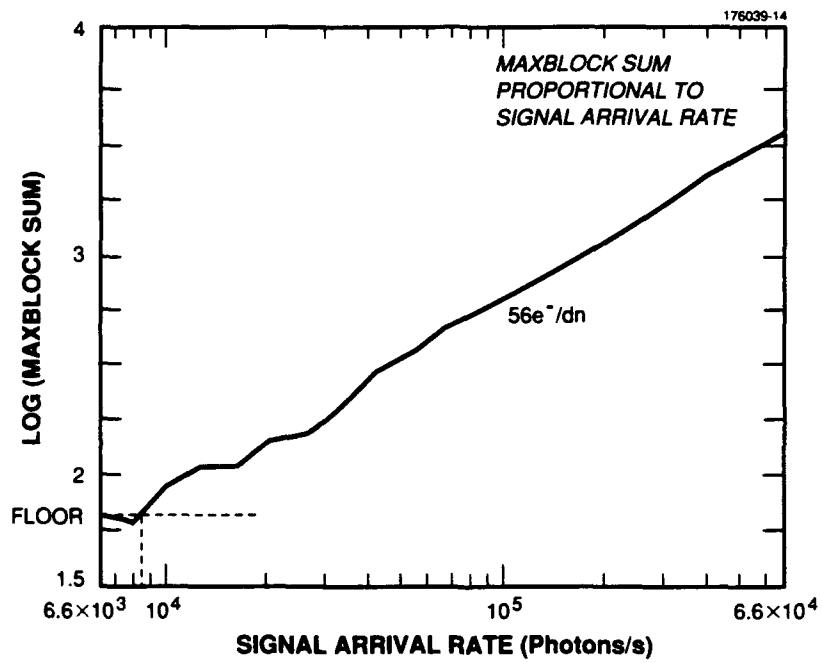


Figure 18. Measured maxblock sum vs signal arrival rate.

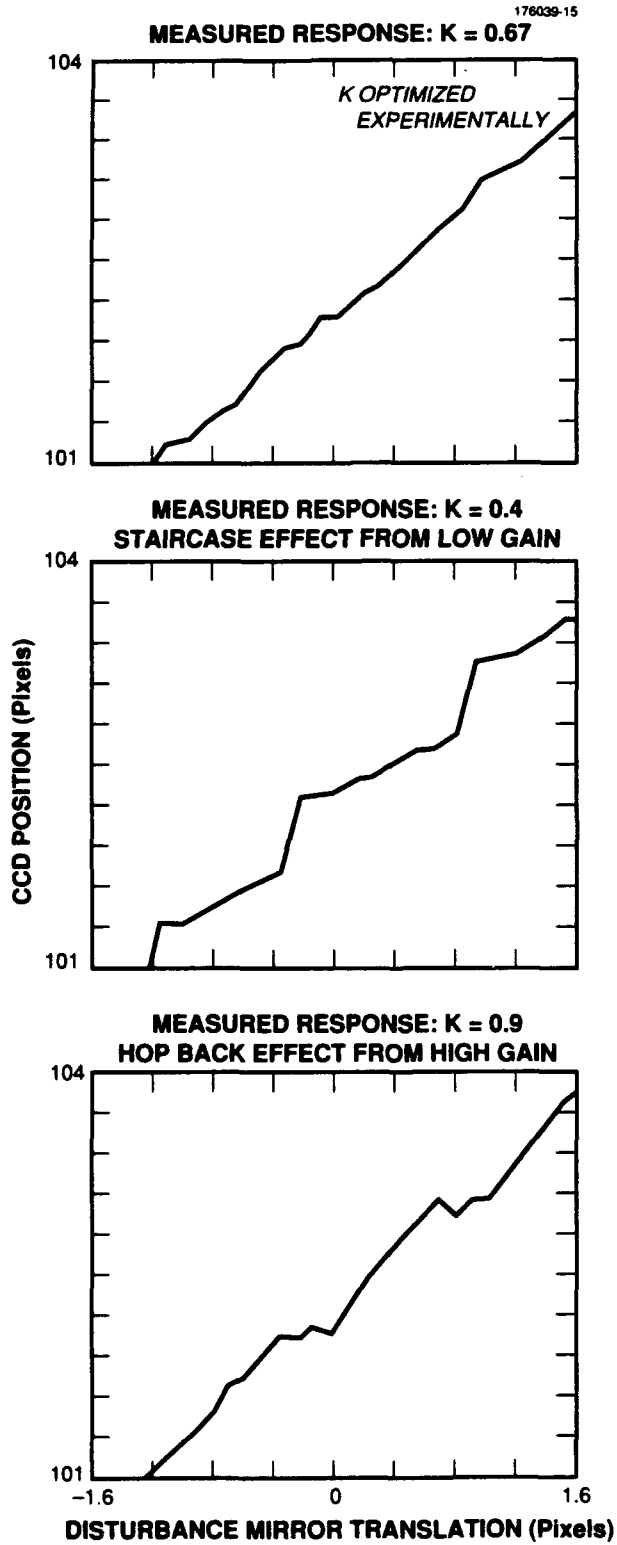


Figure 19. Measured CCD linearity for small (<2 bw) angular motions.

## 8.4 ACQUISITION SENSOR NOISE SOURCES

The extremely low signal level of the incoming beam forced tight constraints on noise levels of the readout and processing electronics in order to reliably find the correct MAXBLOCK location. Noise manifested itself in frame-to-frame variations of the detected charge per pixel when no signal was present. Looking at the variation in the output of single pixels for repeated background frames, it was noted that the CCD output could be corrupted by factors such as temperature variations (that affected the accumulated dark current), clock interference, and noisy power supply lines. In addition, certain "problem pixels" were identified that had particularly high noise levels. The next two sections discuss these factors.

### 8.4.1 Temperature

During overnight runs, bimodal distributions of pixel values were obtained that correlated well with models of distributions as a function of temperature change. The average value of a single pixel varied by more than 100 digital numbers or 5600 electrons. This was attributed to temperature-induced variations in the average dark current: a CCD's dark current level doubles for every 7°C. These data indicate that when utilizing frame subtraction it is necessary either to closely control the temperature of the CCD or to regularly update the background frame so that frame subtraction can effectively track changes in accumulated dark current due to gradual temperature changes. For this spatial acquisition system, updating the background frame as part of the acquisition algorithm added less than 2 s to the overall process and was preferable to temperature control.

### 8.4.2 Problem Pixels

A series of signal acquisitions was performed with the signal laser blocked. This showed that certain pixels within the  $200 \times 200$  subarray of the TK512M CCD were regularly selected as the MAXBLOCK location, despite frame subtraction. By taking many unilluminated frames and listing the MAXBLOCK locations that appeared most frequently, 11 chronic problem pixels, and an additional 15 troublesome pixels out of the total field of 40,000 pixels were identified.

The 26 problem pixels were located in 18 distinct regions within the  $200 \times 200$  pixel subarray. There were seven pixel pairs with the same row address and adjacent column address, and one pixel pair with the same column address and adjacent row address. Two of the eight pairs described contained a pixel with particularly high dark current. Of the 10 remaining problem spots, two were adjacent to individual pixels with high dark current in the same row, one was adjacent to a pixel with saturating dark current in the same column. The manufacturer determined that there were 15 "hot" pixels defects in the entire array with dark current 10 times the specification. Poor charge transfer efficiency between the last element in the serial register and the summing well of the output amplifier in the TK512M, previously reported [29], would explain noisy pixels resulting from the smearing of charge from the "hot" pixels to adjacent pixels during readout. Suboptimal clocking waveforms due to noise, pulse shape, or pulse

amplitude would also contribute to reduced charge transfer efficiency and increase smearing in both serial and parallel transfers. Further investigation could more accurately determine the noise source in these problem pixels.

Because of their high noise level these problem pixels caused frequent false acquisitions when acquiring at low light levels. This resulted in a minimum probability of error well above that which is predicted simply from the quantum shot noise of the dark current in a uniform array. The problem can be seen in the measured MAXBLOCK sum vs input photon arrival rate shown in Figure 20. The noise floor, below which the measured MAXBLOCK sum does not fall, is considerably above the predicted value for a uniform, dark-current-shot-noise-limited array. One technique was tested, then a second technique was implemented to reduce the effects of problem pixels.

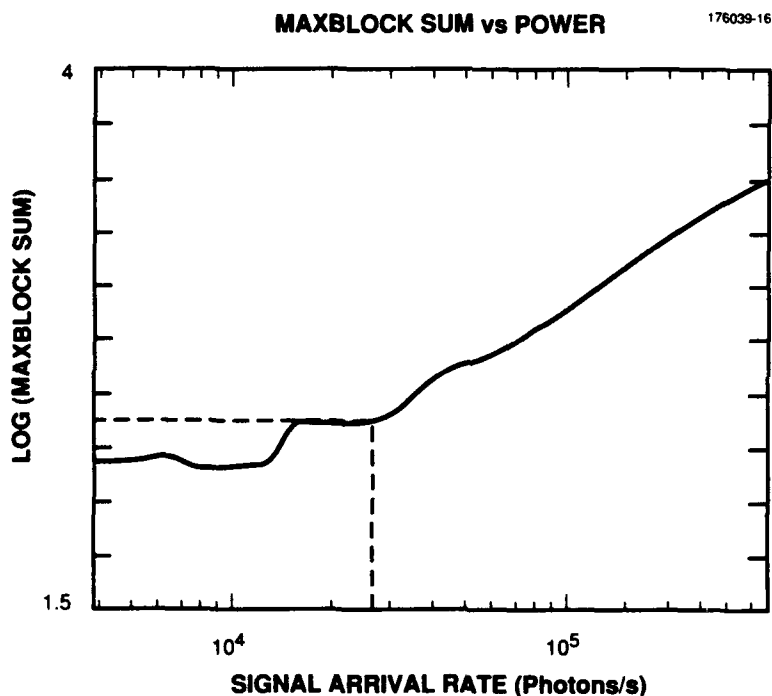


Figure 20. Measured noise floor without pixel masking.

First, as a test, the search region was limited to a small area free from problem pixels. With this technique a significant reduction in the noise floor was obtained. Using a  $10 \times 10$  pixel processing zone within which the signal was positioned, the correct location was selected for signal photon arrival rates as low as  $10^4$  photons/s. This indicated that the performance could be improved if all the pixels within the search area had a uniform response.

In order to eliminate problem pixels while maintaining the required  $200 \times 200$  pixel processing region, a "pixel masking" routine was developed. Masking forced the difference frame to zero at each problem pixel during the hardware subtraction routine. In this way the identified problem pixels no longer affected the selection of the MAXBLOCK location. This procedure was implemented in such a way that processing time was unaffected. The increase in probability of error can be bounded in the following way. The number of MAXBLOCK groups that may include at least one masked pixel is equal to four times the number of masked single pixels (10) and six times the number of masked paired pixels (8) for a total of 88. Assume, as an upper bound, the signal is not detected when it falls within a MAXBLOCK group that contains a masked pixel; the resultant increase in error rate is the ratio of affected MAXBLOCK groups to the total number of MAXBLOCK groups or  $2 \times 10^{-3}$ . This is an upper bound because in the worst case, when the signal is centered upon the single masked pixel, approximately 12 percent of the signal is still incident upon the surrounding pixels within the MAXBLOCK group. With the signal centered within the MAXBLOCK group 60 percent of the signal illuminates active pixels in the MAXBLOCK group despite a single masked pixel, and at least 40 percent of the signal is detected despite a masked pixel pair.

An estimate of the probability of successful acquisition was obtained by counting the number of missed acquisitions over many trials, while the signal was held fixed at a single location in the CCD. Trials were performed both with and without the pixel masking routine over a range of input photon arrival rates. The results are plotted in Figure 21. Pixel masking yielded as much as a 10 dB improvement at  $4 \times 10^4$  photons/s. Successful acquisition was obtained with a probability of 0.999 with as few as  $3 \times 10^4$  photons/s compared to approximately  $10^5$  photons/s without masking and with a probability of 0.99 with as few as  $1.3 \times 10^4$  photons/s rather than  $3.3 \times 10^4$  without masking.

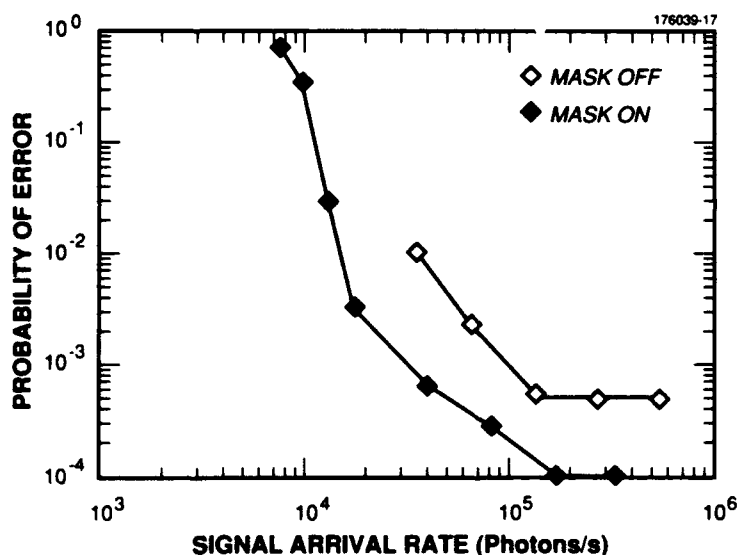


Figure 21. Measured probability of acquisition error, masked and unmasked.

Similar measurements were made when the signal was moved between each trial. The results were not noticeably different from when the signal was fixed at a single location.

### 8.5 ACQUISITION RANGE

The acquisition uncertainty region was mapped onto a  $200 \times 200$  pixel subarray of the CCD. It was confirmed that the system would operate throughout the range of the subarray by stepping the beam throughout the range by increments of just over one pixel, performing the acquisition sequence, and checking for successful pull-in by the tracker.

### 8.6 PROBABILITY OF ACQUISITION

Curves of theoretical and observed probability of error (where probability of error =  $1 - \text{probability of acquisition}$ ) are shown in Figure 22. Horizontal error bars on the experiment results reflect a 10 percent signal power measurement uncertainty. Vertical bars represent 90 percent confidence intervals for the error probability [30].

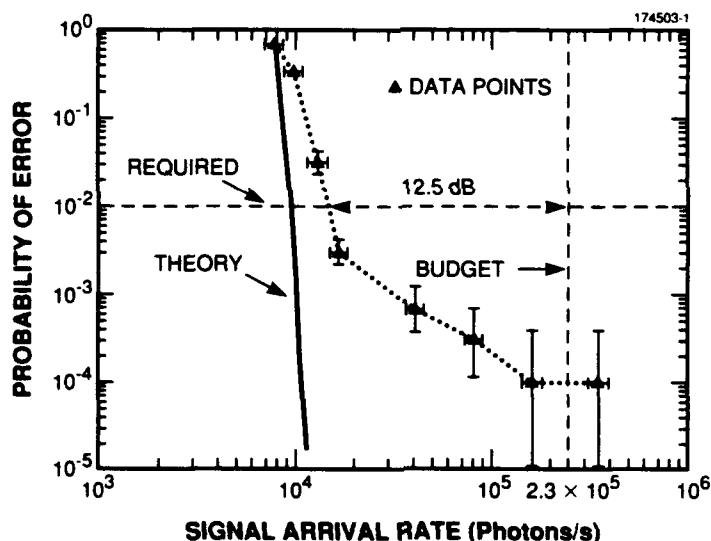


Figure 22. Theoretical vs measured probability of acquisition error.

The first theoretical curve, plotted using Equation (22), assumes that 78 percent of the arriving signal is contained within a  $2 \times 2$  pixel block and is calculated using a dark current density of 5685 electrons/pixel/s and a read noise of 78 rms electrons, measured in a separate characterization setup [17]. The difference between the theoretical and observed curves at the required probability of error of 0.01 is approximately 1.27 dB.

This discrepancy could be attributed to higher dark current and read noise in the experimental test setup than previously measured in the characterization test setup. For example, a 7°C temperature increase within the CCD housing (quite possible because the water cooling system, used during characterization, was not included in the experimental setup) would double the dark current. This would shift the theoretical curve by 0.81 dB. A 32 percent increase in read noise measured in the characterization test setup would shift the theoretical curve by 0.25 dB. This combined noise increase would result in a shift of the theoretical curve by 1.29 dB.

The results follow theoretical predictions quite well at power levels below  $3.7 \times 10^5$  photons/s after accounting for such an increase in the combination of dark current and read noise. Above that level, high gain in the analog signal conditioner preamplifier created an artificial dynamic range limitation due to saturation of the correlated double-sampler electronics. The probability of error continued to decrease with increasing power until all pixels in the  $2 \times 2$  block saturated, above  $7.4 \times 10^5$  photons/s. Despite the high-power level limitation the system exhibited better than the specified 0.99 probability of successful acquisition.

Most importantly, the CCD-based spatial acquisition system achieved the specified probability of successful acquisition of 0.99 with 12.5 dB of margin at the budgeted photon arrival rate for LITE,  $2.3 \times 10^5$  photons/s.

## 8.7 JITTER

Signal angle-of-arrival disturbances that are fast with respect to the CCD integration interval effectively increase the focal plane spot size above the diffraction-limited value (see Section 7.3). Such acquisition jitter was simulated by driving the azimuth and elevation disturbance mirrors simultaneously with nonharmonic sine waves. The disturbance periods in each axis were less than 1/50 of a CCD integration interval. The disturbance amplitudes ranged from 0 (no jitter) to 8.5 bw and were equal in amplitude for both axes.

Jitter is not likely to be symmetrical nonharmonic sinusoids. However, because the handoff algorithm includes a spiral scan of several beamwidths around the centroid location, handoff is expected to be successful as long as the acquisition error is less than 1 to 2 bw. The nonharmonic sinusoidal jitter was a convenient and analytically tractable jitter disturbance that adequately modeled the expected jitter during acquisition, given the relatively mild accuracy requirements on the acquisition process.

The MAXBLOCK sum, in normalized digital numbers, vs jitter amplitude is plotted in Figure 23. An increase in jitter resulted in a reduction in MAXBLOCK sum due to the smearing of signal power outside of the group of four MAXBLOCK pixels.

As jitter was increased to several beamwidths the signal was spread such that  $2 \times 2$  pixel groups other than the initial MAXBLOCK group, chosen in the presence of no jitter, contained the most amount of signal. The MAXBLOCK location therefore began to vary. These results are consistent with the theory presented in Section 7.3. Although for each trial the location of MAXBLOCK was near boresight, it was not consistently within pull-in range of our handoff algorithm for the largest values of jitter.

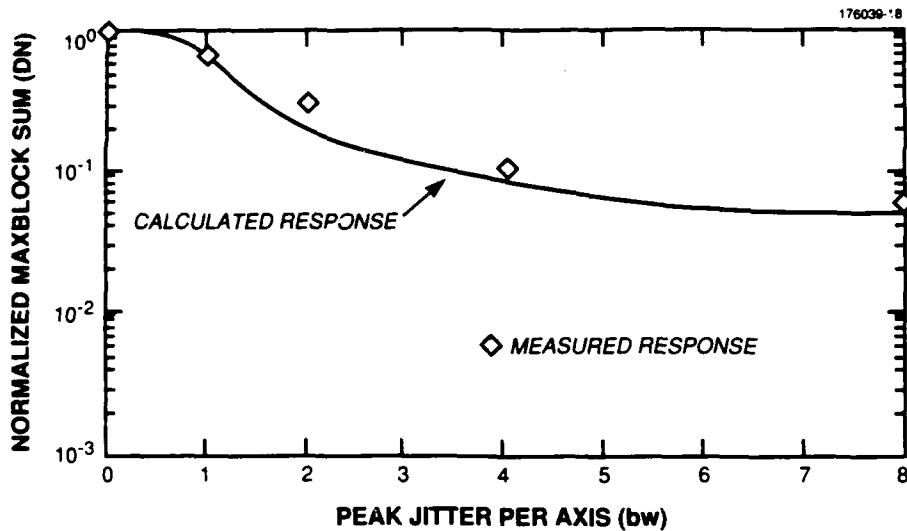


Figure 23. Effect of jitter on measured signal power.

The expected jitter levels during acquisition were described in Section 2.3.2. The high frequency portion of this spectrum (above 1 Hz) has an rms value of approximately 1 bw, which is well below the measured level of jitter in the demonstration system that caused erratic acquisition.

The low frequency jitter (below 1 Hz) on the ACTS satellite is expected to be less than 0.5 rms bw. Jitter on the LEO platform is assumed to be similar. The expected acquisition error due to these disturbances may be bounded by modeling all of the rms low frequency jitter as a single frequency term with an amplitude of 0.71 bw. The maximum error is then equal to the peak amplitude of this disturbance, which is still less than 1 bw. Therefore with confidence, the effects of the expected jitter (on the order of 1 bw) are modeled as a simple reduction in received power at the acquisition sensor, which should not degrade either the accuracy of the position estimate or the probability of successful acquisition by an unacceptable amount.

## 9. HETERODYNE SPATIAL TRACKING SYSTEM

This section describes the specific optical layout and control electronics that are used to implement the spatial tracking system. The demonstration system was built largely with off-the-shelf components, both optical and electronic, and was designed to illustrate the functionality of this system without considering packaging issues.

### 9.1 HETERODYNE RECEIVER AND SPATIAL TRACKING OPTICAL ELEMENTS

When the acquisition/tracking beamswitch (shown in Figure 3) was set to the spatial tracking position, the LO and signal beams were combined at the input to the communications receiver on a 50:50, polarization-independent beamsplitter, and equal length paths were provided to each of the p-type intrinsic-n-type (PIN) photodiodes that formed the balanced detector for the communications channel. The input combining beam splitter was specified to be as close to 50:50 as possible in order to equalize the LO power delivered to each half of the balanced communications receiver. The residual LO mismatch was corrected using a variable attenuator, formed from a quarter wave plate and polarizer in the appropriate arm of the balanced receiver. This was necessary to achieve adequate LO intensity noise cancellation [12]. If the beamsplitter mismatch is characterized by the ratio  $\delta$  of the reflection to transmission (or transmission to reflection) coefficients, defined so that  $\delta < 1$ , then the signal in one arm of the balanced receiver is attenuated by  $\delta^2$ , which is another reason to specify the beamsplitter to be as symmetric as possible. Note that beamsplitters are available that are sufficiently symmetric to reduce the loss of signal due to intensity matching to less than 0.3 dB, while the use of the balanced receiver may provide as much as 3 to 4 dB of improvement over an unbalanced receiver.

Separate and symmetric pickoffs were provided via polarizing beamsplitters for each (azimuth and elevation) track path. This configuration meant that in order to supply equal LO power to each track channel the input combining 50:50 beamsplitter had to be polarization independent. Half wave plates in the LO and signal paths, ahead of the combining beamsplitter, allowed individual control of the LO and signal polarization, and hence separate control of the LO and signal power split between the communications and track paths. These were adjusted so that nominally equal LO power was sent to each photodetector, ~2 mW, while the signal power was split approximately 80:10:10 between the communication, azimuth, and elevation paths, respectively.

Split detectors were formed in each track channel (Az,El) using a gold-coated knife edge (implemented with one edge of a pyramid splitter) and discrete PIN photodiodes because wideband (~1 GHz) segmented detectors with sufficiently small dead zones were not available.

The LO laser was identical to that used for the signal and was similarly collimated and circularized as described in Section 5.1.

### 9.2 DETECTOR/PREAMPS

Commercially available RCA CA-30917E wideband PIN detectors were used in both the communications and track channels. The outputs of the matched communications detectors and each track

photodetector were terminated with 50  $\Omega$  resistors. This increased the thermal noise too much to allow operation near the quantum shot noise limit but improved the flatness of the frequency response in each channel. These electrical signals were then amplified using discrete amplifier modules. Each module was formed from a pair of Watkins-Johnson RA-26 amplifiers and padded with wideband attenuators to yield a module gain of  $42 \pm 0.5$  dB from 50 to 1100 MHz. The noise figure of the front end detector/amplifier combinations could be improved to allow operation within 0.5 to 1 dB of the quantum shot noise limit by using hybrid detector/amplifier modules such as those described by Alexander [12]. Such amplifiers were not available to us at the time this experiment was performed.

### 9.3 SPATIAL TRACKING DEMODULATOR

The spatial tracking demodulator for the azimuth (elevation) channel was implemented as a high precision phase detector, designed to develop a baseband voltage proportional to the electrical phase difference between the two halves of the azimuth (elevation) track channel. In order to minimize the phase matching requirements within the tracking demodulator, a commutating architecture was chosen as illustrated in Figure 24. Details of the spatial tracking demodulator have been described elsewhere [31,32]; an overview will be given here, and a more complete analysis of the demodulator performance is given in Section 10.

For simplicity the following description will refer to the azimuth channel; the elevation channel is exactly analogous. The azimuth track channel outputs were alternately selected via a single-pole double-throw high speed RF switch, forming the commutated track signal. Both the commutated track signal and the communications signal (output of the balanced communications detector/amplifier front end) were then passed through input amplifiers that included automatic gain control (AGC). The front end AGC signal for all three amplifiers (communications, azimuth, elevation) was derived from envelope detection of the communications channel. The commutated azimuth signal was correlated with the communications signal in a wideband RF multiplier, which yielded an ac tracking error signal at the commutation frequency with an amplitude that was proportional to the phase difference between the two halves of the azimuth channel. The error signal was then bandpass filtered and synchronously demodulated to obtain a baseband tracking error signal.

As long as the communications channel SNR within the precorrelation noise bandwidth ( $\sim 1$  GHz) was greater than unity, the AGC in the input amplifiers was derived from the heterodyne IF signal, and the amplifier outputs were held constant despite any input signal optical power fluctuations. However, when the precorrelation communications channel SNR dropped below unity, the front end AGC level was based upon the input noise power, which is mostly LO shot noise in a well designed system (note that in the demonstration system the input noise was a combination of thermal and LO shot noise). When the front end AGC gain was fixed, the gain of the demodulator transfer function (volts/phase shift) was then linearly dependent on the input signal optical power.

In order to extend the effective AGC dynamic range to include operation when the input signal optical power dropped below the level where the precorrelation SNR was less than unity, additional normalization was implemented. This estimate of the signal power was developed at baseband using an

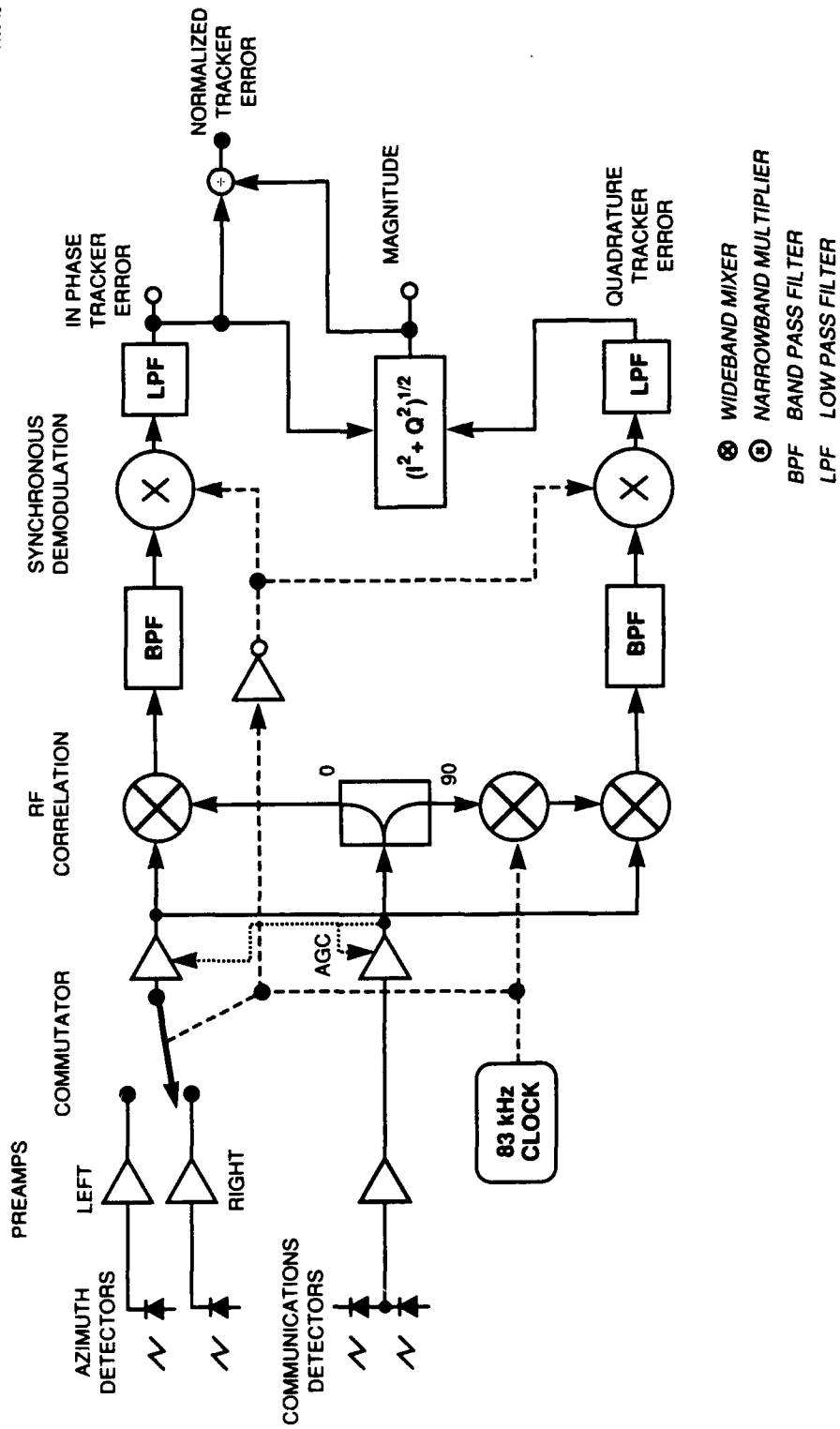


Figure 24. Commutated correlation demodulator architecture.

I and Q receiver. The portion of the receiver described in the previous paragraph developed the I signal. The Q signal was formed by multiplying the commutated azimuth signal by a 90°-shifted version of the communications signal. Note that the development of the wideband quadrature hybrid that provided the quadrature communication signal over a frequency band of 70 to 1170 MHz was one of the critical pieces of technology development necessary for the success of this processing scheme. The phase-shifted communication signal was also biphase modulated at the commutation frequency in order to produce a post-correlation signal at the commutation frequency, and not at dc. The subsequent bandpass filter and synchronous demodulation were identical to the I channel. The baseband normalization signal was then formed by using a commercially available analog function block to obtain  $(I^2 + Q^2)^{1/2}$ . The resultant two stage AGC normalization yielded a net transfer function of the spatial tracking demodulator electronics that was measured to have a mean gain of 1.38 V/radian. The transfer function gain varied by less than  $\pm 5$  percent over a 30-dB range of input optical power variation.

#### 9.4 BASEBAND SERVO ELECTRONICS

A block diagram of the baseband servo electronics, including the coarse track loop (acquisition, CCD-based), the heterodyne tracking loop, and the handoff circuitry used to transition between coarse and fine tracking, is shown in Figure 25. The coarse tracking function was a simple digital loop that used successive estimates from the CCD acquisition system to maintain the received signal at a position on the CCD that corresponded to the center of the receiver FOV. Positional updates were generated every 1.3 s. The digital filter used for the compensation element in the loop consisted of a single integrator (accumulator). The output of the accumulator was converted to an analog signal in a 12-bit digital-to-analog converter (DAC). The equivalent resolution of the DAC was 0.2 bw least significant bit.

Closed loop correction of angular misalignment (fine tracking) was performed by filtering the normalized angle error signal, developed at the output of the spatial tracking demodulator, and using the resultant signal to drive the TMBSs. The compensator filter in each track channel included two integrators for sufficient low-frequency rejection, a lead-lag network for good phase margin at loop crossover, and a fourth order notch filter at 11.4 kHz to keep from exciting the second resonance of the TMBSs.

#### 9.5 HANDOFF CIRCUITRY

The transition from coarse tracking, performed at a sub-Hertz update rate with tracking information derived from the CCD acquisition sensor, to fine tracking using the heterodyne tracking system is denoted as handoff. As discussed in Sections 2.3.2 and 7.3, the expected rms jitter during coarse acquisition and handoff is approximately 1 to 2 bw ( $\sim 0.5$  bw rms due to noise in the gyros used for short-term attitude stabilization, and  $\sim 1$  bw rms due to momentum wheel jitter). Because the coarse acquisition loop (described in Section 2.1) is limited in bandwidth by the 1 s integration time, little or none of the jitter above 0.5 to 1 Hz is rejected. Thus peak angular errors of at least 1 bw are likely to be present during the handoff process for times on the order of 1 to 10 ms. Because the heterodyne tracker will not reliably pull in a signal that is outside the receiver FOV, and because the tracker response time is on the order

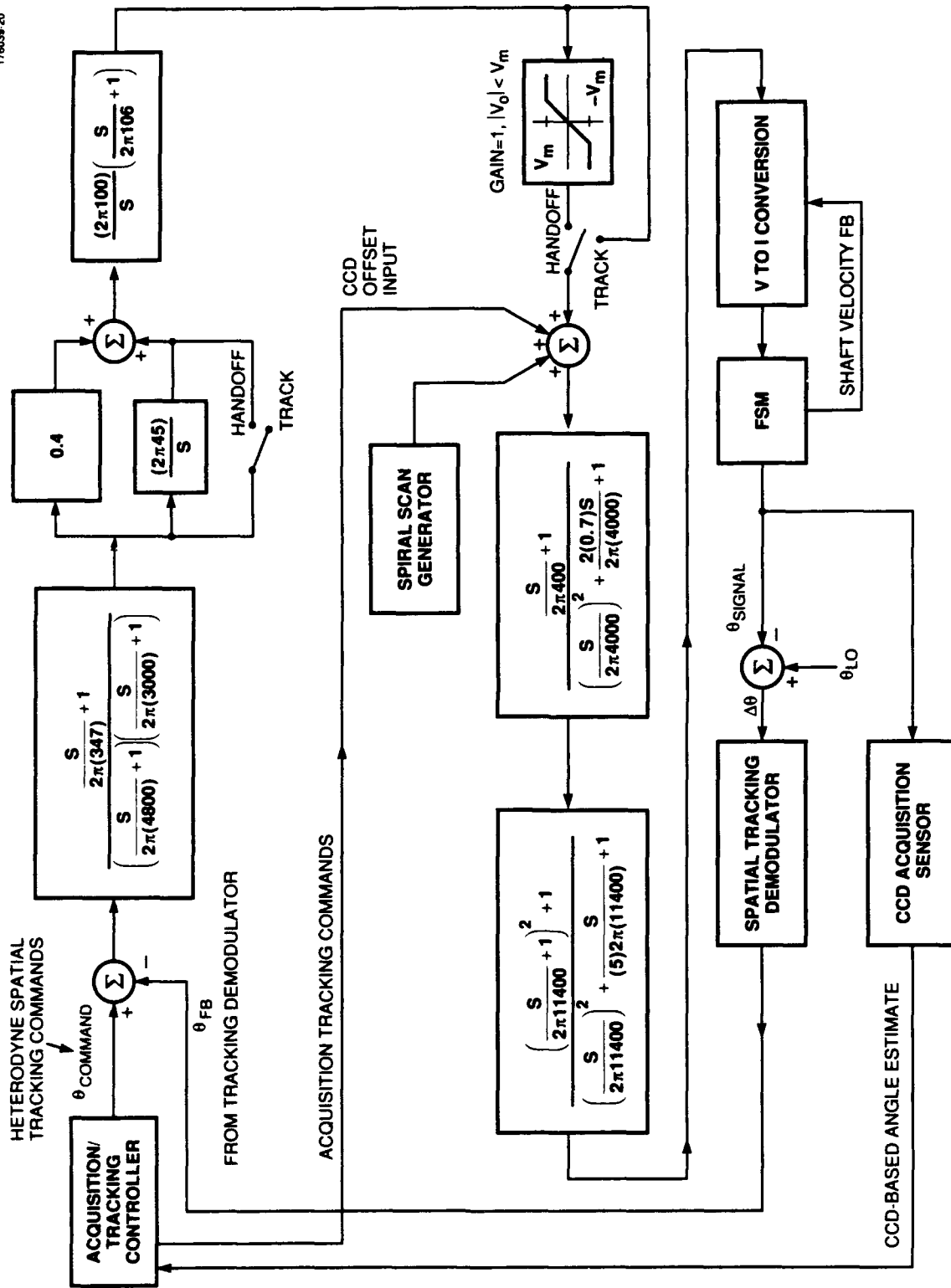


Figure 25. Spatial tracking compensator block diagram.

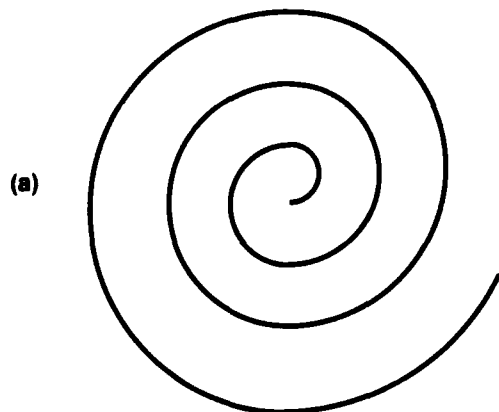
of a few milliseconds, such errors during handoff could cause large and potentially unrecoverable transients. Any bias errors in the acquisition process would tend to worsen this situation. Therefore, a technique for handoff was devised that would allow reliable handoff even when the signal did not initially illuminate the receiver FOV.

When the signal was outside the receiver FOV, an open loop spiral search centered on the acquisition location was initiated. As soon as the signal was directed to within the receiver FOV, control was transferred to the heterodyne tracker. Thus, for successful handoff it was necessary to first determine whether the signal was actually within the receiver FOV prior to transferring full control of the TMBSs to the heterodyne tracker.

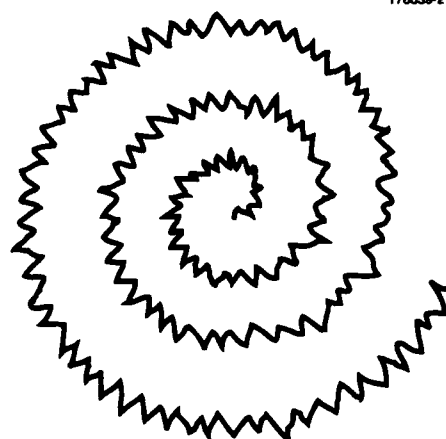
The traditional implementation for such a handoff (e.g., the LITE opto-mechanical system (OMS) acquisition and tracking system, [6]) is to develop an estimate of the received signal power and to transfer control of the tracking mirrors when the received signal power exceeds a predetermined level. The key to the success of this method is in picking the threshold level. Unfortunately, any thresholding scheme is subject to the problems associated with a simple threshold that cannot distinguish between a strong signal off boresight and a weak signal near boresight. In the static case this is not important, but for handoff of a moving signal (e.g., with a spiral scan or in the presence of jitter) it may be possible to pull in a weak signal near boresight, while a strong signal at the edge of the receiver FOV may move out of the FOV before the tracking loop can capture it [33].

The handoff method implemented for the two-axis tracker described here, first proposed by Kaufmann [34], modified the usual thresholding scheme to increase robustness. Instead of completely disabling the tracking loop during the open loop scan at the beginning of the handoff transition, the tracking loop output was limited to a voltage equivalent to an angular excursion of  $\pm 1$  to 2 beamwidths, which was called the authority limit. This limited output was added to the open loop scan. An ideal noiseless spiral scan is illustrated in Figure 26(a). As the signal was scanned the tracking loop was driven by noise as long as the signal was outside the receiver FOV, which led to modified spiral scan shown in Figure 26(b). When the signal was scanned to within the authority limit of the tracking loop, the loop acted to center the signal, in effect counteracting the spiral scan. When the signal was centered the authority limits were opened to allow the loop full authority and fine tracking commenced. The performance of this technique is presented in Section 11.9.

There are two advantages to this method relative to the traditional approach. First, the threshold problem is greatly simplified to merely detecting the minimum signal power that corresponds to the lowest received optical power at which tracking can take place, when the signal is centered on boresight. The question of which conditions will potentially lead to a large enough detected signal to trigger a threshold, but will not lead to a successful pull-in, need not be determined exhaustively a priori, since the system will automatically fail gracefully in those cases (i.e., the spiral scan will continue without interruption until the signal sweeps close enough to boresight to pull in). Second, this method guarantees that the compensator integrators are automatically set to the correct voltage to minimize any transient when control is passed to the tracking loop.



(a)  
**SPIRAL SCAN  
WITHOUT  
NOISE**



(b)  
**SPIRAL SCAN  
WITH LIMITED  
AMPLITUDE NOISE**

Figure 26. Handoff spiral scan.

## 9.6 COMMUNICATIONS LINK

In order to demonstrate the performance of an integrated communications receiver with active spatial tracking, a data link was established using a binary FSK modulator (operating at 110 Mb/s) and a matched filter demodulator. Binary FSK modulation was achieved by varying the current of the signal laser, which in turn varied the optical frequency. A five-section equalization network similar to those developed in earlier work [35] was included in the modulation path to flatten the signal laser FM response. The tone spacing was set to 220 MHz.

The receiver included a frequency tracker, which varied the LO laser current in order to stabilize the lower frequency tone (of the two heterodyne IF tones) at 325 MHz. The receiver used a pair of matched filters to determine which tone was being sent. The matched filter bandwidths were designed for an IF linewidth less than 12 to 15 MHz. Unfortunately, the measured IF linewidth of the demonstration system was 22 MHz, which degraded communications performance by creating a BER floor near  $10^{-4}$ . The relatively large IF linewidth had no effect on the tracking performance because the tracking demodulator processed the entire information bandwidth and was essentially insensitive to where the heterodyne signal might be located within that band.

## 10. THEORY OF OPERATION FOR THE HETERODYNE SPATIAL TRACKER

In this section the expressions for the photocurrents both in the azimuth segmented detectors and at the output of the balanced communications detectors are derived. The transfer function between optical angle error (between the LO and signal optical beams) and the normalized output voltage of the tracking demodulator is developed. This quantity is commonly referred to as the tracking discriminant. Finally, an analysis of the noise performance of the track channels, including the effects of the commutating, correlation processing is presented.

Throughout this section the performance of the azimuth track channel only is derived. The elevation channel is exactly analogous. Also, the azimuth track channel power is defined as the total LO or signal power at the azimuth beamsplitter. Similarly, the communications channel power will refer to the LO or signal optical power arriving at both communications detectors. Finally, a beamwidth is defined as the full angular width between the half maximum points of the far field intensity pattern of the signal beam and is equal to  $3.24/ka$  (radians) for a uniform circular beam of radius  $a$ , where  $k$  is  $2\pi/\lambda$ .

### 10.1 DEFINITION OF GEOMETRY

The geometry for the track channels is shown in Figure 27(a), where a Gaussian LO is normally incident upon a split detector, and a truncated plane wave signal beam overlaps the LO but is angularly misaligned from the LO by an angle  $\Delta\theta$ . This same geometry applies to the communication channel, except that the detectors are not segmented. The coordinate system is illustrated in Figure 27(b), where the  $k$  vector,  $\vec{k}_s$ , is projected into the plane of the detector. For a nonzero angular misalignment  $\theta$  there will be nonzero components of the signal  $k$  vector in the plane of the detector. This projection of  $\vec{k}_s$  is written in polar coordinates,  $k_r, \phi_0$ , in order to exploit the circular symmetry of the beams, where  $\vec{r}$  is the position vector within the detector plane.  $\phi_0 = 0$  corresponds to a beam angular deviation only in the  $x$  direction while  $\phi_0 = \pi/2$  corresponds to a beam angular deviation only in the  $y$  direction. For small angular misalignments the azimuth and elevation disturbances may be considered orthogonal (i.e.,  $\theta^2 = \theta_x^2 + \theta_y^2$ ).

### 10.2 DERIVATION OF IF HETERODYNE CURRENTS

By looking at the integral of the Poynting vector of the combined LO and signal beams normal to the plane of each detector, an expression can be derived for the electrical IF signal at the detector outputs. For any position  $\vec{r}$  in the detector plane, let the  $\vec{E}$  fields of the LO and signal beams be characterized as follows:

the signal beam at the split detector (Az or El),

$$\vec{E}_{S,track} = \sqrt{2\gamma P_C z_0} A_S(x, y) e^{-j(\omega_s t - \vec{k} \cdot \vec{r})} \quad (34)$$

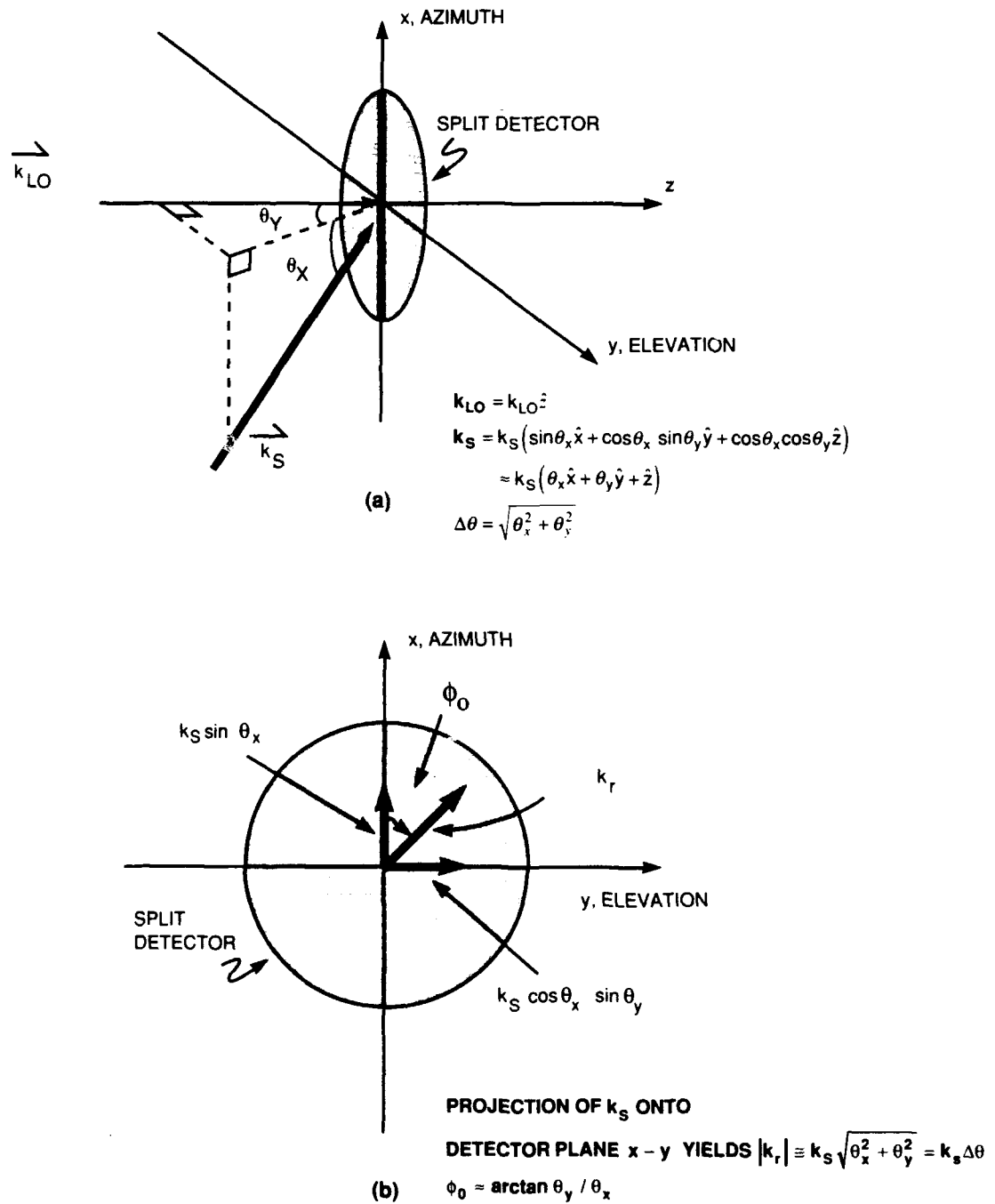


Figure 27. Geometry for heterodyne detection in the pupil plane.

the LO beam at the split detector (Az or El),

$$\bar{E}_{\text{LO,track}} = \sqrt{2 P_{\text{LO}} z_0} A_{\text{LO}}(x, y) e^{-j\omega_L t} \quad (35)$$

the signal beam at each communication detector,

$$\bar{E}_{S,\text{comm}} = \sqrt{P_C z_0} A_S(x, y) e^{-j(\omega_S t - \vec{k} \cdot \vec{r})} \quad (36)$$

and the LO beam at each communication detector,

$$\bar{E}_{\text{LO,comm}} = \sqrt{P_{\text{LO}} z_0} A_{\text{LO}}(x, y) e^{-j(\omega_L t + \pi/2)} \quad (37)$$

where  $\gamma$  is the ratio of track signal optical power to communications signal optical power, and  $A_{\text{LO}}(x, y)$  and  $A_S(x, y)$  are the field amplitudes of the LO and signal beams, respectively, normalized such that

$$\int_{-\infty}^{\infty} dx \int_{-\infty}^{\infty} dy |A_{\text{LO}}(x, y)|^2 = \int_{-\infty}^{\infty} dx \int_{-\infty}^{\infty} dy |A_S(x, y)|^2 = 1 \quad (38)$$

The 90° phase shift between the LO field in the communications channel and the LO field in the track channel is introduced optically, via a quarter wave plate ahead of the combining beamsplitter. The net effect is to make the communications and sum track channel IF photocurrents differ in phase by 90°. The phase shift is introduced optically (prior to photodetection) in order to make the slope of the tracking discriminant independent of the sign of  $\omega_{\text{LO}} - \omega_S$ .

In general, the IF heterodyne current may be written as

$$i_{\text{HET}}(t) = \frac{e\eta}{h\eta z_0} \text{Re} \left\{ \int_{\text{DETECTOR}} E_S(\vec{r}) E_{\text{LO}}(\vec{r}) e^{j(\Delta\omega t - \vec{k} \cdot \vec{r})} dA \right\} \quad (39)$$

For the specific case where the signal is a circularly truncated plane wave,  $A_S(r, \phi) = (1/a\sqrt{\pi})\text{circ}(r/a)$ , and the LO is Gaussian,  $A_{\text{LO}}(r, \phi) = \sqrt{2/\pi w^2} \exp(-r^2/w^2)$ , and the beams are matched such that  $a = w$ , then the heterodyne IF current over one azimuth detector segment may be written as

$$i_{\pi}(t) = \frac{2\sqrt{2}e\eta}{h\nu\pi} \sqrt{\gamma P_C P_{\text{LO}}} \cos \Delta\omega t \int_{0=r}^1 dr \int_{\phi=-\pi/2}^{\pi/2} r e^{-r^2} e^{-j(3.24 \theta r \cos \phi)} d\phi \quad (40)$$

where the angular mismatch  $\theta$  is in units of angular beamwidths. The current in the left azimuth detector,  $i_{\text{lt}}$ , may be obtained by changing the limits on  $\phi$  in Equation (40) to  $\pi/2 < \phi < 3\pi/2$ , and when the LO and signal beams overlap perfectly,  $i_{\text{lt}}$  is the complex conjugate of  $i_{\pi}$ . It is convenient to write Equation (40) as

$$i_{\pi}(t) = I [m(\theta) \cos \Delta\omega t + q(\theta) \sin \Delta\omega t] \quad (41)$$

$$I = \frac{e\eta}{h\nu} \sqrt{\gamma P_C P_{\text{LO}}} \quad (42)$$

$$m(\theta) = 2\sqrt{2} \int_{r=0}^1 r e^{-r^2} J_0(3.24 \theta r) dr \quad (43)$$

$$q(\theta) = \frac{8\sqrt{2}}{\pi} \int_{r=0}^1 r e^{-r^2} \sum_{n=0}^{\infty} \left[ \frac{J_{2n+1}(3.24 \theta r)}{2n+1} \right] dr \quad (44)$$

Figure 28 plots  $m(\theta)$  (which is proportional to the sum channel output) and  $q(\theta)$ , which is proportional to the track difference channel output, vs  $\theta$ . More conveniently, by setting  $m(\theta)/m(0) = \cos \zeta$  and  $q(\theta)/m(0) = \sin \zeta$ , we can also write

$$i_n(t) = m(0)I \cos(\Delta\omega t - \zeta) \quad (45)$$

$$\zeta = \arcsin \left( \frac{q(\theta)}{m(0)} \right) \quad (46)$$

The communications channel IF photocurrent may now be written by inspection, remembering that it will be similar in form to the track channel sum current, but shifted by  $90^\circ$

$$\begin{aligned} i_C(t) &= \frac{j}{\sqrt{\gamma}} (i_n + i_h) \\ &= \frac{2I}{\sqrt{\gamma}} m(\theta) \sin \Delta\omega t \end{aligned} \quad (47)$$

Note that  $m^2(\theta)$ , from Equation (43), is often called the heterodyne mode matching efficiency [36], and for our particular example of a truncated plane wave signal of radius  $a$  and Gaussian LO with  $1/e^2$  intensity radius  $a$ ,  $m^2 = 0.8$ . If the Gaussian LO is also truncated at radius  $a$ ,  $m^2$  increases to 0.92. The mode matching efficiency is always less than or equal to unity, and is only unity when the LO and signal beams have identical profiles, within a multiplicative constant.

### 10.3 CORRELATION-BASED TRACKING DISCRIMINANT NEAR BORESIGHT

Correlation-based processing using single sideband (SSB) correlation has been discussed previously for both pupil [14] and focal [15,37] plane heterodyne spatial trackers. The signal processing we describe reduces the complexity of the SSB approach, with similar performance. The following description is a summary of the analyses presented by Kaufmann [38] and Hodsdon [37]. A more complete derivation is given in Appendix C. Only the derivation for the azimuth channel is presented; the elevation channel is exactly analogous.

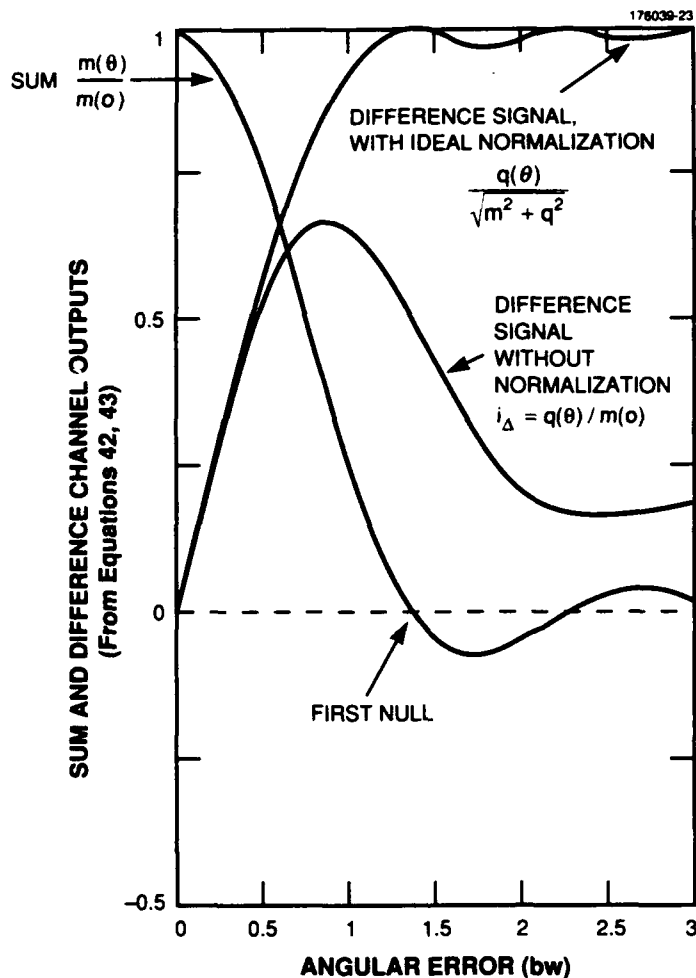


Figure 28. Sum channel magnitude and tracking discriminant vs angular error.

The communications channel photocurrents are amplified and split into an I and Q signal using a wideband quadrature hybrid. Expressions of the resultant voltages, including noise terms follow the I channel voltage,

$$v_{c,I}(t) = \frac{2 \text{Im}(\theta)}{\sqrt{\gamma}} \sin \omega t + n_C(t) \quad (48)$$

and the Q channel voltage,

$$v_{c,Q}(t) = \frac{2 \text{Im}(\theta)}{\sqrt{\gamma}} \cos \omega t + n_C(t) \quad (49)$$

Rewriting Equation (45) to include both the track channel noise terms and the commutation terms  $R'$  and  $L'$ , and setting the term  $\zeta \approx K_D \theta$ , obtain

the voltage in the left azimuth channel,

$$v_{\text{left}}(t) = L' \left[ m(0)I \cos(\omega t + K_D \theta_{\text{bw}}) + n_L(t) \right] \quad (50)$$

and the voltage in the right azimuth channel,

$$v_{\text{right}}(t) = R' \left[ m(0)I \cos(\omega t - K_D \theta_{\text{bw}}) + n_R(t) \right] \quad (51)$$

The gain  $K_D \approx 1.24$  radians/bw may be obtained by linearizing  $q(\theta)/m(0)$ , Equation (46), for small  $\theta$ . Note that  $n_c(t)$ ,  $n_L(t)$ , and  $n_R(t)$  are all uncorrelated, additive, white, Gaussian noise terms with two-sided spectral densities  $N_o/2$ ,  $N_o/4$ , and  $N_o/4$ , respectively. In a system dominated by the LO quantum shot noise  $N_o = 2ei_{\text{dc}} = 2e^2 \eta P_{\text{LO}}/h\nu$ . The commutation in the track channel is modeled as a multiplication of the azimuth signals by an offset square wave, so that  $R'$ ,  $L'$  are written as

the right track commutation function,

$$R' = \left( \frac{1}{2} + \sum_{k=1}^{\infty} B_k \cos(k\omega_s t) \right) \quad (52)$$

and the left track commutation function,

$$L' = \left( \frac{1}{2} - \sum_{k=1}^{\infty} B_k \cos(k\omega_s t) \right) \quad (53)$$

for

$$B_k = \frac{\sin \frac{k\pi}{2}}{\frac{k\pi}{2}} \quad (54)$$

Following the commutated correlation processing illustrated in Figure 24, it can be shown (Appendix C) that the normalized output of the I channel is given by

$$\bar{V}_o(\theta) = K_D \theta + \frac{\pi \sqrt{\gamma}}{4 m^2(0) I^2} \{ n_{\text{sxN}}(t) + n_{\text{nxN}}(t) \} \quad (55)$$

where  $I$  was defined in Equation (42),  $m(\theta)$  was defined in Equation (43), and  $K_D \theta \ll 1$ . The noise terms,  $n_{\text{sxN}}(t)$  and  $n_{\text{nxN}}(t)$ , are discussed in Section 10.4. The normalization is implemented by dividing the I channel output by the square root of the sum of the squares of the I and Q outputs.

## 10.4 NOISE EQUIVALENT ANGLE FOR COMMUTATED, CORRELATED PROCESSOR

The noise analysis for both pupil and focal plane heterodyne spatial trackers with correlation processing has been previously presented [14,15]. The noise equivalent angle is the offset angle  $\theta_{NEA}$ , which in a noise-free system would yield the same output as the rms noise voltage in the real system. From Equation (55) and following some manipulation (see Appendix C),  $\theta_{NEA}$  may be written as

$$\begin{aligned}\theta_{NEA} &= \left( \text{var} \left( \frac{\bar{V}_o(\theta)}{K_D} - \theta \right) \right)^{1/2} \\ &= \frac{\pi}{2 K_D} \left( \frac{F}{CNDR_{\text{track}}} \right)^{1/2} \left( 1 + \frac{W}{CNDR_{\text{comm}}} \right)^{1/2}\end{aligned}\quad (56)$$

where  $F$  is the single-sided noise equivalent bandwidth of the closed loop tracking servo,  $W$  is the single-sided noise equivalent bandwidth of the input electronics before correlation, and  $CNDR_{\text{comm}}$  and  $CNDR_{\text{track}}$  are the carrier-to-noise density ratios in the communications and track (sum) channels, respectively. In a shot-noise-limited system,  $CNDR_x$  is simply  $\eta m^2 P_x / h\nu$ , where  $\eta$  is the quantum efficiency of the photodetector,  $h$  is Planck's constant,  $\nu$  is the optical frequency,  $m^2$  is the spatial mode matching parameter, and  $P_x$  is the optical power incident onto the photodetectors in channel  $x$ . The noise equivalent angle (NEA) in Equation (56) is  $\pi/2$  greater than in a simple correlation processor. Note that as discussed in Section 11.6, by building a second identical correlation channel in which the commutation signals are inverted with respect to the first, and subtracting the outputs, the  $\pi/2$  factor in Equation (55) could be reduced to  $\pi/(2\sqrt{2}) = 1.11$ . For comparison, the expression for the NEA of a system in which the frequency of the received tone is known exactly, i.e., the RF demodulation is done coherently, [14] is given by

$$\theta_{NEA} = \frac{1}{K_D} \left( \frac{F}{CNDR_{\text{track}}} \right)^{1/2} \quad (57)$$

## 10.5 EFFECTS OF LO ANGULAR DISTURBANCES

An important difference between detection in the pupil plane and in the focal plane which has not previously been noted is the sensitivity of the two methods to angular movement of the LO beam. In a typical closed loop tracking system the signal beam angle of arrival is adjusted to maintain zero error signal at the output of a segmented detector in the track channel. Proper choice of an error signal ensures that when the error is driven to zero the angular misalignment between the LO and signal beam is also minimized. For focal plane detection, the usual error signal is based upon the amplitude difference between the heterodyne current in each half of a segmented detector. Unfortunately in such a system zero error signal only corresponds to perfect signal-LO beam angular alignment when the LO is centered.

Conversely, for detection in the pupil plane, where the discriminant is based upon differential phase between the heterodyne outputs of the detector segments, zero error signal corresponds to perfect signal-LO angular alignment even when the LO is not centered on the segmented detector.

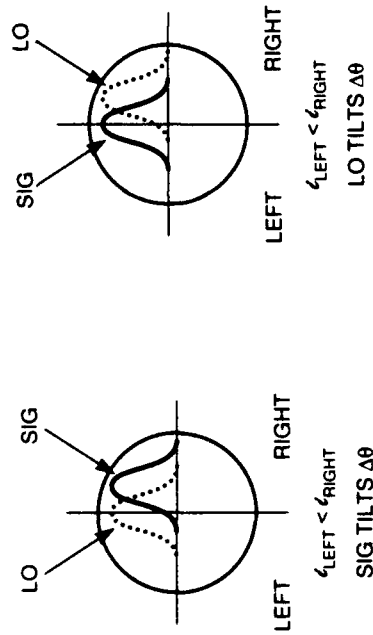
This is illustrated with a comparison of a single axis pupil and focal plane system as shown in Figure 29. Both systems employ segmented detectors (bi-cells) and derive a discriminant by differencing the heterodyne currents from the two halves of the split detector. In the focal plane the incremental change in the IF current difference due to LO angular tilt has the same sign as the incremental change due to signal angular tilt. This is because the IF current in each detector segment is a function of the product of LO and signal power incident on the segment. In the example illustrated in Figure 29, a positive tilt in either the LO or signal acts to increase the IF current in Segment A and decrease the IF current in Segment B. A closed loop tracking system that adjusts the signal angular tilt to maintain equal IF current in each detector segment would then move the signal beam in the opposite direction of any LO tilt, which acts to amplify LO angular disturbances.

By contrast, in the pupil plane the incremental change in differential current output due to LO tilt is opposite in sign from that induced by the same tilt in the signal beam. The tracking information in the pupil plane is derived from the phase difference between the IF currents, and the sign of that phase difference can be predicted based on whether the LO optical phase front leads or lags the signal across each detector segment. A positive LO tilt then clearly introduces the opposite IF phase change from a positive signal tilt. Thus a closed loop tracking system based upon detection in the pupil plane would tend to adjust the signal beam tilt to follow LO disturbances.

Both pupil and focal plane detection are relatively insensitive to beam-walk-induced offset errors. In the focal plane case, beam walk produces relative translation at the focusing lens ahead of the detector and thus phase shift but no translation in the focused intensity profile. The resultant heterodyne current outputs from the detector segments will differ in phase, but not in amplitude. In focal plane detection the RF processing is designed to detect differential amplitude differences in the heterodyne currents and is relatively insensitive to phase differences. Beam walk will only reduce the discriminant gain and does not introduce an offset error. Analogous arguments may be invoked to show that in pupil plane detection, beam walk produces only amplitude differences, to which the RF processing is largely insensitive.

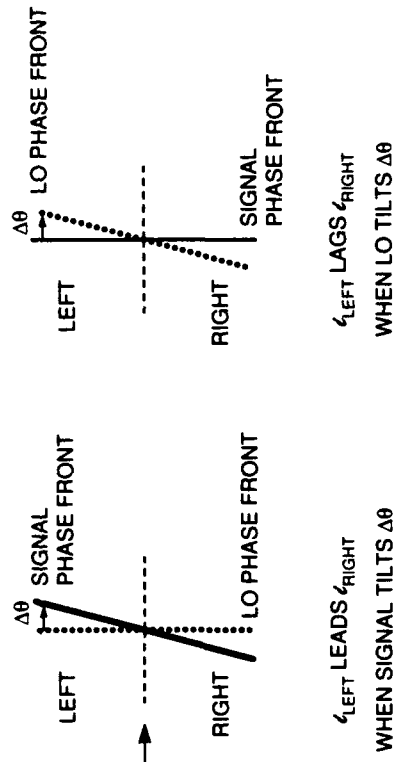
The perceived advantage of pupil plane detection vs focal plane detection may be reduced, however, upon consideration of a duplex link. In a system in which the pointing of the outgoing beam is referenced to the incoming signal, any correction by the FSM to track an LO-induced angular misalignment (between the incoming signal and the LO) simultaneously mispoints the outgoing beam by the same amount. Thus for a communication link between two platforms A and B, the angular deviation of the LO in the receiver on platform A is translated into a reduction in the power with which platform B is illuminated. In such a case, as for focal plane detection, a separate LO angular stabilization loop is necessary. Note that a coordinated closed loop point-ahead system could track out drifts.

**FOCAL PLANE**



FOR  $\Delta V = \frac{\epsilon_L - \epsilon_R}{\Sigma_i}$   
**SAME SIGN FOR  $\frac{\Delta V}{\Delta \theta_{SIG}}$  AND  $\frac{\Delta V}{\Delta \theta_{LO}}$**

**PUPIL PLANE**



FOR  $\Delta V = \frac{\epsilon_L - \epsilon_R}{\Sigma_i}$   
**OPPOSITE SIGN FOR  $\frac{\Delta V}{\Delta \theta_{SIG}}$  AND  $\frac{\Delta V}{\Delta \theta_{LO}}$**

Figure 29. Effects of LO motion on focal plane and pupil plane spatial trackers.

## 11. SPATIAL TRACKER AND HANDOFF RESULTS

This section summarizes the results of the various characterization tests of the heterodyne tracker and acquisition/tracking handoff procedure. For each test the method is described, then the measured data are presented.

### 11.1 BEAM CHARACTERIZATION

Hitachi HLP-8314E lasers operating at a nominal wavelength of  $0.86 \mu\text{m}$  and in a single longitudinal mode served as the signal and LO sources. The laser outputs were collimated and circularized using a Fujinon 7-mm  $f/1.1$  lens and an anamorphic prism pair. After collimation the beam profiles were well approximated by circular Gaussians with  $1/e$  ( $E$  field amplitude) radii of  $2.65 \mu\text{m}$ . The LO profile was measured with a Beamscan scanning slit profilometer inserted in the beam path just after the input 50:50 combining beamsplitter, and the vertical and horizontal profiles are shown in Figure 30.

The signal beam was further conditioned, in order to approximate a plane wave, by expanding the output from the single mode waveguide through a 20x telescope and blocking all but the center of the beam with an iris, the nominal diameter of which was  $5.3 \mu\text{m}$ . The horizontal and vertical intensity profiles were measured as described above and are shown in Figure 31. Note that the constant amplitude curves one might expect in Figure 31 are not obtained because the beam profile is measured using a scanning slit, which actually integrates the beam along the direction perpendicular to the scan direction. For a constant amplitude, circularly truncated beam, the resultant output of the profilometer is proportional to  $(1 - x^2)^{1/2}$  when scanning in the  $x$  direction. In comparison, for a circular Gaussian beam the output of the profilometer is still a Gaussian profile.

The signal and LO wave fronts were also characterized using a LADITE wave front measuring instrument. Plots of the optical path differences (OPD) across each wave front are shown in Figure 32. The measured Strehl ratios were 0.90 and 0.84 for the LO and signal, respectively.

Using the method first described in [39] and later in [36] the spatial mode matching was measured to be 0.66. The theoretical spatial mode matching for a matched Gaussian ( $E$  field  $1/e$  radius  $w$ , and truncated at radius  $w$ ) and plane wave (radius  $a$ ) is 0.93, for  $a = w$ . Based on the analysis in [39,36], the mode matching for beams with small, uncorrelated aberrations may be approximated by the product of the ideal mode matching and the Strehl ratios of the signal and LO beams. Good agreement was obtained between the measured mode matching, 0.66, and the expected value based on the Strehl ratios,  $0.93 \cdot 0.84 \cdot 0.90 = 0.70$ .

### 11.2 CNR vs SIGNAL OPTICAL POWER

The thermal to LO shot noise ratio in the communications channel was characterized by measuring the ratio between the outputs of the communications channel photodetector/preamplifier front end with the signal beam blocked, and the LO alternately blocked and unblocked. Each communication photodetector received approximately 1.8 mW of LO power, which produced 0.9 mA of dc photocurrent. The sum of the shot noise plus thermal noise was 4.3 dB above the LO shot noise alone, within a 1 GHz noise bandwidth. Both the shot noise and total noise spectra were flat to within 0.5 dB over a 70 to 1300 MHz bandwidth.

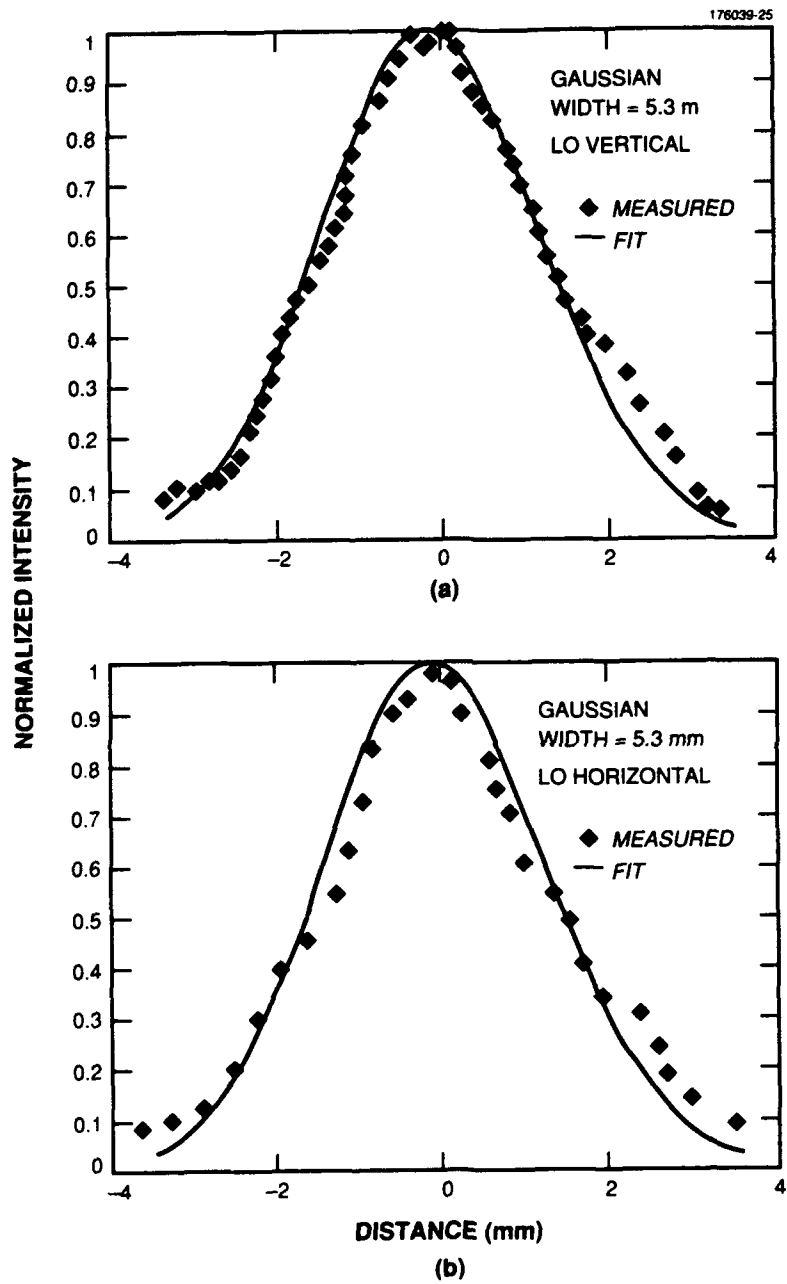


Figure 30. (a) LO beam profile, vertical. (b) LO beam profile, horizontal.

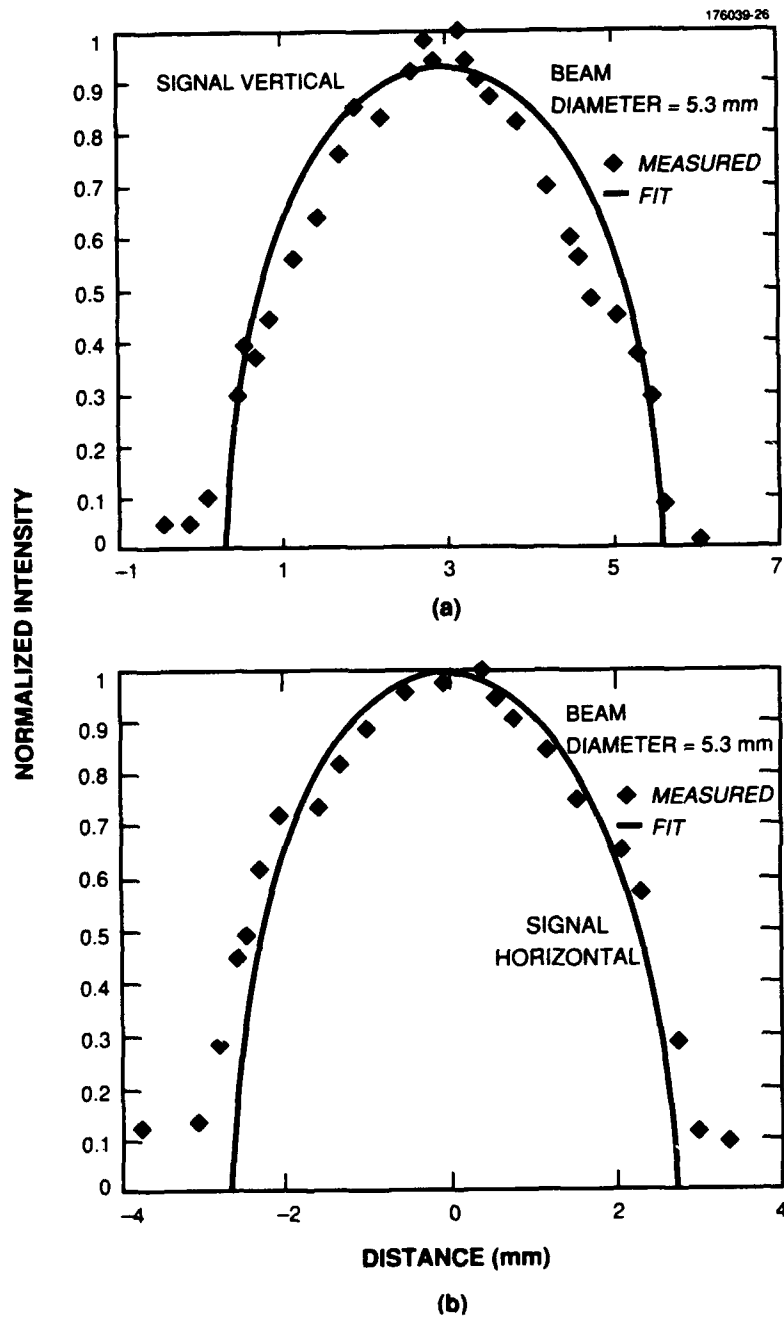


Figure 31. (a) Signal beam profile, vertical. (b) Signal beam profile, horizontal.

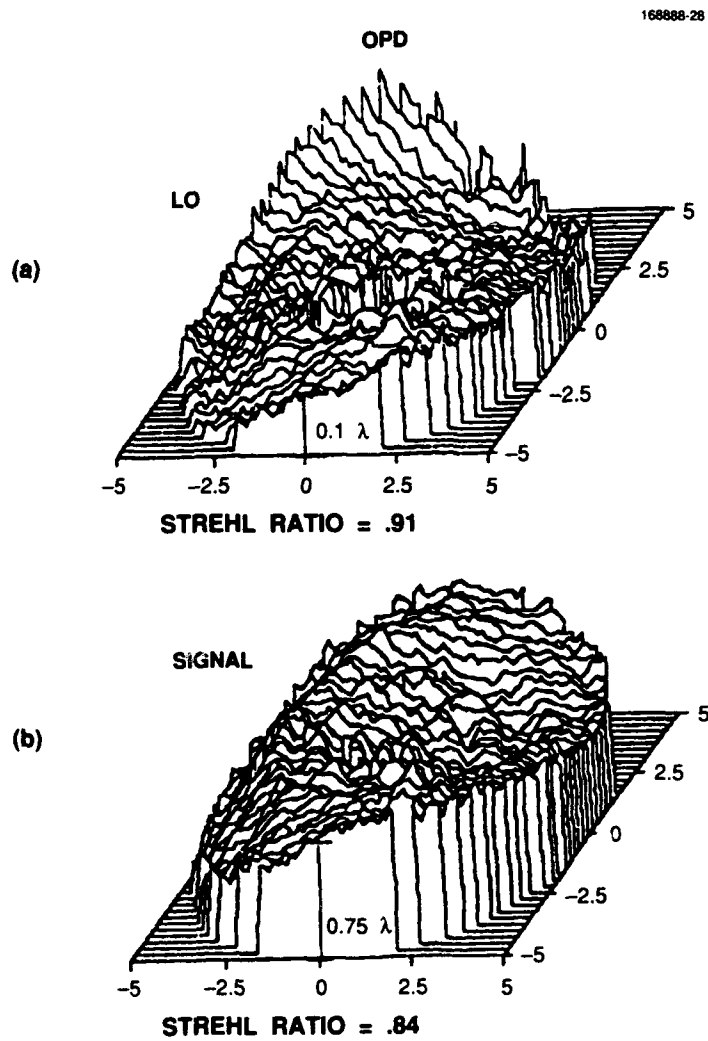


Figure 32. LO, signal beam wavefront optical phase distribution.

The LO intensity noise cancelling was measured by looking at the post-correlation IF signal of the spatial demodulator, with the signal optical beam blocked. The post-correlation signal consisted of the product of the LO shot plus excess intensity noise in the track and communications channel. If excess intensity noise is not present, one would expect the post-correlation signal to be zero mean. However, because the excess intensity was correlated on the three detectors, the dc output of the tracking demodulator, with the signal optical beam blocked, was a measure of the uncancelled relative excess intensity LO noise. The dc output of the spatial tracking demodulator was first nulled with the LO blocked in order to ensure that only correlated LO noise was being measured. The value of the intensity noise when one path length in the communications path was unbalanced could then be compared to the uncancelled intensity noise after the balanced receiver was nulled. The intensity noise could be reduced by at least 15 dB in this way [13]. The long-term stability of our experimental setup limited the practical cancellation to 15 dB. At this level, the corresponding LO intensity noise-induced offset was calculated to be less than 0.01 bw for signal photon arrival rates (at the communications detectors) greater than  $1.5 \times 10^8$  photons/s.

In addition, the ratio of rms shot noise to rms thermal noise in each of the track channels was measured. This was not identical to the communications channel because the input 50:50 combining beamsplitter was neither exactly a 50:50 splitter nor completely polarization-independent. Thus, equal LO power was not delivered to the communications, azimuth, and elevation channels. Also, the track channels each had two amplifiers per channel instead of only one as in the balanced communications channel. As a result, the azimuth channel operated with 0.75 mA/detector of LO photocurrent, while the elevation channel operated with 1.0-mA/detector of LO photocurrent. The measured ratios of shot noise power to shot plus thermal noise power were 0.31 (elevation) and 0.23 (azimuth).

The signal beam polarization was adjusted to give close to a 80:10:10 (comm:az:el) split; the actual measured signal distribution was 81:9:10.

The responsivity  $R$  of the detectors was measured to be 0.5 A/W, and assuming the low frequency and high frequency quantum efficiencies were the same, and the quantum efficiency was spatially homogeneous in each detector, a quantum efficiency is obtained of  $\eta = Rhv/e$ , or 0.72 at wavelength  $\lambda = 0.86 \mu\text{m}$ .

Finally the communications channel SNR was measured as a function of incident optical power. The results are plotted in Figure 33. For comparison the quantum shot noise limited SNR,  $\eta m^2 P_c / hv$  was plotted. The receiver loss was 7.7 dB from the quantum shot noise limit, of which 7.5 dB may be accounted for as follows: 1.8 dB for  $m^2 = 0.66$ , 1.4 dB for  $\eta = 0.72$ , and 4.3 dB due to excess thermal noise of the amplifiers within the 1 GHz noise bandwidth of the measurement system.

### 11.3 NEAR BORESIGHT DISCRIMINANT GAIN AND BIAS

The near boresight discriminant gain (volts/radian of tilt) in each axis was determined by deflecting the jitter mirrors by calibrated amounts and measuring the resultant tracking demodulator output. Figure 34 shows the elevation and azimuth channel small signal responses to 100  $\mu\text{rad}$  peak-to-peak triangle wave angular disturbances. The responses were quite linear over the +/- 50  $\mu\text{rad}$  range, and near boresight gains of 1.84 and 1.78 V/bw tilt were obtained for the elevation and azimuth channels, respectively. The variation of discriminant gain with input signal power was less than 5 percent over a 20 dB range of input signal optical power in the two channels.

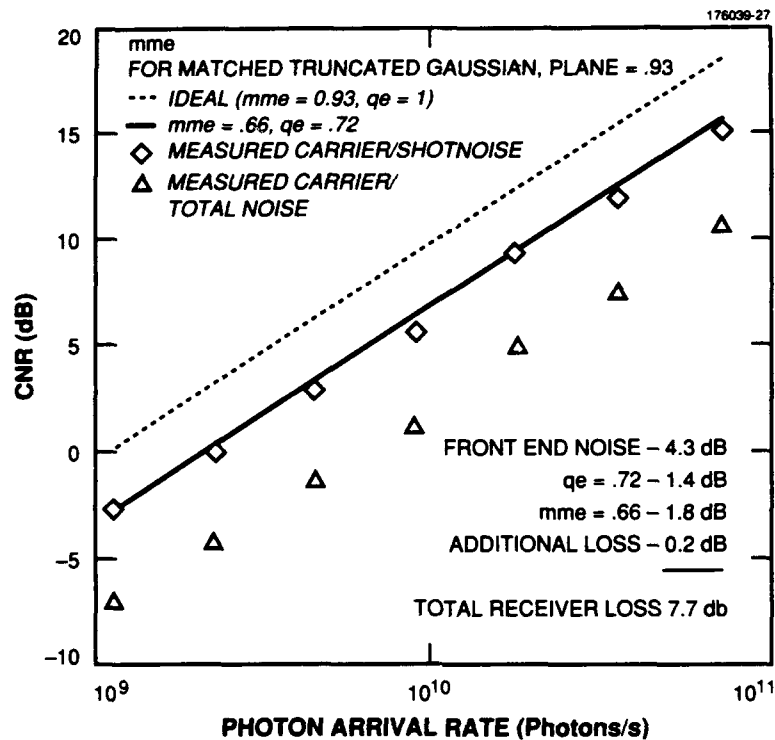


Figure 33. Communications channel carrier-to-noise ratio vs photon arrival rate.

In order to compare these results with theory, the gain,  $K_p = 1.38$  V/radian, of the tracking demodulator electronics was separately measured. Combining the measured transfer function of the tracking demodulator with  $K_D$ , the calculated electrical phase shift per beamwidth of optical tilt which was obtained via numerical integration of Equation (46), the predicted discriminant gain was  $K_p K_D = 1.71$  V/bw of tilt. The discrepancy between predicted and measured gains (1.84, 1.78 vs 1.71) is not due solely to beam diameter mismatch because the discriminant gain  $K_D$  is not particularly sensitive to such a mismatch. Calculations indicate that varying the ratio of beam diameters from 0.9 to 1.1 should produce less than  $\pm 3$  percent change from the gain for matched beam diameters. Also, the translational mismatch between the LO and signal beams was less than  $300 \mu\text{m}$ , which would not account for all of the observed gain difference. The discrepancy is attributed to inaccuracies in the calibration of the test aid used to find the gain of the demodulator electronics.

The tracking bias was measured by dithering the disturbance mirror at a frequency above the range in which the tracking loop had significant rejection (above 1 kHz). The resultant envelope modulation of the communication channel signal was then synchronously detected to determine the tracking bias offset. Over a -10 dB to +20 dB range of input optical signal power (relative to the budgeted level, see Table 1), and for IF heterodyne frequencies between 100 MHz and 1 GHz, the measured tracking bias was less than 0.015 bw.

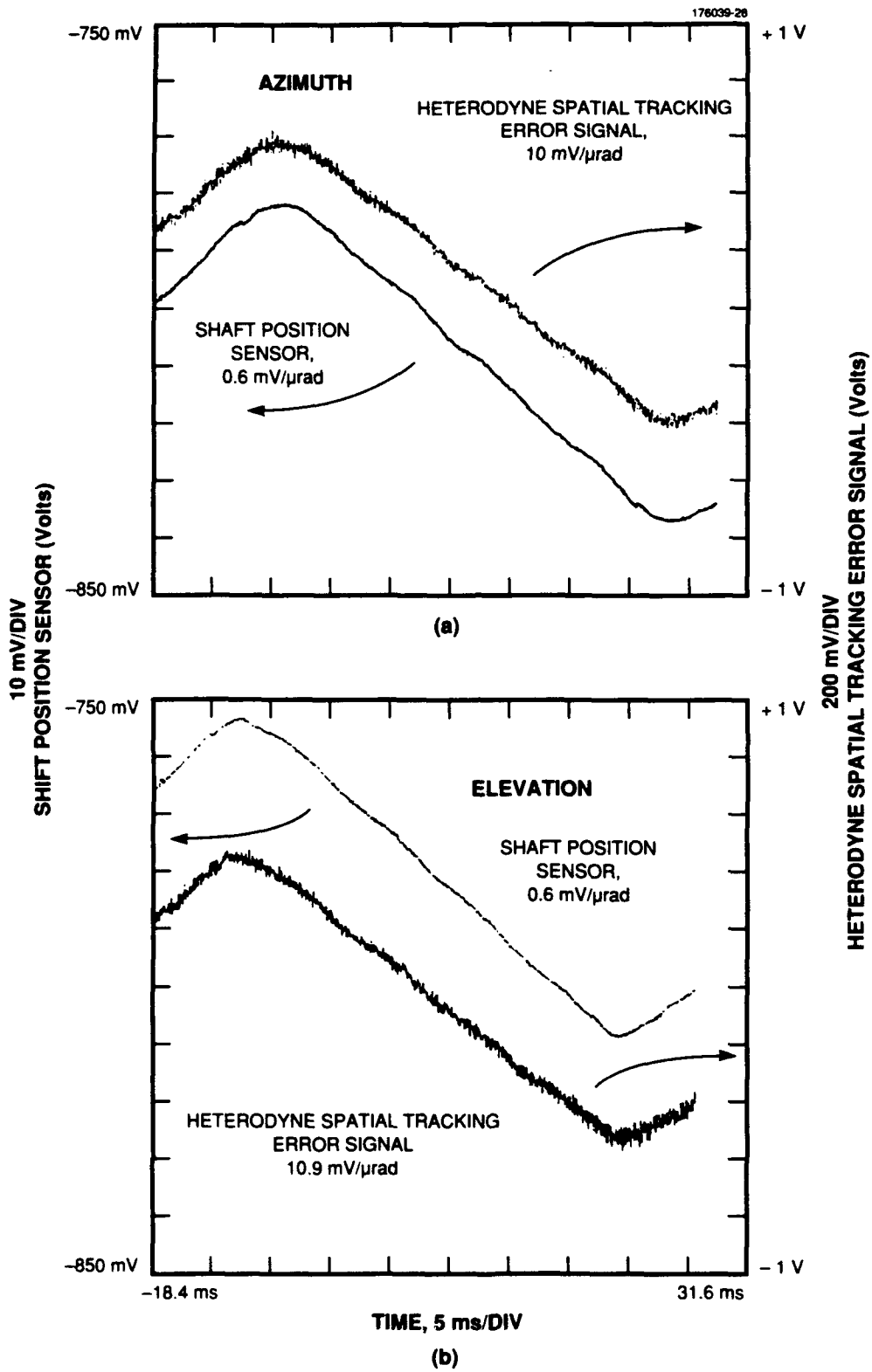


Figure 34. (a) Small signal azimuth tracking discriminant. (b) Small signal elevation tracking discriminant.

#### 11.4 OFF AXIS DISCRIMINANT SHAPE

The complete discriminants, at high and low SNR, are shown in Figure 35 for each track channel. The major features of the discriminant which can be compared with theory are the initial slope (Section 10.3), the first zero crossing, and the off-axis sign reversal for high SNR. Ideally, in a system with infinite AGC gain the off-axis shape of the discriminant normalized by the norm of Equation (9) would be given by curve c in Figure 28. Unfortunately, the AGC gain in any real system is finite, and hence the post-correlation signal has corresponding nulls and sign reversals with the communications (sum) channel. From Figure 28, in a system with matched Gaussian and plane wave optical beams the communications or sum channel magnitude, and hence the post-correlation discriminant, is expected to have a null at 1.2 bw. At high SNR, and for angular errors greater than 1.2 bw, the normalized discriminant actually reverses in sign, which can lead to positive feedback during closed loop operation (e.g., during acquisition). As discussed in Section 11.9.4, this affected the pull-in transients but did not otherwise affect normal operation of the tracking system. At low SNR the tails of the discriminant are dominated by the noise of the system.

#### 11.5 MEASURED NEA IN THE COMMUTATION CORRELATION PROCESSOR

The NEA of the spatial tracker may be obtained by measuring the rms noise equivalent voltage (NEV) at the output of the tracking demodulator within a 2-kHz noise bandwidth and then normalizing by the square root of the measured discriminant gain. These measurements were made with a frequency tracking loop enabled that controlled the LO laser current to maintain a constant IF tone at 325 MHz. The signal laser current was not modulated, i.e., no data were transmitted, during these measurements. In order to characterize the open loop angle sensor, the NEV measurements were made with the spatial tracking loop disabled. Because the relatively large low frequency disturbances in the open loop system, due to acoustic and mechanical noise on the optical table, would otherwise have dominated the measurements, the NEV was measured in a 2-kHz bandwidth from 1 to 3 kHz. The spectral density of the noise at the output of the tracking demodulator due to shot noise and amplifier thermal noise was flat to beyond 5 kHz, and above 1 kHz there were negligible mechanical and acoustic disturbances. The resultant NEAs are plotted in Figure 36. Error bars indicate the repeatability of the measurements. The major factors that accounted for the measured NEA variations at constant nominal input power were fluctuations in the signal optical power during the measurement interval (1 s) and inaccuracy in optical power measurements at received power levels of less than 50 nW.

For comparison Figure 36 plots the theoretical shot-noise-limited NEA for a commutated correlation processor (curve a), as well as the predicted NEAs for the laboratory system (curve b), which are based upon the measured, non-shot-noise-limited CNDs in the track and communication channels (Section 11.2) and the measured gain near boresight (Section 11.3). Within experimental repeatability the measured NEAs in Figure 36 agree with calculated values in curve c for our non-shot-noise-limited implementation.

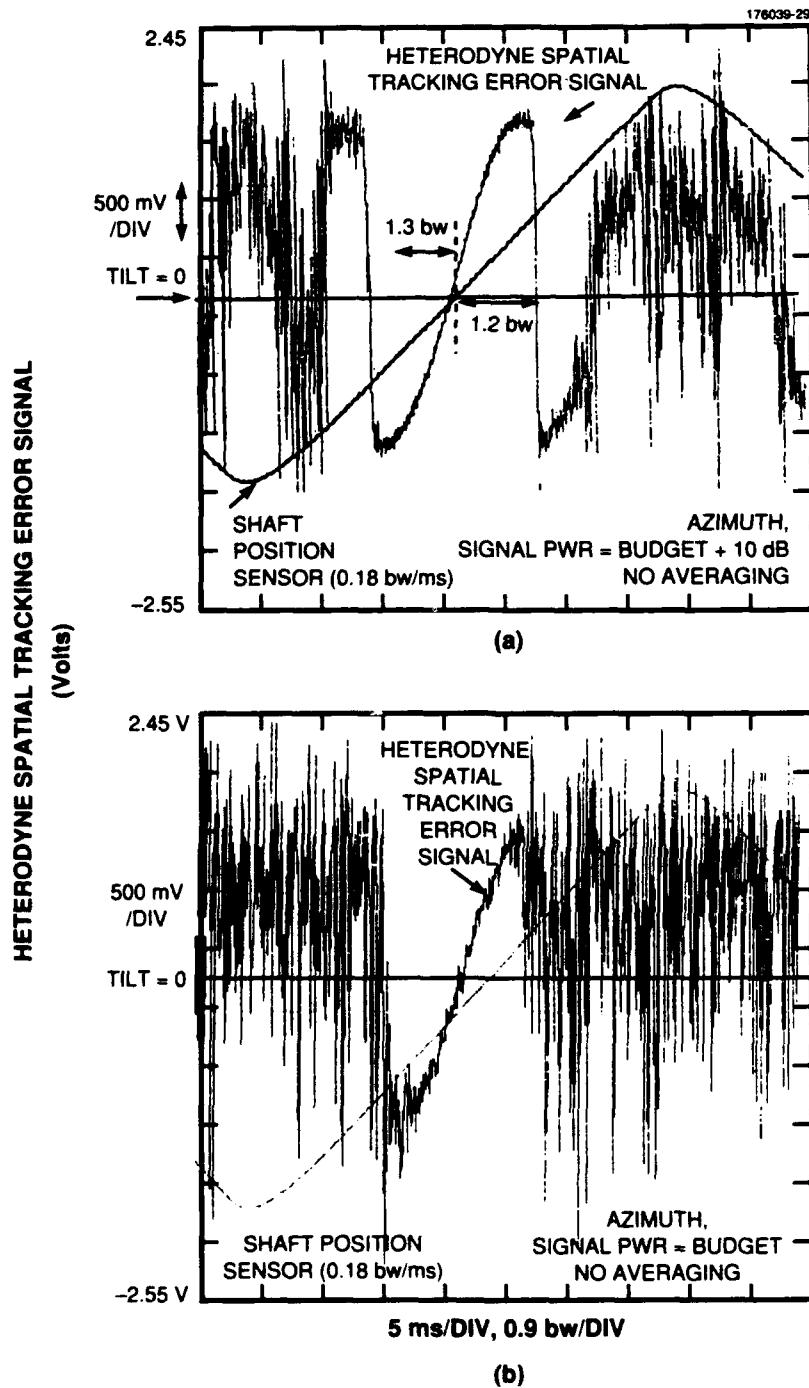
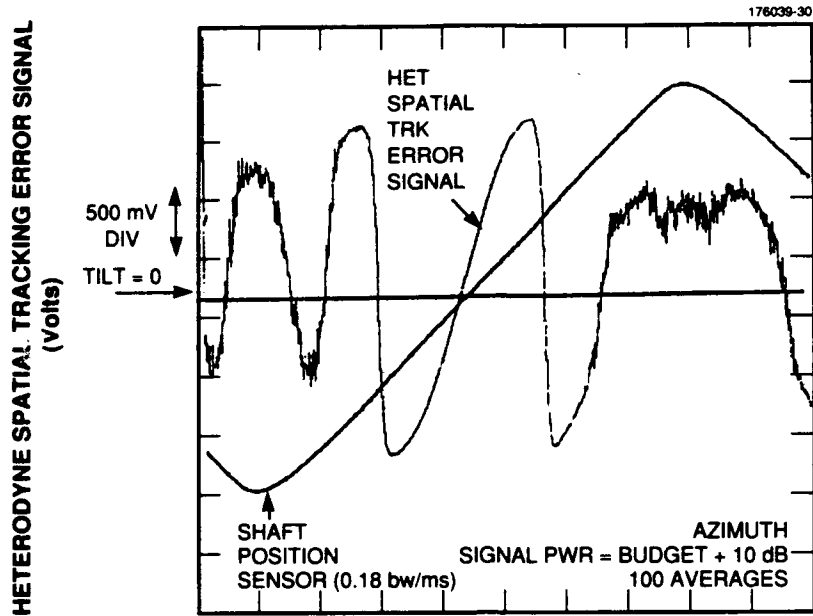
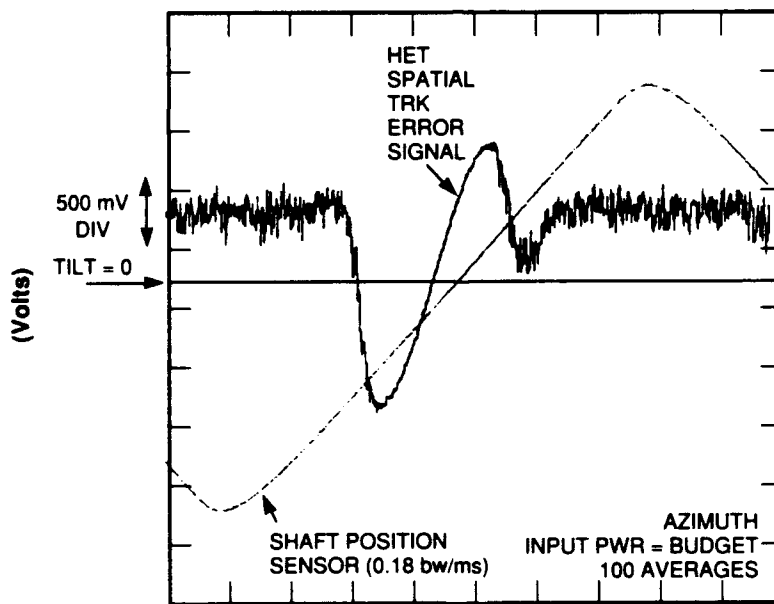


Figure 35. (a) Large signal tracking Az discriminant at high signal photon arrival rate. (b) Large signal tracking Az discriminant at budgeted signal photon arrival rate.



(c)



5 ms/DIV, 0.9 bw/DIV

(d)

Figure 35. (c) Large signal tracking Az discriminant with averaging, at high signal photon arrival rate. (d) Large signal Az tracking discriminant, at budget signal photon arrival rate with averaging.

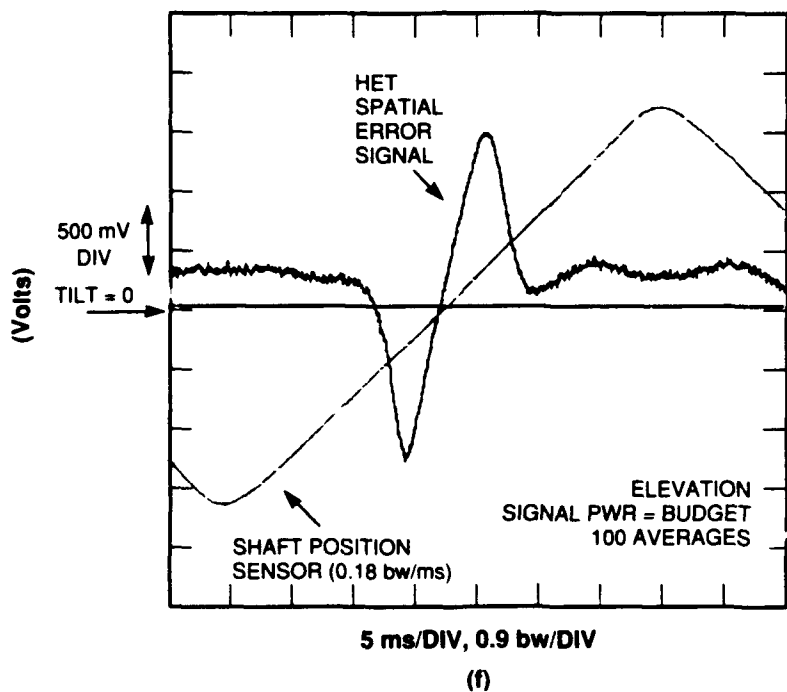
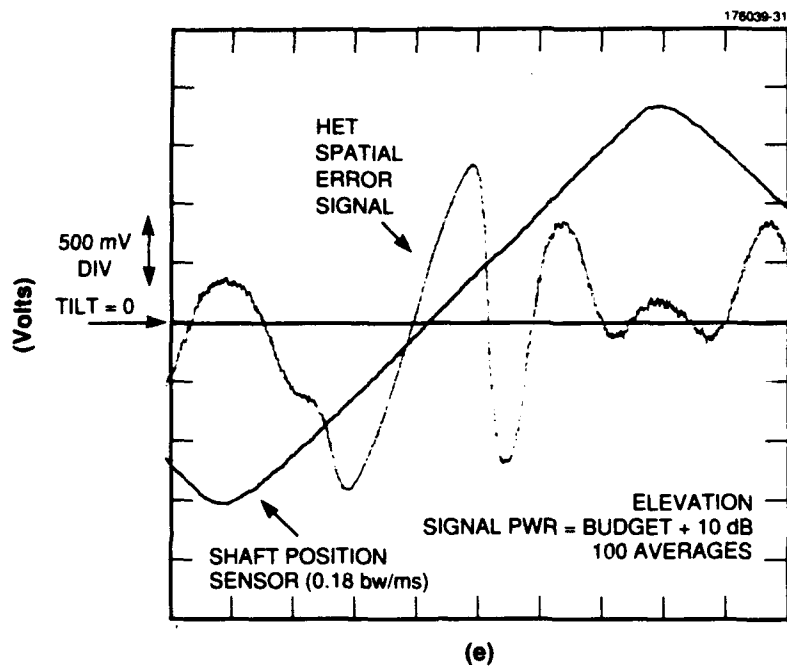


Figure 35. (e) Large signal elevation tracking discriminant, with averaging at high photon arrival rate. (f) Large signal elevation tracking discriminant with averaging at budget photon arrival rate.

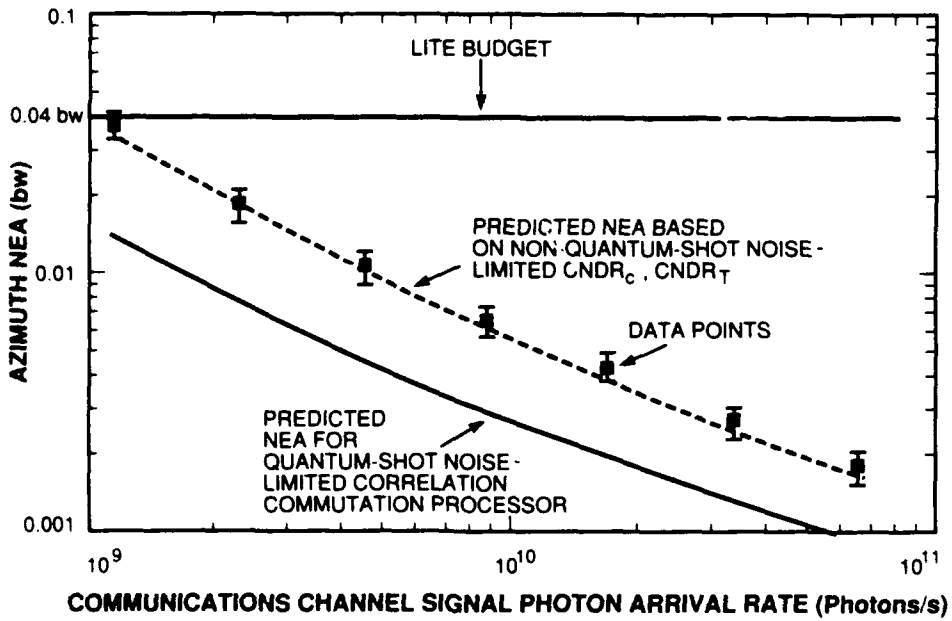
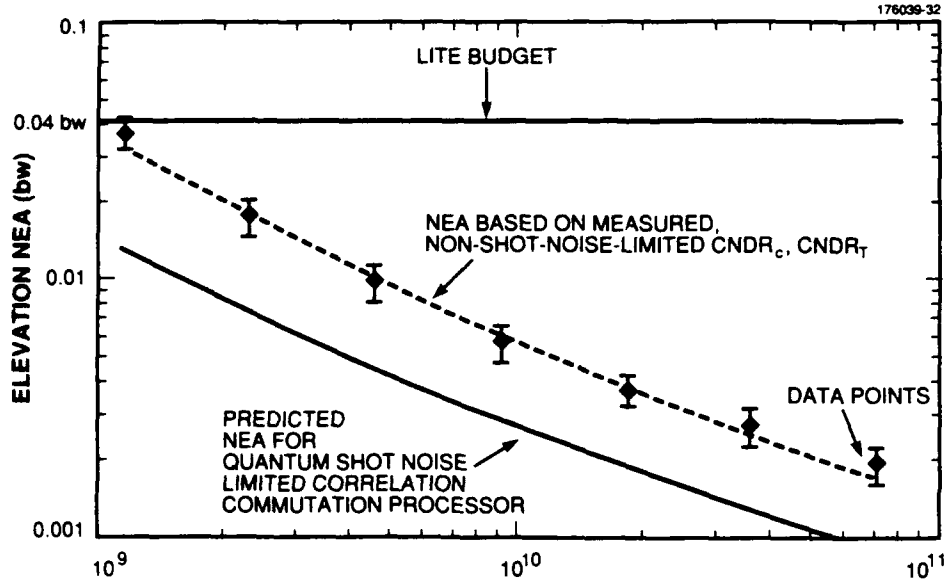


Figure 36. (a) NEA vs signal photon arrival rate, elevation. (b) NEA vs signal photon arrival rate, azimuth.

## 11.6 COMPARISON OF NEAS ACHIEVABLE WITH OTHER PROCESSING ARCHITECTURES

It is instructive to compare these results with NEAs of other processing architectures. First, the lower bound on a realizable NEA is achieved in a system with coherent RF demodulation, e.g., for FSK data modulation, a system in which the frequency of the received tone is known exactly. This yields the expression in Equation (57), which is plotted in curve a of Figure 37. It has been shown that square law processing (curve b, Figure 37) yields the same NEA at medium to high SNR but has a larger NEA at low SNRs where a noise times noise term dominates the square law NEA. Ideal correlation processing yields the same NEA as the square law processor, without the attendant problems of excessively stringent channel matching requirements to maintain acceptable noise-induced bias errors. Architectures have also been demonstrated [15] in which the communications and track channel signals, prior to correlation, are up-converted to frequencies that differ by a small frequency offset (e.g., 83 kHz), such that the post-correlation signal is offset from dc. This is attractive because the broadband multipliers used for correlation have large dc offsets. Also, by up-converting both communications and track signals the relative bandwidth of the RF multipliers is reduced. As long as both sidebands of the frequency-shifted signals are processed, the resultant NEA is identical to a simple correlation processor. An early implementation of the frequency-shifted correlation processor kept only one sideband of the upconverted signals (curve d, Figure 37), in order to reduce even further the relative bandwidth in the RF multipliers. It has been shown that the NEA in such an architecture is  $\sqrt{2}$  larger than the simple correlation processor.

The commutation correlation processor was derived from the frequency-shifted architecture. It is possible to build a frequency-shifted correlation processor in which only the communications channel is chopped using biphase modulation at a relatively low rate, e.g., 83 kHz. Compared to a simple correlation processor the resultant post-correlation signal is at this low IF frequency, rather than dc, and because both sidebands of the frequency-shifted communications signal are kept, there is no performance penalty relative to simple correlation [15]. It is now possible to obtain RF multipliers that are sufficiently flat within a 100 to 1000 MHz frequency range to make this approach practical. However, in all of the correlation architectures discussed so far, the track channels must be closely matched from the photodetector/preamplifiers to the RF multiplier in order to maintain a discriminant gain that is independent of the tone frequency and in order to minimize bias errors. The commutation correlation processor simply moves the chopping function from the communications path to the track channel path. As a result, only the paths between the track photodetector/amplifier and the RF commutator must be tightly matched to minimize bias errors, which is a substantially simpler task. It is still necessary to maintain the phase match between the overall track and communications channel to within 5 to 10° [32,40], to achieve the desired discriminant gain.

As was derived in Section 10.4, the commutation in the track paths introduces a  $\pi/2$  increase in NEA (curve e, Figure 37) relative to simple correlation. This can be viewed as a consequence of chopping the noise in each track channel far below the Nyquist rate, such that out-of-band noise is folded into the post-correlation bandwidth. It can be shown that if one chops at a rate above the Nyquist rate the NEA of the commutation processor is the same as simple correlation. This would be impractical in most

applications. It is also possible to show that by building a second identical correlation channel, in which the commutation is inverted from the first, and adding the post-correlation signals together, a factor of  $\sqrt{2}$  may be regained. The NEA in the two channel commutation architecture (curve c, Figure 37) is then only a factor of  $\pi/2\sqrt{2}$  or 1.11 larger than the NEA in simple correlation processing.

The heuristic argument for this increase is that the post-correlation noise in each channel of the two channel architecture is uncorrelated; the right and left channel noises are uncorrelated to the extent that they are composed only of thermal and shot noise, and the noise is sufficiently white that samples from a single noise channel taken one commutation period apart are also uncorrelated. The post-correlation signals then add coherently, while the noise adds incoherently, resulting in a factor of 2 improvement in SNR, or  $\sqrt{2}$  in NEA. Finally, it is important to note that the two-channel architecture would offer no advantage over the single channel version when the commutation rate is above the Nyquist rate. This is a consequence of the fact that when sampling at these rates, noise samples are not uncorrelated from one commutation period to the next.

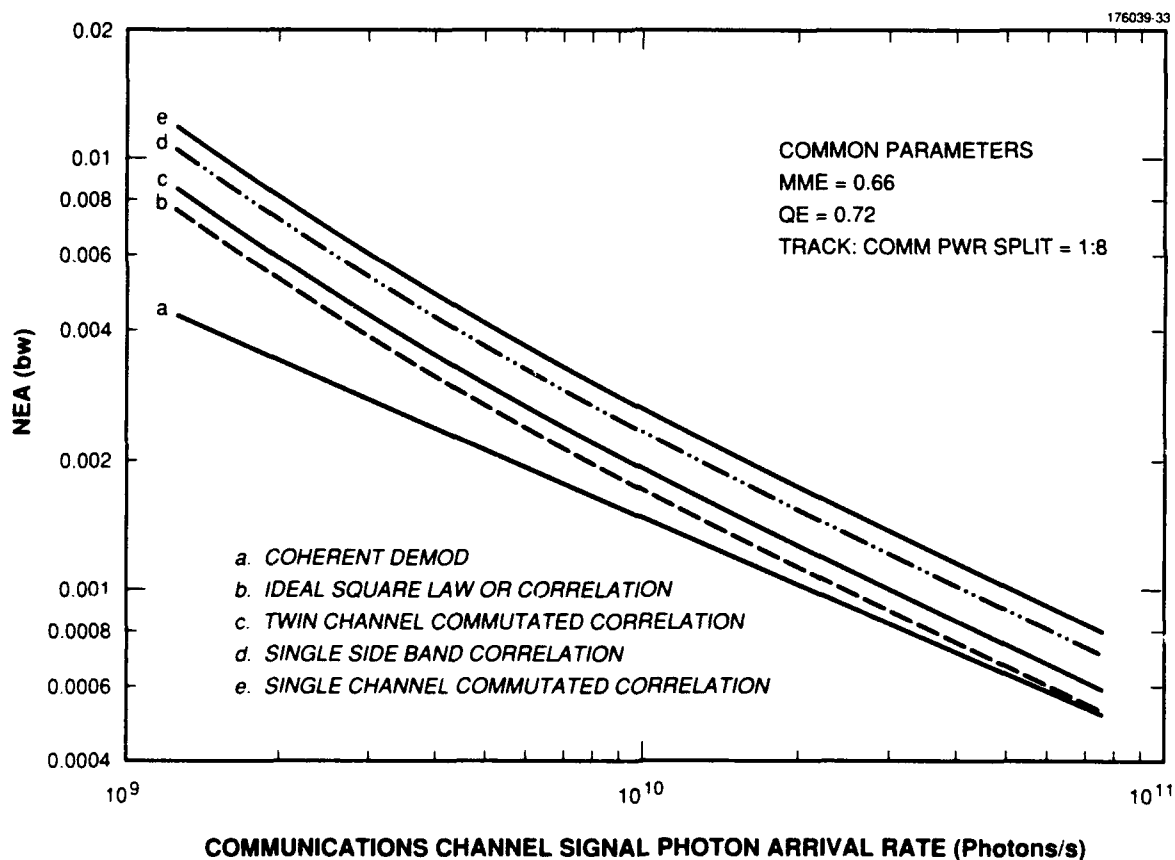
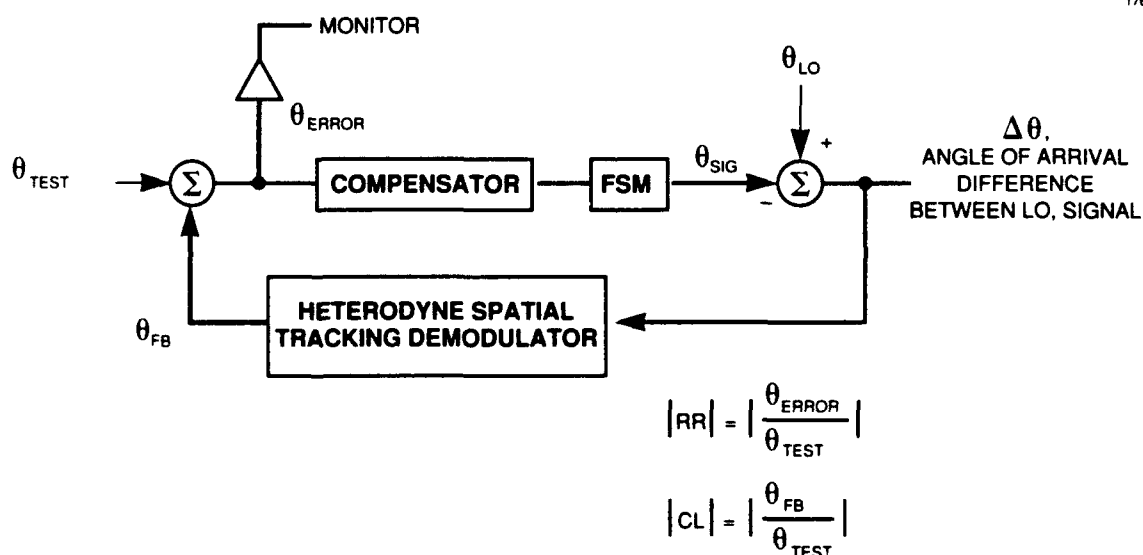


Figure 37. Comparison of NEAs for various processing architectures.

## 11.7 CLOSED LOOP TRACKING AND DISTURBANCE REJECTION

Closed loop disturbance rejection was provided by driving the FSM with an appropriately filtered version of the tracking demodulator output. The system gain was increased to yield the fastest response possible without excessive ringing due to feedback from the FSM second resonance. The resultant azimuth and elevation loop gain crossover frequencies were estimated to be 800 and 700 Hz, respectively. Each compensation filter included two integrators (for low frequency rejection), a lead-lag network centered at the loop gain crossover frequency for adequate phase margin, an additional zero below crossover, also to improve the phase margin, and a second-order pole pair well above crossover to reduce the effects of feedback from higher-order resonances in the FSM. A second-order notch filter was also included at the second resonance of the FSM (11.4 kHz).

The closed loop transfer function and rejection ratio were each measured using the setup in Figure 38. An electrical test signal (denoted  $\theta_{\text{test}}$ ) was applied to the input of the tracking loop. The closed loop transfer function is the ratio of the output to the input, while the rejection ratio is the ratio of the error voltage (input minus feedback) to the input signal. The closed loop transfer functions are shown in Figure 39, where it can be seen that the measured 3-dB frequencies of the closed loop responses were 2.3 and 2.5 kHz in the elevation and azimuth channels, respectively. The rejection ratios for the elevation and azimuth channels are shown in Figure 40, where it can be seen that more than 15 dB of rejection was obtained in each channel at 200 Hz, and more than 28 dB at 100 Hz. The measurements plotted in Figure 40 were made with 10 times the nominal signal photon arrival rate, in order to reduce the averaging necessary to yield a clear picture. With sufficient averaging, the same results were obtained over the 30-dB range where the signal normalization maintained a constant discriminant gain.



NOTE:  $\theta_{\text{TEST}} = 0$  FOR NORMAL OPERATION OF THE HETERODYNE SPATIAL TRACKER

Figure 38. Set-up to measure closed loop transfer function and rejection ratio.

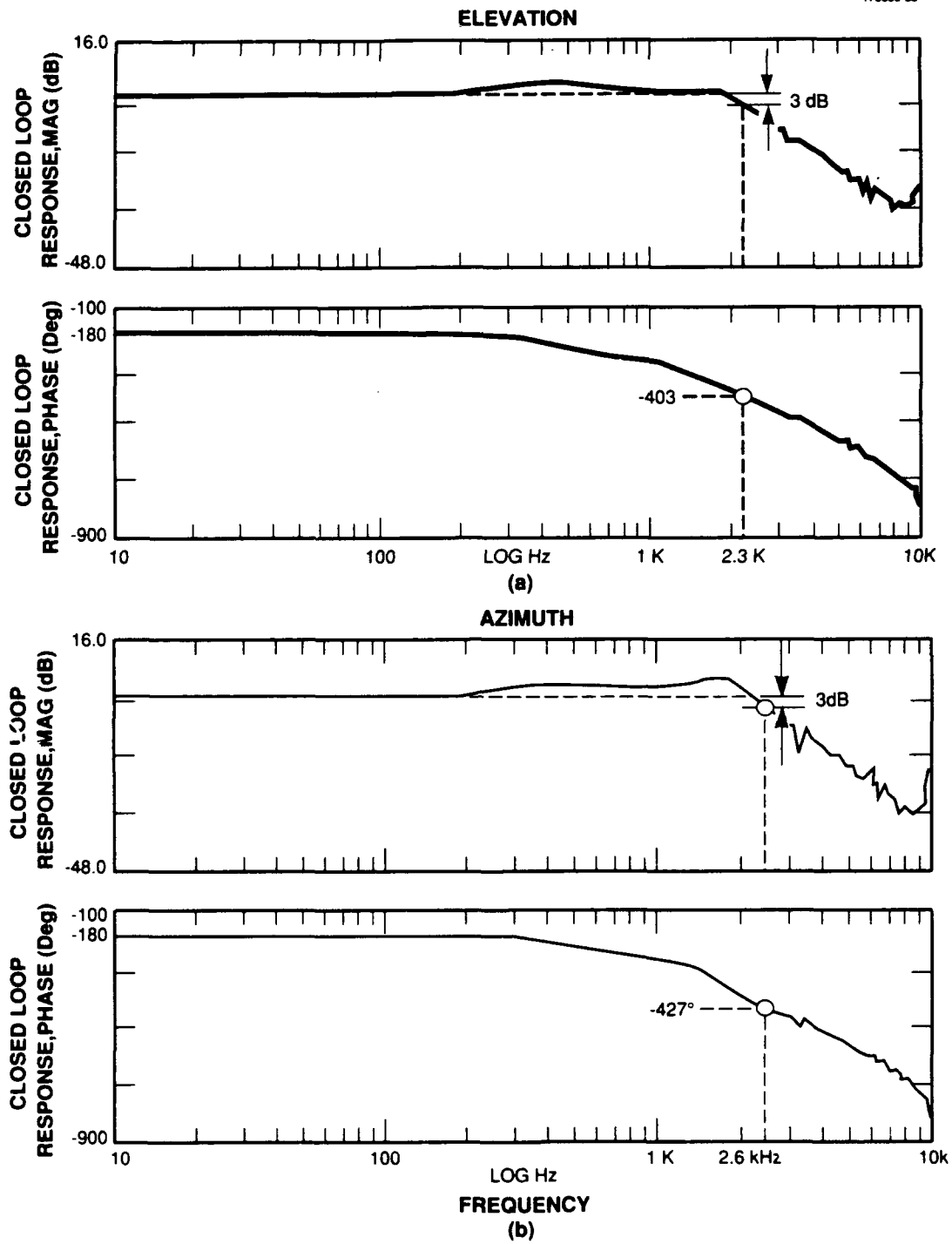
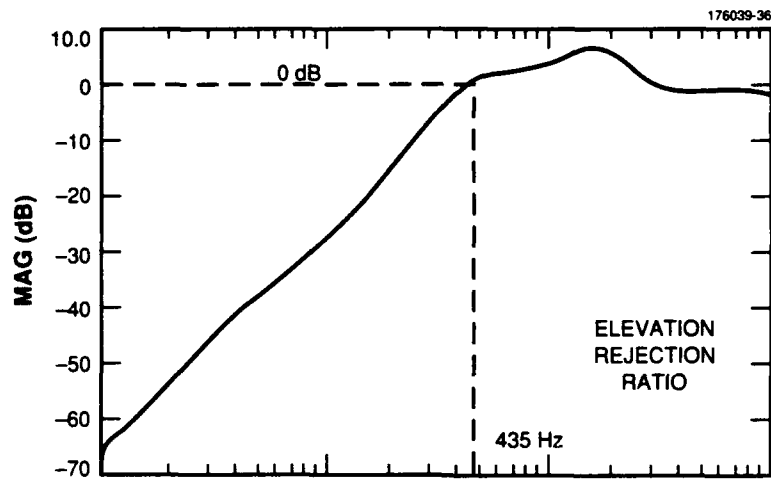
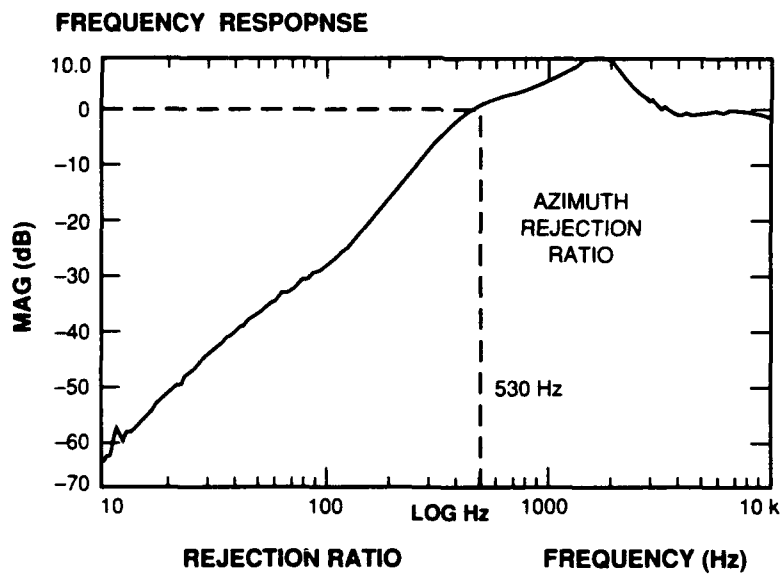


Figure 39. (a) Closed loop input/output transfer function, elevation. (b) Closed loop input/output transfer function, azimuth.



(a)



(b)

Figure 40. (a) Rejection ratio, elevation. (b) Rejection ratio, azimuth.

The performance of the spatial tracking loop in the microjitter environment that was described in Section 2.3.1 may be predicted by applying the measured rejection ratio to the power spectral density (PSD) of the angular jitter in Figure 2. In Figure 41 the integrated PSD of the expected angular jitter on the ACTS satellite, both with the tracker on (curve 3) and with the tracker off (curve 1), is compared to the allowable single axis rms angular error (0.05 bw/axis). Curve 3 in Figure 41 was obtained by multiplying the measured spatial tracker rejection ratio by the expected ACTS jitter spectrum and integrating the resultant spectrum. It can be seen that the demonstration spatial tracking system rejection was sufficient to meet the LITE system specification of 0.05 bw residual angular error.

The integral of the disturbance spectrum that was used to simulate on-orbit jitter, both with rejection (curve 4) and without rejection (curve 2), is also plotted. This spectrum corresponded to white noise filtered with a single pole at 35 Hz. Curve 4 of Figure 41 demonstrates that in the demonstration system with the spatial tracker on, and 2.1 bw rms disturbance jitter added to the incoming signal beam, the residual angular jitter was 0.07 bw.

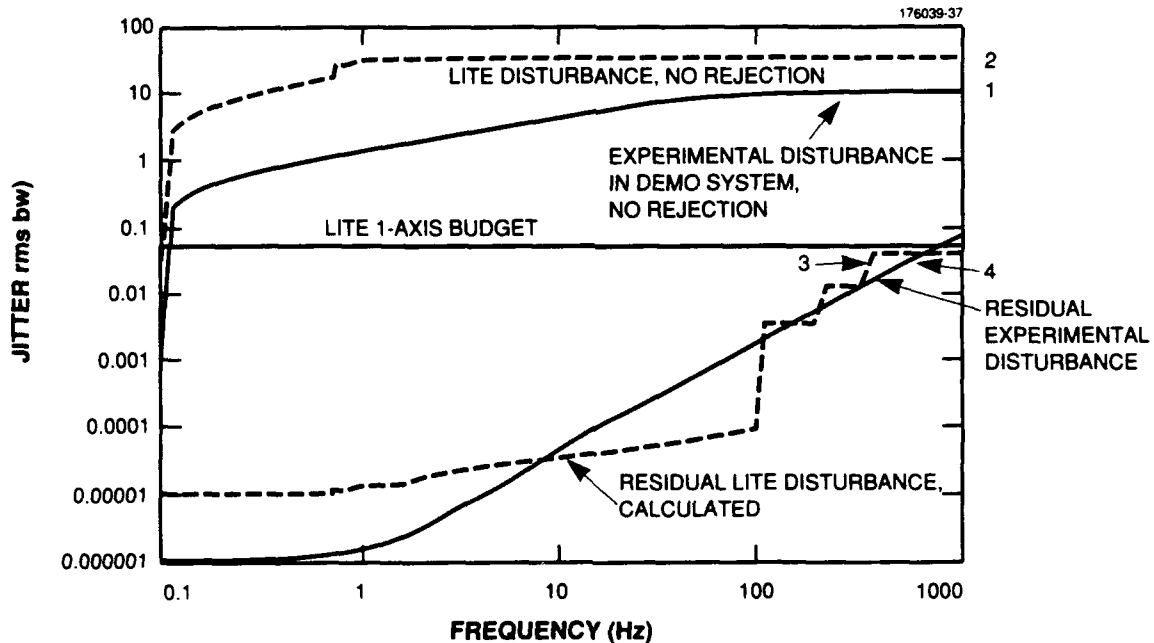


Figure 41. Residual jitter for open loop, closed loop systems.

## 11.8 BER VS OPTICAL POWER, JITTER

BER curves were measured as a function of jitter level and input signal optical power using a pseudo-random sequence of length  $2^{15} - 1$ . The communications link described in Section 9.6 was operated with a signal-LO laser pair whose modulated IF spectrum is shown in Figure 42. The linewidth of each tone was 22 MHz, which accounted for the observed BER floor near  $10^{-4}$ . The BER measurements are summarized in Figure 43. Curve a was taken with frequency tracking enabled, but without any active spatial tracking. The rms disturbance level during this test was less than 0.1 bw (over a 1 to 1000 Hz bandwidth). Curves b, c, and d are taken with the spatial tracking enabled and with an rms (1 to 1000 Hz bandwidth) jitter level of 0.4, 1, and 2.1 bw/axis, respectively. The spectrum of the applied jitter disturbance was shown in Figures 2 and 41.

The BER floor imposed by the large IF linewidth reduced the sensitivity of the communication system to angular mismatches between the signal and LO beams. However, by comparing the BER with spatial tracking enabled and disabled, when there was much less than 0.1 bw disturbance jitter present, it can be seen that the spatial tracking system by itself did not degrade communications performance in any measurable way. As the angular jitter amplitude was increased to the maximum value of 2.1 rms bw (in which case the residual jitter was 0.07 bw, see Section 11.7), the observed BER performance remained constant when the spatial tracking loop was enabled. Finally, note that without active spatial tracking the communications link was completely inoperative for residual rms jitter levels greater than 0.5 bw.

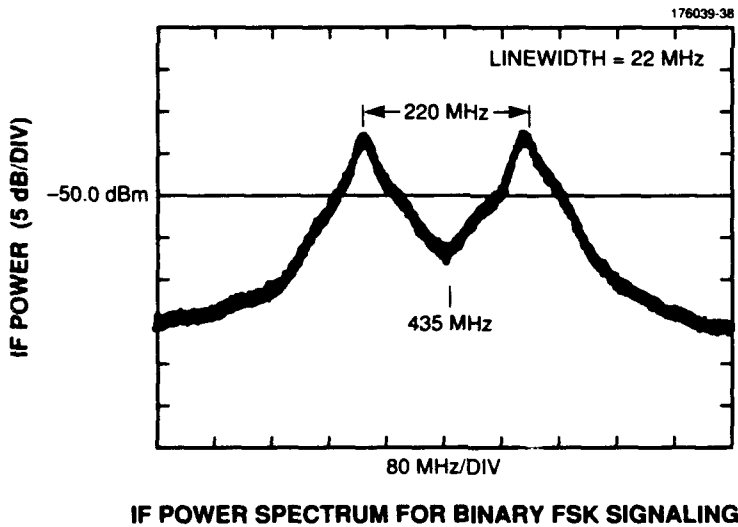


Figure 42. IF spectrum for binary FSK signaling.

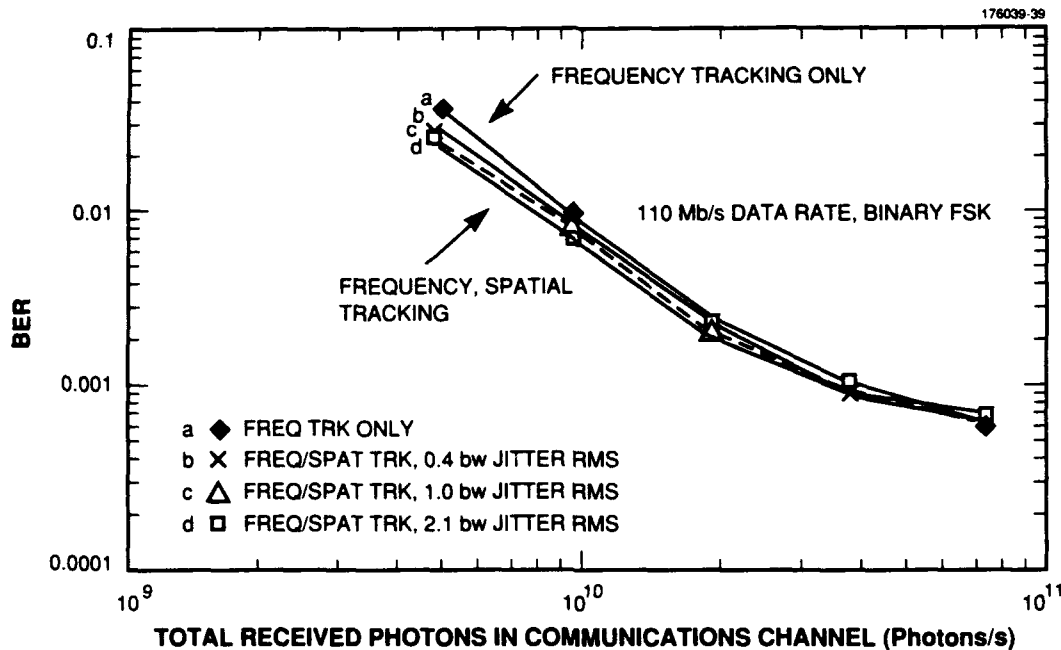


Figure 43. BER vs communications channel signal photon arrival rate.

## 11.9 HANDOFF CHARACTERIZATION

This section describes the algorithm by which handoff from CCD-based acquisition to heterodyne spatial tracking was achieved and presents data to illustrate system performance over a range of input optical powers and rms disturbance jitter levels. The handoff trajectories were measured by simultaneously recording the azimuth and elevation track mirror position sensor outputs and plotting them against one another to obtain the azimuth-elevation trajectories. In each case the beam was scanned outward from the center of the patterns.

### 11.9.1 Handoff Algorithm

The procedure by which the transition from acquisition to tracking was achieved is described. Following acquisition, and after beam narrowing of the received signal has been detected through the resultant power surge, a spiral scan is initiated centered on the acquisition location. The tracking loop is set to the handoff mode. As discussed in Section 9.5 (see Figure 25), in the handoff mode the tracking loop is modified such that a maximum of  $\pm 1$  to 2 bw of deviation from the scan pattern can be commanded by the loop. In addition, one of the integrators in the loop compensation filter is disabled while in handoff mode. This is equivalent to setting an initial condition in the compensator of zero velocity. It is important to note that because the output of the velocity integrator is additionally filtered by the second (position) integrator, the output of the compensation filter will be continuous when the transition from handoff to tracking mode occurs. The transition to the full authority tracking loop (i.e., enabling the velocity integrator and removing the limits on the compensation filter output) is made when the received power exceeds a predetermined threshold.

In the demonstration system this threshold was experimentally set to trip at the minimum received power level for which the spatial tracker was expected to operate. The decision logic included a small amount of hysteresis (equivalent to  $\sim 0.2$  bw of beam movement at minimum signal power) to avoid dithering when the received signal power was close to the threshold. The following discussion refers to the limited authority, single integrator tracker as the handoff mode spatial tracker. The two-integrator, full-authority tracker will be referred to simply as the spatial tracker.

### **11.9.2 Handoff Spiral Scan Pattern**

The beam angular position during the spiral scan with the spatial tracking disabled is shown in Figure 44(a). The angular position was measured using the shaft position sensors on the azimuth and elevation FSMs. The individual azimuth and elevation shaft positions are also plotted as a function of time [Figure 44(b)]. Previous calibration (see Appendix A) demonstrated that the actual signal beam angle of arrival corresponded to the FSM shaft position sensor output with a maximum error of less than 0.1 bw over the full angular range of the FSMs. In this idealized mode of operation the deviation of the actual spiral scan from the commanded pattern was less than 0.1 bw. The slight ellipticity of the pattern is due to a small gain difference between the elevation and azimuth axes of the spiral scan generator. In Figure 44(c) the same scan is illustrated with the limited authority feedback loop enabled, but when the signal was not within the receiver FOV. Thus the feedback loop was driven by noise, and approximately 0.2 to 0.3 bw of deviation from the ideal pattern was introduced.

Two possible scan patterns were available: a slow scan in which the tangential angular velocity was 0.5 bw/ms with the ring to ring distance of 0.6 bw, and a fast scan in which the tangential angular velocity was 1.0 bw/ms with the ring to ring distance of 1.1 bw.

### **11.9.3 Pull-in of the Spatial Tracker, in Handoff Mode**

To illustrate the tracker pull-in during handoff, Figure 45(a) plots the tracking FSM position (equivalent to the signal beam angular trajectory) when the tracking loop was kept in the handoff mode (the transition to full authority track mode was disabled). The initial signal location was about 4 bw away from the center of the receiver FOV, and the fast spiral scan was employed. Two different interpretations of the tracking FSM position are necessary, depending upon whether active spatial tracking has commenced. Prior to active spatial tracking (i.e., prior to and during the spiral scan), motions of the tracking FSM correspond directly with signal beam angular motions. Note that the complete signal beam trajectory cannot be reconstructed from the tracking FSM motion prior to active spatial tracking because the disturbance FSM motions and acoustic and mechanical disturbances are not detected by the tracking FSM position sensor. After the start of active spatial tracking [Figure 44(c), at the apparent end of the spiral scan] the tracking FSM motion represented the inverse motion necessary to cancel disturbances either from mechanical or acoustic vibrations, or as introduced via the disturbance FSM. During active spatial tracking, for disturbances in the frequency regime where the spatial tracking loop had reasonable rejection, the signal beam itself was essentially motionless. Therefore, the motion of the tracking FSM during active spatial tracking was a measure of the disturbances that were present (and those present but not shown prior to spatial tracking).

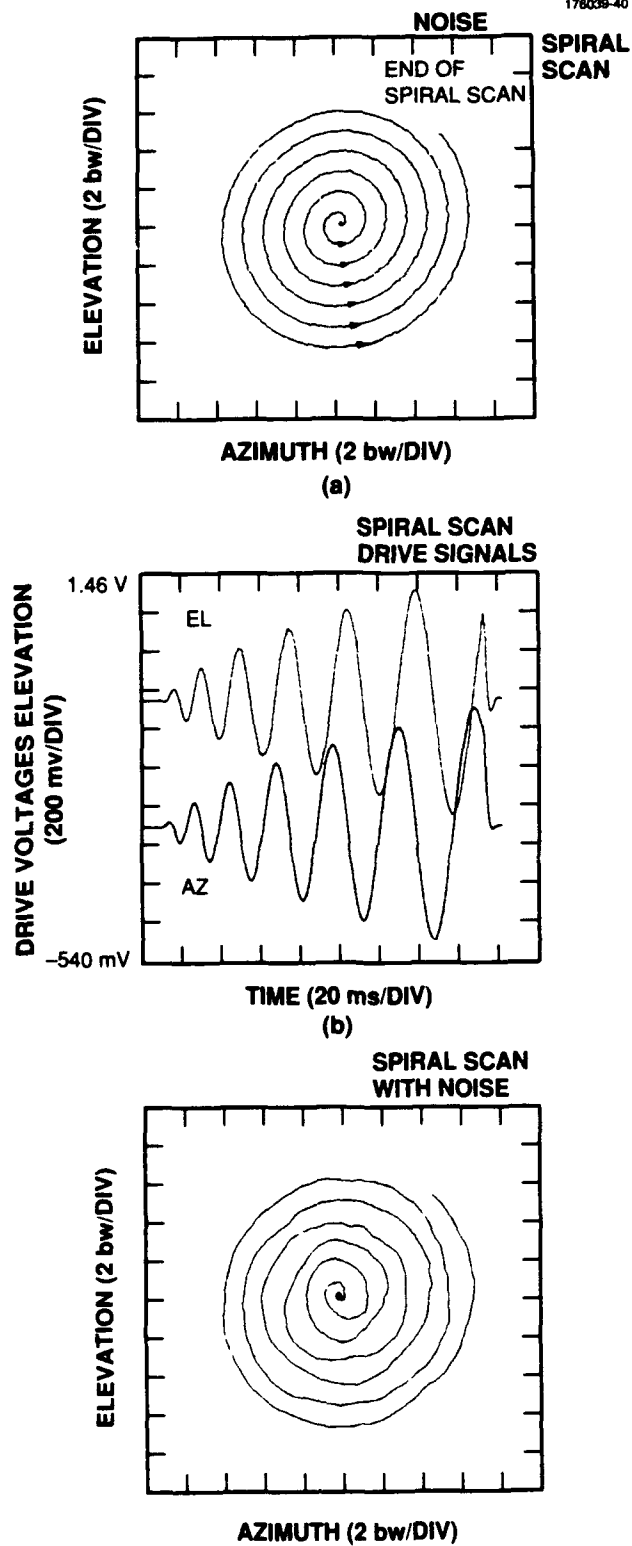


Figure 44. (a) Spiral scan, no noise. (b) Az, EL drive signal for spiral scan. (c) Spiral scan with noise.

In the example illustrated in Figure 45(a) the signal photon arrival rate (in the communications path) was  $1.3 \times 10^{10}$  photons/s, which was the budgeted level during spatial tracking. At this photon arrival rate the tracker discriminant was useful (i.e., not dominated by noise) within 1 bw of the center of the receiver FOV. On two consecutive passes, as the signal was swept by the receiver FOV the loop acted to center the beam (counteracted the spiral scan) until the authority limits were exceeded. An expanded view of this trajectory is shown in Figure 45(b), along with an overlay of the trajectory that resulted when the transition to full authority tracking was enabled. In the overlay the tracker pulled in on the first pass, and when the full authority tracking was enabled the spiral scan was counteracted continuously. As previously noted, the post-pull-in movement of the tracking FSM, illustrated by the enlarged spot at the center of the tracker FOV, was a measure of the acoustic and mechanical disturbances present on the optical table. Measurements of the heterodyne tracker error signal indicated that the signal beam itself was motionless to a resolution equal to the NEA of the tracker.

#### **11.9.4 Effects of Varying Handoff Mode Authority Limit on Pull-in Trajectories**

The transition from handoff mode to full authority spatial tracking is enabled when the communication channel IF power exceeds a preset threshold. A given threshold level corresponds to placing the signal beam a particular angular distance  $\Delta\rho$  away from the receiver FOV boresight. At larger signal photon arrival rates,  $\Delta\rho$  is greater because with a stronger signal on boresight a larger angular deviation is required to reduce the signal to the fixed threshold level. In handoff mode the spatial tracker can force an angular deviation from the spiral scan of at most  $\Delta\alpha$ , where  $\Delta\alpha$  is the tracker authority limit. A necessary condition for successful handoff is that the spiral scan sweep the signal beam to within  $\Delta\alpha + \Delta\rho$  of the receiver FOV boresight. These considerations make it attractive to make  $\Delta\alpha$  as large as possible in order to increase the pull-in range of the spatial tracker.

Unfortunately, because the spatial tracker output is dominated by noise when the signal beam is not within the receiver FOV, setting the authority limit too high may excessively distort the spiral scan pattern. In the system under discussion, the noise-induced distortion was less than 0.5 bw and was not the dominant factor in setting the handoff mode authority limit.

The dominant factor in determining an appropriate authority limit was the sign reversal in the off-boresight discriminant at high SNR. This sign reversal resulted in positive feedback, which tended to force the signal beam away from the receiver FOV. This is particularly a problem because the signal beam must traverse the region of positive feedback in order to reach the receiver FOV boresight. Figure 46(a) illustrates an artificial case in which the signal was deflected around the receiver FOV on two consecutive passes, and for which handoff was unsuccessful. In this example the on-axis received signal power was 4.7 dB above budget, and the authority limit was set to  $\pm 5$  bw. This combination of authority limit and received signal power was chosen to illustrate this problem, and was not representative of normal handoff. At the budgeted signal power level where the tails of the discriminant were noisier, and hence the positive feedback region was smaller, the effect was less pronounced, as illustrated in Figure 46(b). Note that the effect of the positive feedback can still be seen in the distortion of the spiral scan in the vicinity of the signal beam location, prior to pull-in.

It was possible to improve the pull-in performance by reducing the authority limit. Since the discriminant is of little use when it either changes sign or is dominated by noise, the pull-in range for a correlation-based tracker cannot be greater than about 1.2 bw (the point at which the communications channel magnitude has its first null). When the authority limit was set to a maximum excursion of 1.5 bw ( $\pm 0.75$  bw) and the signal photon arrival rate was much higher than nominal, the trajectory in Figure 47(a) was obtained. Reduction of the authority limit to  $\pm 0.5$  bw, shown in Figure 47(b), resulted in somewhat less distortion of the scan pattern outside the pull-in range, but no real change in the actual pull-in transient. In each case the spatial tracker pulled in on the seventh cycle of the spiral scan. These examples demonstrate that the problem illustrated in Figure 48(a) can be reliably eliminated, even when the discriminant has regions of positive feedback, by selecting an adequately small authority limit during handoff. Furthermore, an adequately small authority limit does not reduce the pull-in range below that defined by the angular misalignment at which the discriminant is dominated by noise.

### 11.9.5 Effects of Angular Jitter on Pull-in Trajectories

Using the slow spiral scan described in Section 11.9.2 with the authority limits on the handoff mode set to  $\pm 0.75$  bw, pull-in trajectories were recorded for signal photon arrival rates of  $1.3 \times 10^{10}$  and  $13 \times 10^{10}$  photons/s (budget and 10 dB above budget), and for rms angular jitter levels of 0.4 and 2.1 bw/axis. The disturbance FSM (see Figure 4) in each channel was driven with independent Gaussian noise power spectral density flat to 35 Hz and then rolled off in single-pole fashion. Sample trajectories are shown in Figures 48 and 49.

The rms jitter amplitude did not noticeably affect the spiral scan trajectories, even when the peak jitter excursions were several beamwidths in extent. The jitter had no observable effect on the trajectory during the actual handoff from spiral scan to active spatial tracking, i.e., the transition during which the signal moved from the edge to the center of the receiver FOV. The transition was always observed to be direct and free of significant overshoot or ringing. This was confirmed by looking at the heterodyne spatial tracking error signal during the transition.

The jitter did affect exactly when pull-in occurred. Over several repetitions in which the signal had the same initial angular offset from the receiver FOV, the actual point along the spiral scan when the signal came within the receiver FOV was observed to vary by approximately the rms amplitude of the jitter. In our demonstration system this meant that the actual pull-in would occur with a variation of  $\pm 1$  cycle of the spiral scan, for rms jitter less than or equal to 2.1 bw.

### 11.9.6 Probability of Pull-in

The probability of pull-in is affected by the spiral scan parameters (ring to ring spacing and tangential velocity), the rms jitter amplitude of the signal during handoff, the authority limit of the spatial tracker in handoff mode, and the signal photon arrival rate. In order to characterize the pull-in probability, a series of trials were performed in which the signal was located 3 to 5 bw outside of the receiver FOV, and pull-in was initiated with various initial conditions. In these trials one of two spiral scans was used: a fast scan with 1 bw/ms tangential velocity and 1.1 bw spacing between rings, or a slow scan with

0.5 bw/ms tangential velocity and 0.55 bw spacing between rings. Gaussian noise as described in Section 11.9.5 was introduced at rms levels of 0.4 or 2.1 bw/axis. The signal photon arrival rate was varied from -6 dB to +10 dB relative to the budgeted level of  $1.3 \times 10^{10}$  photons/s.

**Effects of Tracker Authority Limits on Probability of Pull-in.** As described in Section 11.9.4, when the handoff mode tracker authority limit was much larger than  $\pm 1$  beamwidth, the pull-in process could fail because the discriminant changed sign at large angular disturbances and at high signal photon arrival rates. However, when the tracker authority limit was reduced to less than  $\pm 0.75$  bw, no missed pull-ins were observed in 2000 trials for the fast spiral scan in the absence of angular disturbances and at a photon arrival rate 10 dB above budget, which represented a worst case scenario. The pull-in performance was not measurably different at high photon arrival rates when the authority limits were set to either  $\pm 0.75$  or  $\pm 0.5$  bw.

**Effects of RMS Jitter and Photon Arrival Rate on Probability of Pull-in.** The transition between handoff mode and spatial tracking was enabled by comparing the output of an envelope detector in the communications channel to a preset threshold voltage. At lower input photon arrival rates a relatively smaller angular disturbance would reduce the communications channel envelope detector below the transition threshold, which would cause the spatial tracker to revert to the handoff mode. However, as long as the residual jitter was less than 0.2 to 0.3 rms bw, no pull-in failures were recorded in 2000 trials for input photon arrival rates 6 dB below the nominal photon arrival rate of  $1.7 \times 10^{10}$  photons/s. When the residual jitter approached 0.5 rms bw the tracker was in a nearly continuous transition between handoff and spatial tracking. Note that these levels of residual jitter were more than five times the expected levels for LITE. In summary, the pull-in process was more robust than the spatial tracker.

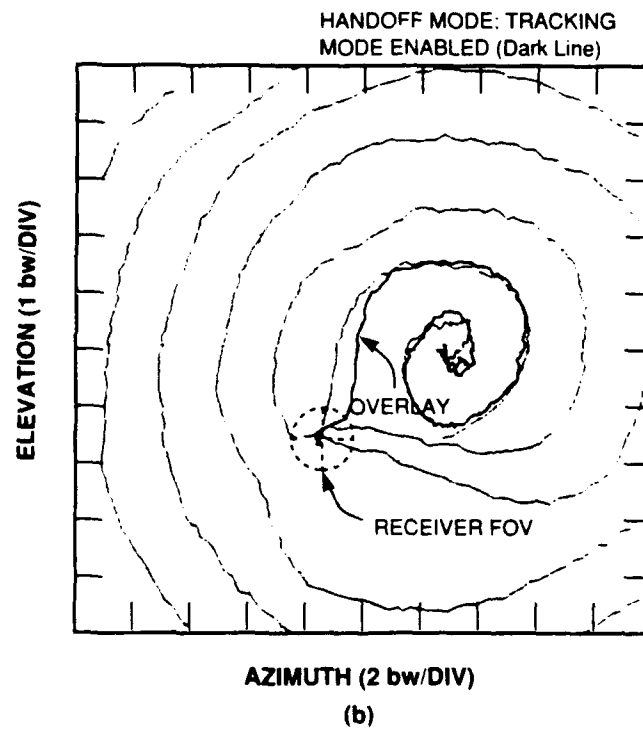
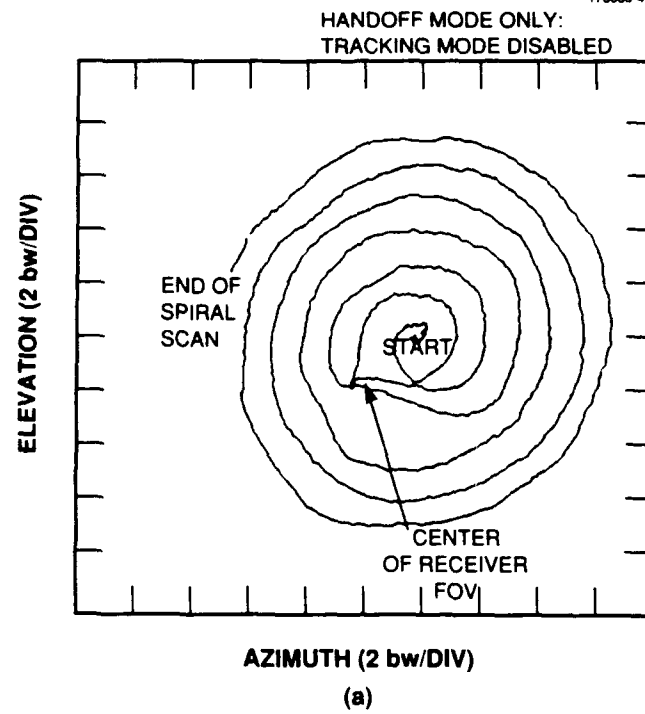


Figure 45. (a) Handoff spiral scan with tracking disabled (limited authority tracker). (b) Comparison of limited and full authority tracker.

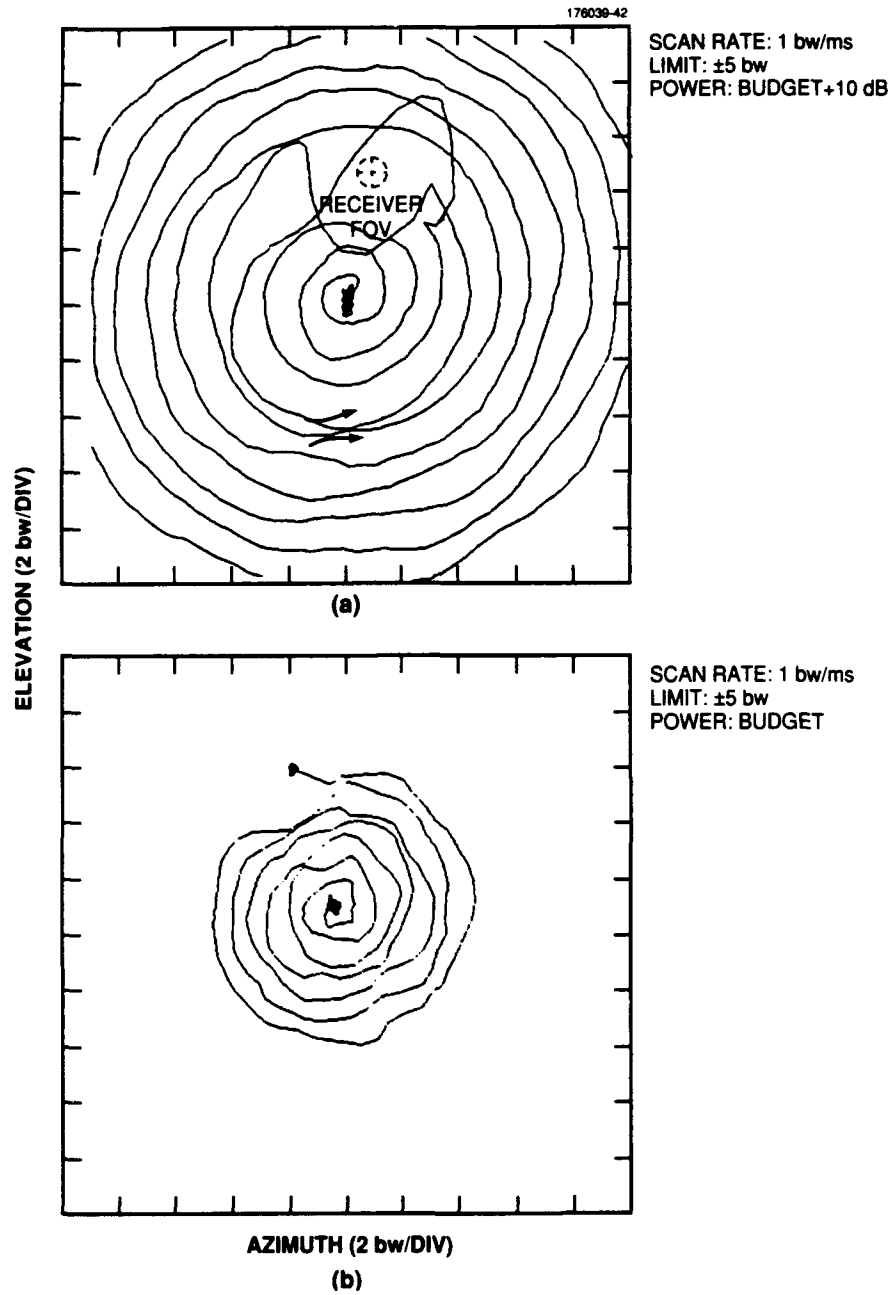


Figure 46. (a) Effects of positive feedback on pull-in transient. (b) Effects of positive feedback on pull-in transient.

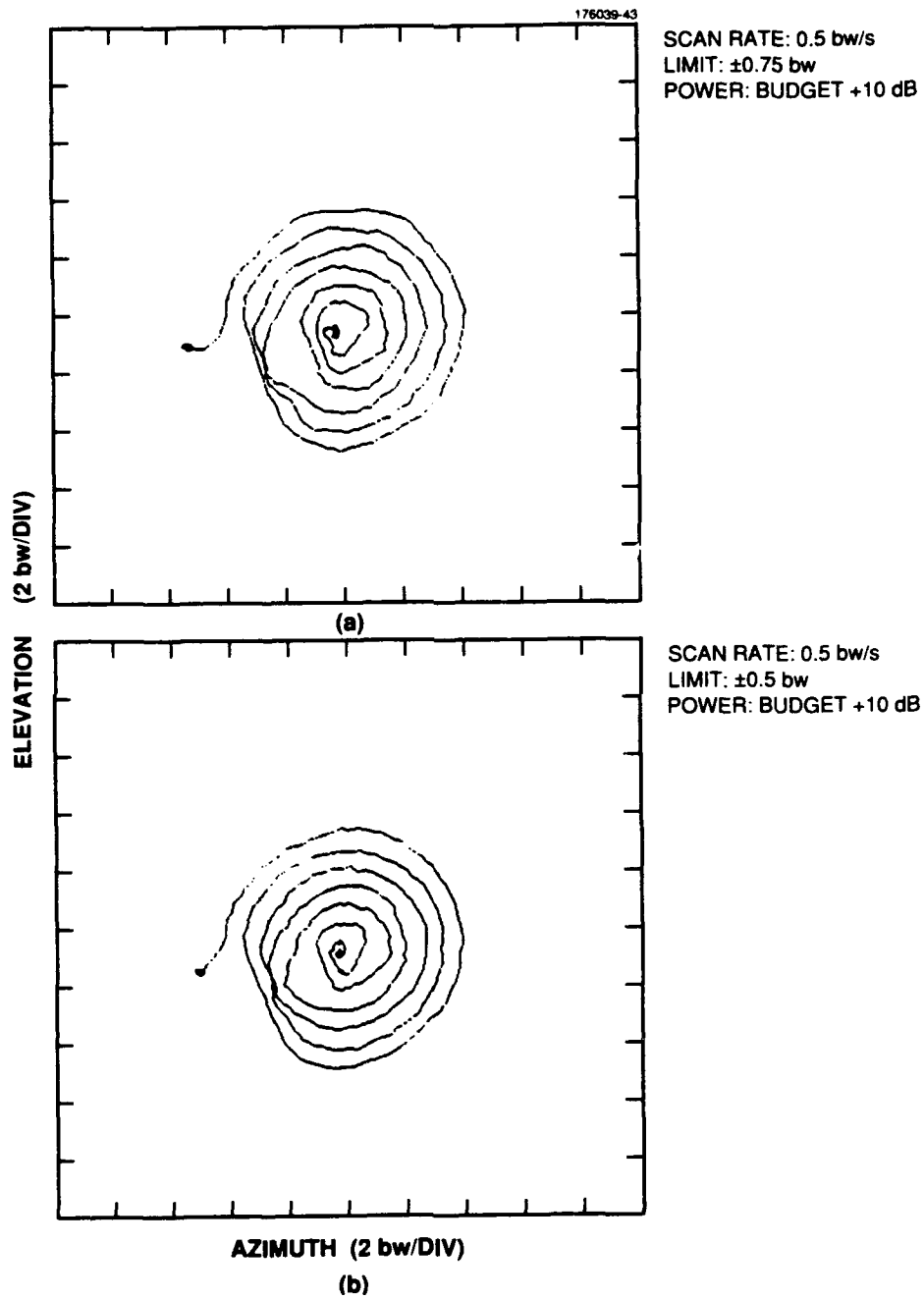


Figure 47. Improvement of pull-in transient by adjusting tracker authority limit.

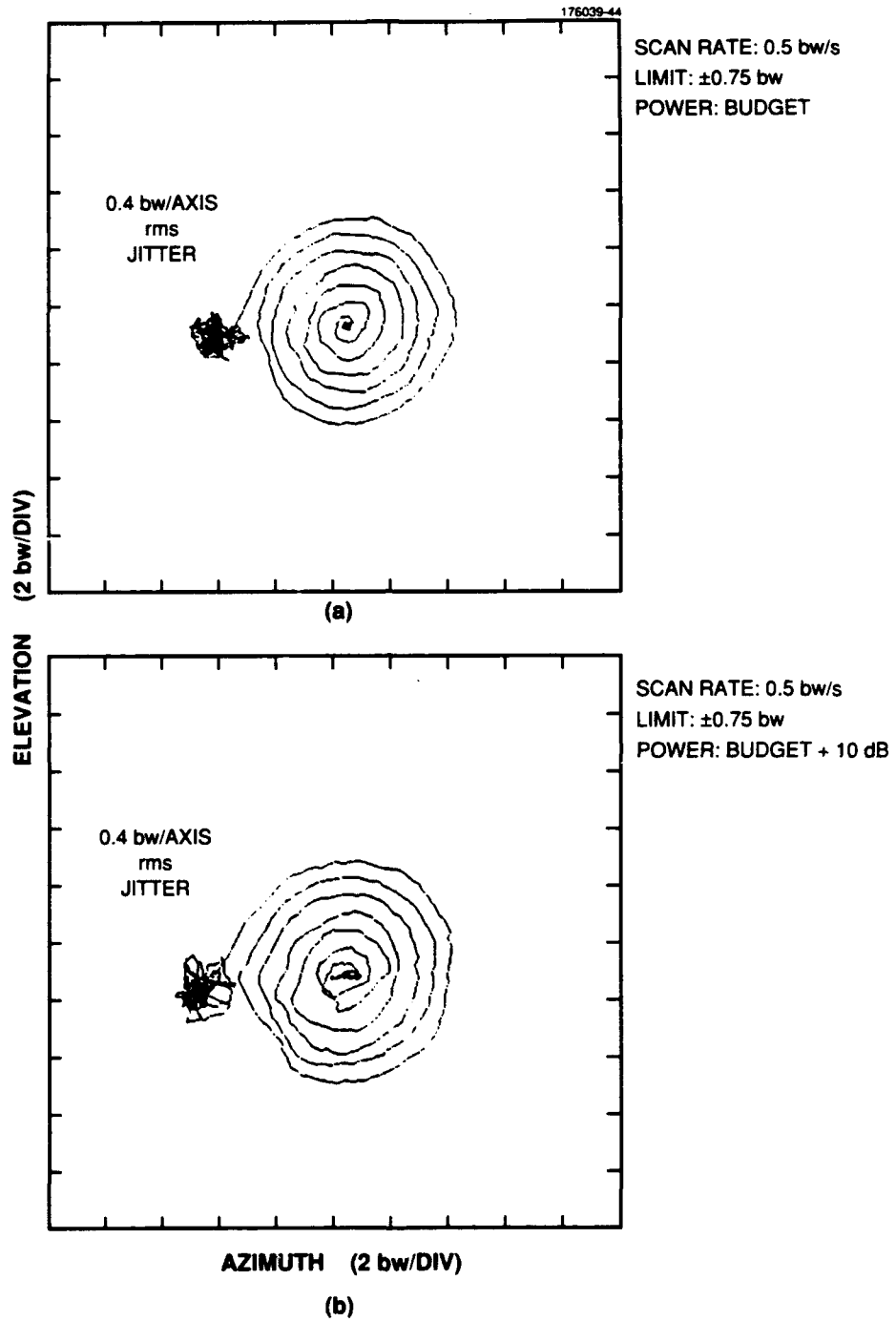


Figure 48. (a) Pull-in trajectory with 0.4 bw/axis rms noise, budget input signal power. (b) Pull-in trajectory with 0.4 bw/axis rms noise, budget + 10 db signal input power.

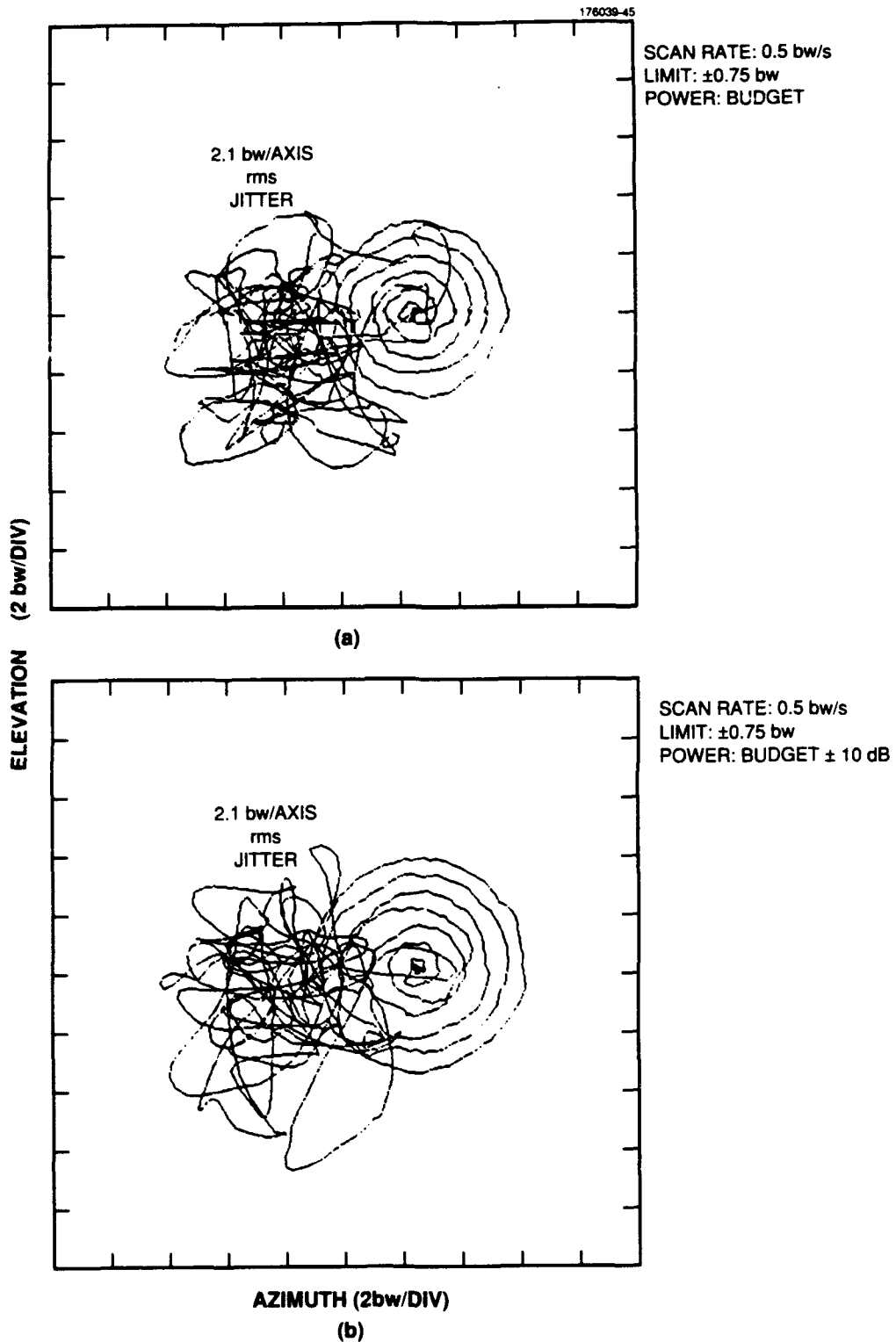


Figure 49. (a) Pull-in trajectory with 2.1 bw/axis rms noise, budget signal power. (b) Pull-in trajectory with 2.1 bw/axis rms noise budget + 10 dB input signal power.

## 12. CONCLUSIONS

A 110 Mb/s, binary FSK laboratory demonstration receiver has been developed and demonstrated, which included spatial acquisition and tracking subsystems, that is suitable for use in a communications link such as that proposed for the LITE. A description of the microjitter environment was developed based upon LITE, and the resultant disturbance spectrum is conservative when compared with on-orbit measured data from the Landsat-4 and Olympus satellites. Requirements for the spatial acquisition and tracking system were presented, based in part on the expected microjitter environment in LITE.

The spatial acquisition system was based upon a commercially available CCD array that was used to perform a parallel search to initially locate the incoming signal beam during acquisition. The expected accuracy, both with and without jitter, and the probability of successful acquisition were derived and compared with measured data from the laboratory demonstration system. The effects of CCD imperfections and variations in signal photon arrival rate and signal angle of arrival were described and documented. A pixel masking routine was developed to reduce the acquisition noise floor that resulted when a few excessively noisy pixels dominated acquisition performance at low photon arrival rates. The demonstrated spatial acquisition system met the LITE system requirements with 12.5 dB of margin.

The spatial tracker was based on measurement in the pupil plane of the angle of arrival difference between the LO and the signal beam. A commutating, correlation demodulator was developed to provide a high precision, bias-free error signal for use in the closed loop spatial tracker. Because of the commutation the spatial tracking demodulator was predicted to have an NEA which was a factor of 1.6 greater than that of a simple correlation processor (the inherent loss could be reduced from 1.6 to 1.1 through the use of a second correlation channel in which the commutation sequence was reversed with respect to the first channel). The discriminant gain in each axis of the spatial tracker was within 8 percent and 4 percent of the predicted values, in the elevation and azimuth axes, respectively. The spatial tracker did not operate at the quantum shot noise limit due to imperfect front end amplifier/detector combinations, but did operate with NEAs in each axis which were within 5 percent of the expected values after excess front end noise and the effects of demodulator commutation were taken into account. BER curves were measured both with the spatial tracker on and off and in the presence of high frequency angular disturbances similar to those expected on LITE. The BER of the receiver was essentially unaffected by these angular disturbances, which were far in excess of the level necessary to shut down the link without active spatial tracking.

A robust handoff algorithm was developed, for which no failures were observed in approximately 2000 trials, and which reduced the accuracy requirements on the spatial acquisition system to easily realizable levels. The handoff algorithm employed a constant tangential velocity, outward spiral search initiated at the incoming signal beam location as determined by the spatial acquisition system. The spatial tracker was partially enabled during this search, such that if the signal were swept across the communications receiver FOV then the partially enabled spatial tracker would center the signal within the receiver FOV. When the signal was approximately centered within the receiver FOV, and if the detected signal photon arrival rate exceeded a preset threshold, the spatial tracker was fully enabled and spatial

tracking proceeded normally. The handoff algorithm was found to be sensitive to sign reversals in the spatial tracker discriminant off boresight at high signal photon arrival rates. The algorithm could be made robust when facing these reversals by limiting the range of the partially enabled spatial tracker to less than  $\pm 0.75$  bw. Data from the demonstration system confirmed that successful handoffs were possible given any combination of signal photon arrival rate and angular disturbance level that would subsequently allow the spatial tracker to meet system requirements.

In summary, a laboratory breadboard of a spatial acquisition and tracking system suitable for intersatellite optical communications links has been described, analyzed, and demonstrated. Robust performance has been demonstrated that is well-predicted by theoretical models of the system.

## APPENDIX A TORQUE MOTOR BEAM STEERER CONTROL

This appendix details the design of the control circuitry for the torque motor beam steerers (TMBS) used as fast steering mirrors in the demonstration system. The position sensor that is part of each TMBS is first discussed, and then the current source, which is used as a driver for each TMBS, is presented.

### A.1 TMBS SHAFT POSITION SENSOR

TMBSs from General Scanning, Model Z2046 were used; they have a capacitive shaft position sensor built into each unit. The basic sensor is shown in Figure A-1. The capacitors C1 and C2 vary differentially as the shaft is turned. At the null position the capacitors are each approximately 11 pF.

In order to use the sensor to detect shaft position the diode bridge is driven with a capacitively-coupled common mode signal. During the positive half of the common mode drive signal a positive charge,  $C1 \Delta v$  and  $C2 \Delta v$ , is transferred onto C1 and C2, respectively, through diodes D1 and D4. The average current  $I1^+$  (averaged over one cycle of the drive voltage) is  $C1 \Delta v / \Delta T$ , while  $I2^+$  is similarly  $C2 \Delta v / \Delta T$ . During the negative half cycle of the drive voltage C1 discharges through D2, and C2 discharges through D3, which yields average currents  $I1^- = -C2 \Delta v / \Delta T$  and  $I2^- = -C1 \Delta v / \Delta T$ . The average dc current  $I1$  may then be obtained by adding  $I1^+ + I1^- = (C1 - C2) \Delta v / \Delta T$ .  $I2$  is obtained similarly as  $(C2 - C1) \Delta v / \Delta T$ . The resultant dc currents  $I1$  and  $I2$  are then detected with current to voltage converters. It is important that the current to voltage converters have low input impedance at frequencies below a few kilohertz (so as to accurately detect the expected shaft motion), and also have a high input impedance at the drive frequency (2 MHz), in order to block out the drive signal.

A commercially available oscillator board is used, Model OD-401, supplied by General Scanning. The board includes a blocking oscillator designed to supply approximately 200 V p-p at 2 MHz to the TMBS sensor, a half-wave rectified output that is used to sense the amplitude of the drive voltage, an amplitude control input, and the coupled inductor shown in Figure A-1 that is used as a common mode high frequency filter at the inputs to the current to voltage converters.

The circuit shown in Figure A-2 included the additional circuitry necessary to implement an AGC loop for the oscillator and to provide the current to voltage conversion. The offset adjust resistor R11 was selected to match the offset voltage of the particular TMBS with which the demodulator circuit was used.

Results from a prototype demodulator circuit are shown in Figure A-3. The only difference between the prototype and the demodulators used in the demonstration system is that the prototype had a factor of 8.4 more gain in the output stage U4. The measured rms deviations from linearity are less than 2 percent and are within the resolution within which the shaft angle for this test could be determined.

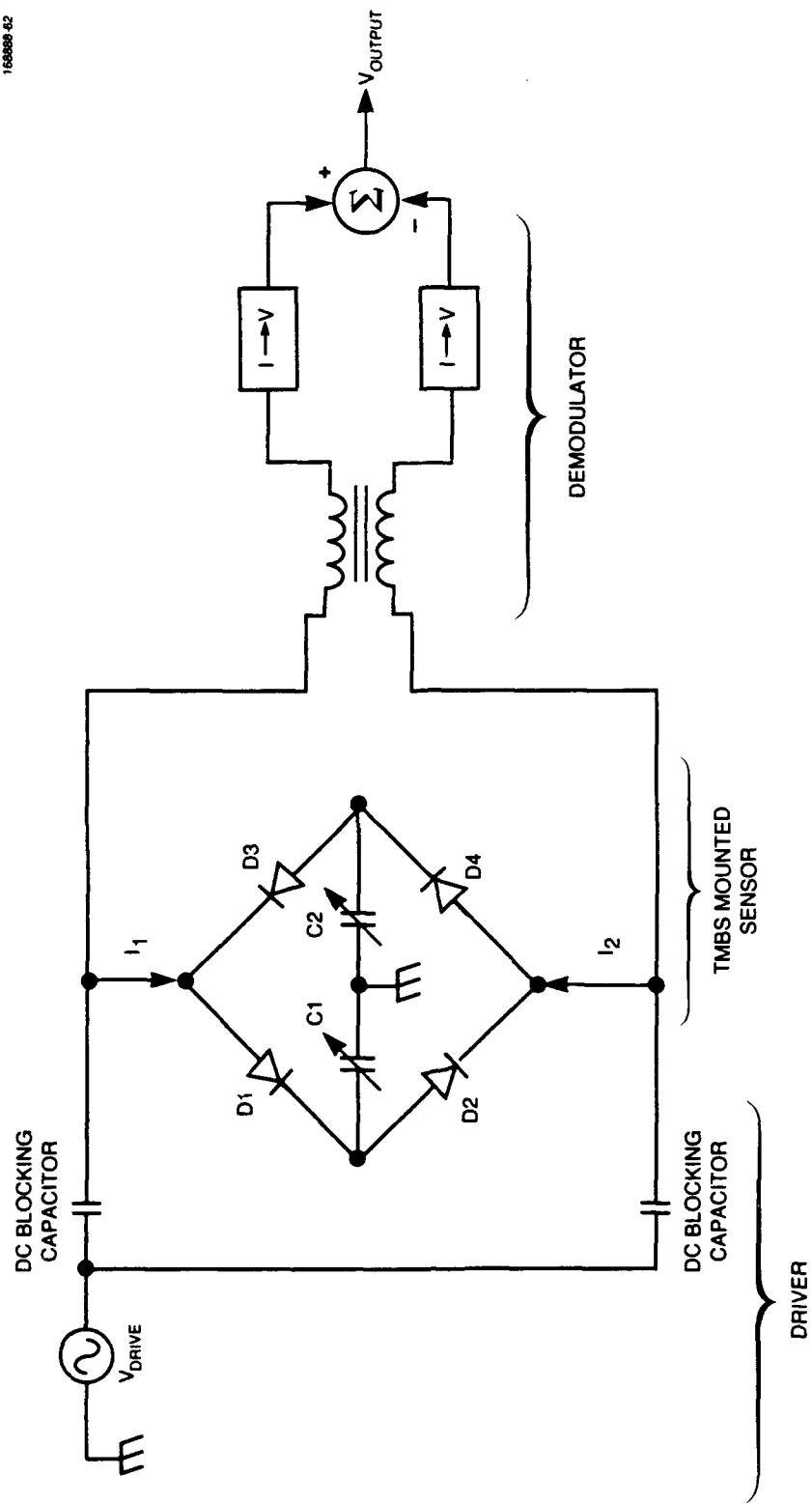


Figure A-1. TMBS shaft position sensor.

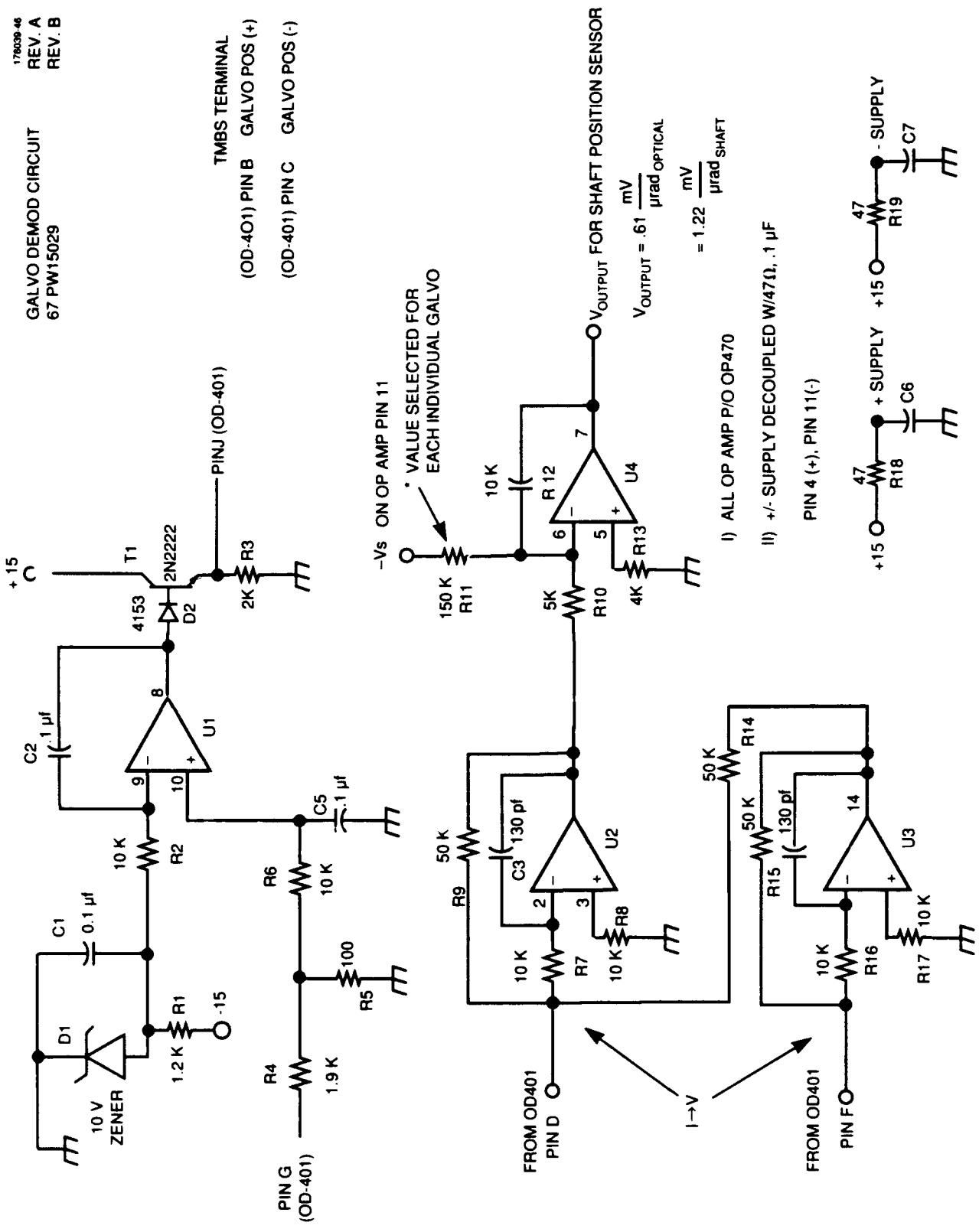


Figure A-2. Shaft position sensor demodulator.

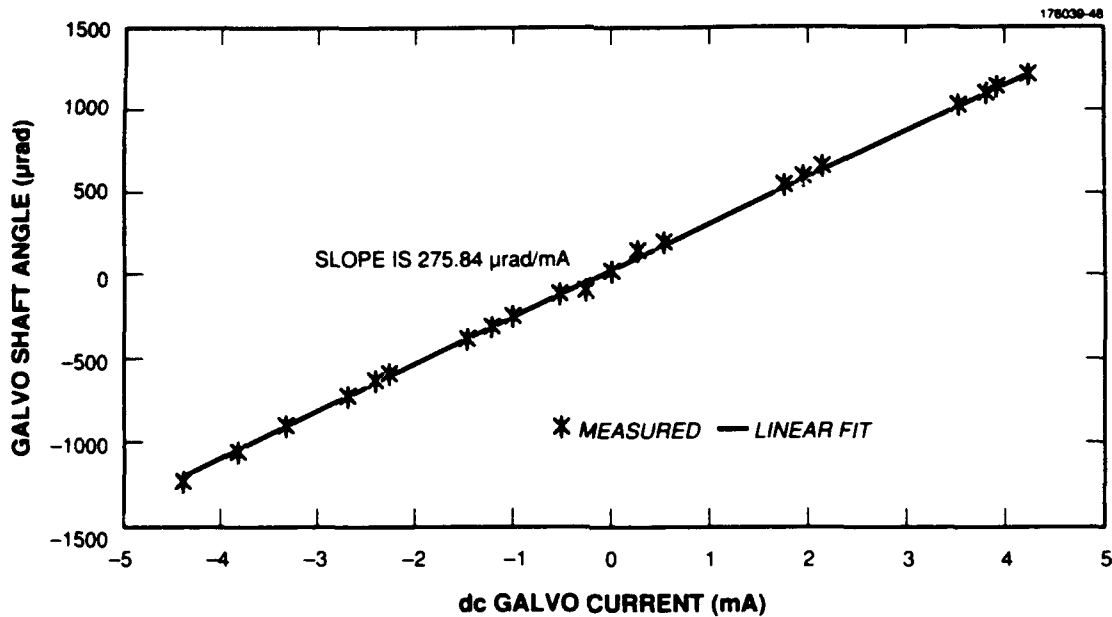


Figure A-3. TMBS shaft position sensor calibration.

## A.2 CURRENT DRIVER CIRCUIT FOR TMBS

In order to control the TMBSs in such a way that variations in the inductance of the torque coils would not change external system performance, a closed loop current source was designed to drive the TMBSs. Also, in order to remove problems associated with the high  $Q$  resonance associated with the first mode of the mirror/TMBS combination, located at 109 Hz, velocity feedback was added that was derived from the position sensor (described in Section A.1) to increase the damping. The current driver is shown in Figure A-4.

A  $20\ \Omega$  sense resistor, combined with the 10:1 ratio between  $R_x$  and  $R_y$ , yielded a low frequency voltage to current conversion gain of 5 mA/V. The current response was flat to beyond 15 kHz.

The velocity feedback is ac coupled through capacitor C12 and provides sufficient damping at the resonance frequency 109 Hz to obtain critically damped time responses for the closed loop system. Because only the derivative of the position sensor output is used, the system is insensitive to bias variations in the sensor output.

The dc linearity of galvanometer position vs drive current is shown in Figure A-5. The measured linearity was better than 3 percent.

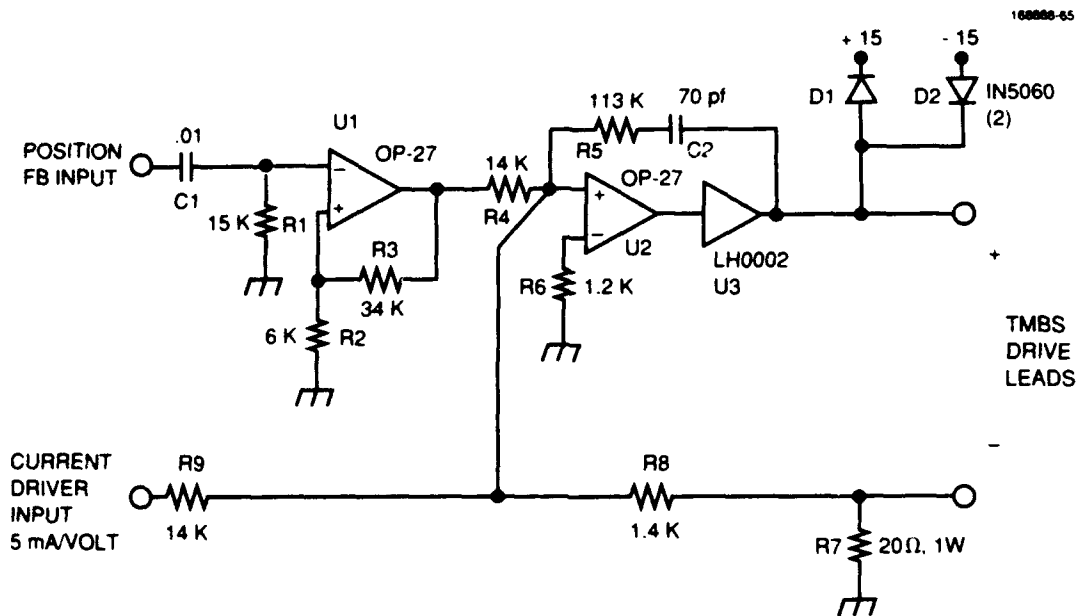


Figure A-4. TMBS current driver.

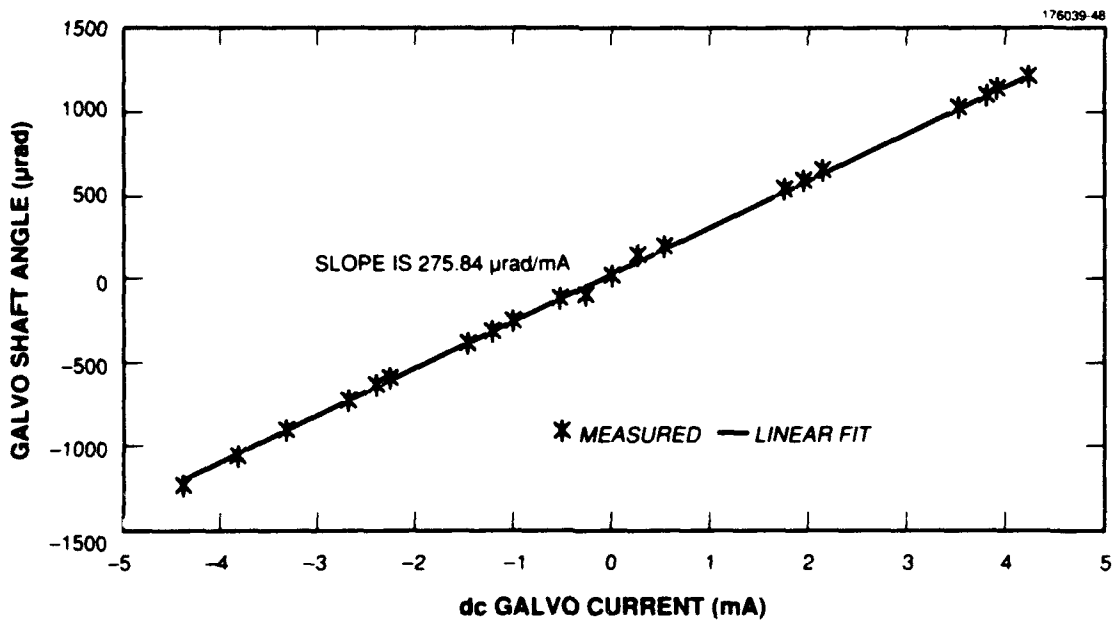
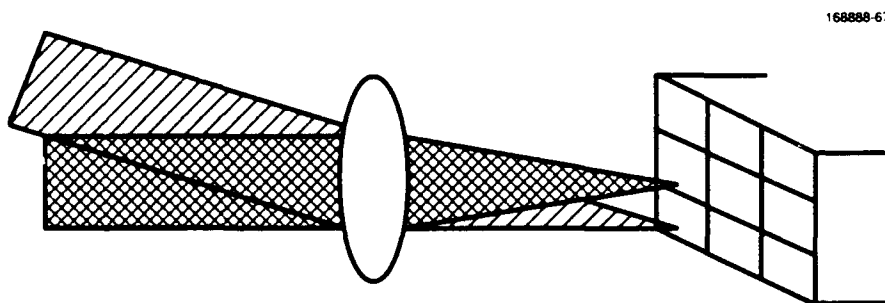


Figure A-5. TMBS shaft angle vs drive current.

## APPENDIX B CCD PRIMER

CCD imagers respond to a wide spectral range, from 0.1 to 1100 nm [41,42]. CCDs excel at low-light imaging; laboratory cameras exist with noise floors that are less than 3 rms electrons per pixel [43]. CCD imagers have already enjoyed great success in a number of major projects. Examples include NASA's Galileo-Jupiter Orbiter [44,45], which uses an  $800 \times 800$  pixel virtual-phase array from Texas Instruments (TI), the European Space Agency's Giotto Mission to Comet Halley [46], which uses a  $390 \times 584$  TI virtual-phase array, and the Hubble Space Telescope [47,48], which uses a TI  $800 \times 800$  pixel three-phase array. A four-phase  $64 \times 404$  pixel CCD was designed specifically for the NASA's Shuttle Image Spectrometer Experiment [49].

When used as an acquisition imager, a CCD array is placed in the back focal plane of a lens, which converts an incoming angle to a positional translation within the array as shown in Figure B-1. Signal integration time is selected as a function of signal and noise of the system. Using a parallel architecture, charge is simultaneously integrated over a wide field of view (FOV) with a resolution that is determined by the ratio of the focused spot size to CCD pixel size.



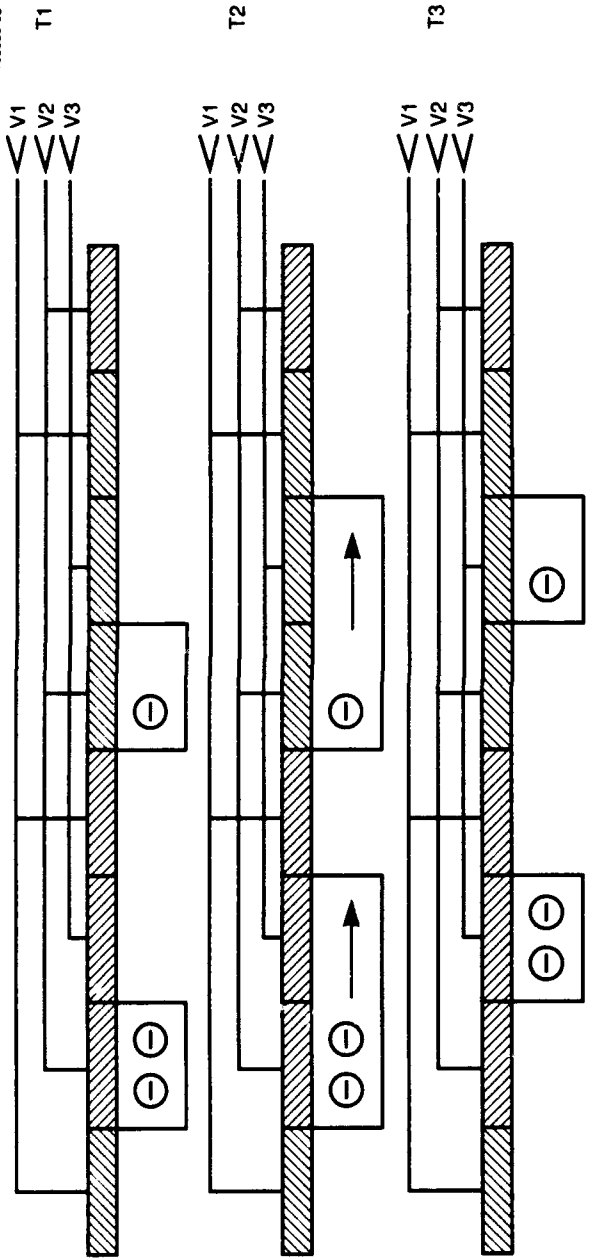
**TRANSLATING ANGLE TO POSITION**

*Figure B-1. Angle-to-position conversion.*

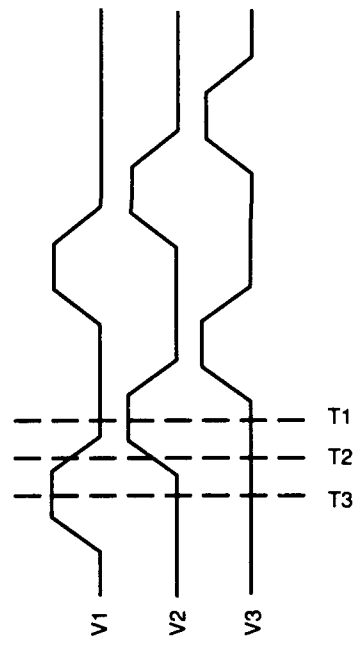
### B.1 OPERATION

A CCD is a high-resolution, low noise, integrating, direct detection array sensor that converts incident photons to electrons. Photoelectrons are generated within each pixel of the array as a function of the number of photons incident on the pixel and the photon-to-photoelectron conversion probability, or quantum efficiency, which is dependent upon wavelength. The charge is collected under an electrode gate and stored in a MOS capacitor potential well. The charge is then transferred serially out of the array using pulses of positive voltage to push charge along in "bucket brigade" fashion, as illustrated in Figure B-2. Finally, the charge is converted to a proportional voltage at the output of the CCD array.

160000-68



**CHARGE TRANSFER: THREE GATES PER PIXEL**



**CLOCKING SCHEME**

Figure B-2. CCD drive voltage timing diagram.

## **B.2 ARCHITECTURES**

Three types of CCD array architectures are commonly used for electronic imaging: interline transfer, frame transfer, and full frame imaging (see Figure B-3). Each array collects photons on the imaging area during the integration time. The charge collected in the pixels of the imaging area may first be transferred to a storage area or may be directly shifted to a parallel-to-serial readout register.

### **B.2.1 Interline Transfer CCD Array**

An interline transfer CCD has a storage array intermeshed with the imaging array. The charge collected on each line of imaging area during integration time is transferred under the adjacent interline mask. Each mask is then read out serially through a parallel-to-serial shift register. Since transfer from the imaging zone to the mask is so quick, the integration duty cycle is essentially 100 percent. Because the interline mask blocks incoming photons, during readout there is no need for a shutter and there is no image smearing. However, each strip covered by the interline mask is a dead zone not sensitive to incoming photons.

### **B.2.2 Frame Transfer CCD Array**

A frame transfer array provides the high frame rate needed for conventional television broadcast. It is composed of two arrays in tandem: one performs the imaging operation and the other, covered by an opaque mask, serves as temporary storage area for image data. Charge is quickly shifted line-by-line from the imaging section to the storage section, typically in about 1 ms. In most applications this is fast enough to keep image blur to an acceptable level without using a shutter. Following transfer, the imaging section can integrate another image while the stored data are read out through a parallel-to-serial register. This architecture is commonly operated continuously at television frame rates. Without the opaque mask the array can operate as a full frame imager.

### **B.2.3 Full Frame CCD Array**

A full frame array collects photons on the imaging area during the integration time, then transfers the charge collected in every pixel, row by row, directly to a parallel-to-serial shift register for serial readout. During data transfer a shutter typically blocks the imaging area so that the image is unaltered by photons arriving during the readout process.

A full frame CCD array was chosen for our receiver acquisition system in order to eliminate dead zones within the active area of the sensor and because high frame rates were not necessary. The Tektronix TK512M, a full frame array of  $512 \times 512$  pixels, was selected because it had specifications that met system noise and sensitivity requirements and was commercially available from an American manufacturer.

Other manufacturers of commercially available CCDs include Texas Instruments, Kodak, Thompson-CSF, and Photometrics.

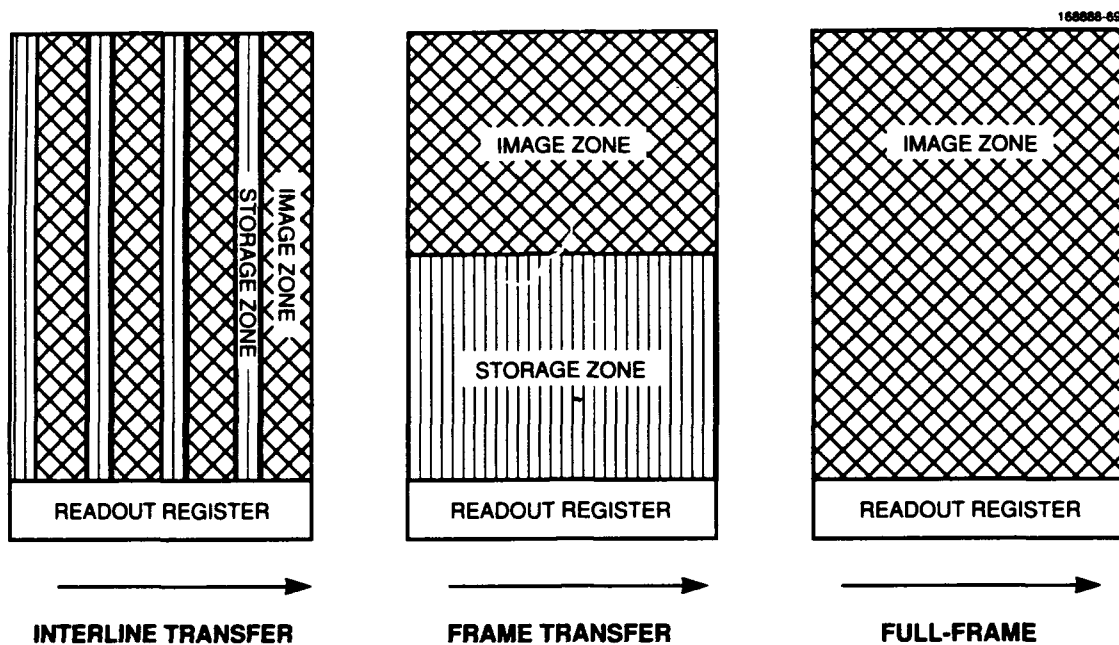


Figure B-3. CCD architectures.

### B.3 CHARACTERIZATION

CCDs are commonly characterized by resolution, quantum efficiency, full-well charge, dark current, read noise, crosstalk, and charge transfer efficiency. A number of papers have been published regarding the characterization of CCDs [21,22,43,50,51].

#### B.3.1 Quantum Efficiency

Quantum efficiency (QE) is the incident photon-to-electron conversion probability. An incoming photon must penetrate the electrode layer and generate an electron in order to be detected. Electrode reflectivity can prevent photons from penetrating to the substrate, degrading quantum efficiency. Furthermore, the quantum efficiency drops at shorter wavelengths due to absorption in the electrodes and at longer wavelengths due to generation of electrons too deeply for efficient collection in potential wells. Good quantum efficiency is necessary to maximize the sensitivity of the CCD array.

CCDs are commonly available which have quantum efficiencies as high as 40 to 45 percent. Examples of such CCDs include the Thomson TH 7863 (at a wavelength of 790 nm), the Photometrics PM512 (at a wavelength of 700 nm), and the Kodak KAF-1400 (at a wavelength of 650 nm). At 860 nm typical quantum efficiencies drop to approximately 30 percent for the PM512, 29 percent for the TH 7863, and 20 percent for the KAF-1400. The quantum efficiency for these devices falls below 10 percent at wavelengths longer than approximately 960 nm and shorter than 430 nm. Methods to improve CCD QE are discussed in the literature [22,43].

### B.3.2 Full-Well Capacity

Full-well capacity defines the saturation limit, in electrons, for each pixel. Typically this number is above  $10^5$  electrons. The difference between the full-well capacity and the minimum noise per pixel in rms electrons, divided by the quantum efficiency of the device, determines the dynamic range of the sensor.

### B.3.3 Dark Current

Dark current is the rate of thermally-generated charge accumulation within the CCD imaging region. Dark current, as the name implies, is independent of photon arrival rate but doubles for every  $7^\circ\text{C}$  temperature increase near room temperature. An average dark current is commonly measured for the entire CCD array. By thermoelectric cooling to  $-100^\circ\text{C}$ , dark current has been reduced to less than  $1\text{ e-/s/pixel}$  [43]. For extremely long exposures the CCD can be cooled to  $-120^\circ\text{C}$  with liquid nitrogen. CCDs are not commonly operated at temperatures below  $-120^\circ\text{C}$  because the charge transfer efficiency degrades significantly.

### B.3.4 Read Noise

Read noise is generated by sources intrinsic to the CCD during the transfer of charge from the CCD to the outside circuitry. Examples include reset noise and amplifier noise [43]. Generally read noise is a function of readout rate and device temperature.

Reset noise results from variations in the reset voltage of the output node prior to a charge dump of a pixel during readout. This noise may be expressed [43], in rms electrons, as:  $N_r(e^-) = (kTC)^{1/2}/q$  where  $k$  = Boltzmann's constant,  $T$  = temperature in Kelvin,  $C$  = output capacitance,  $q$  = the electronic charge.

Correlated double sampling is often used to greatly reduce reset noise. Correlated double sampling refers to the practice of sampling the CCD output immediately after the reset pulse and then again after the charge dump. The difference between the two samples represents the signal charge, free from any added charge associated with the reset procedure. Without correlated double sampling the read noise floor is typically above  $200\text{ e-/pixel.rms}$  (see Section 7.3.4).

The on-chip amplifier is the main source of read noise. Voltages driving this amplifier, the reset transistor drain voltage, reset transistor gate clock, and source-follower drain voltage, most critically affect performance [51]. The reset drain, for example, provides the critical reference level following the reset pulse prior to the charge dump during readout.

### B.3.5 Charge Transfer Efficiency

Charge transfer efficiency (CTE) measures the percentage of collected charge that is transferred from one gate to the next. CTE decreases with increased clock frequency or gate length and will diminish at low temperatures. CTEs of 0.999995 can be obtained with today's fabrication technology. A

CTE > 0.99995 is routine today; scientific grade is 0.99997. The TK512M is specified to have a CTE of 0.99999. This parameter is critical: for the  $200 \times 200$  three-phase subarray selected, the 0.00004 difference between specification (0.99999) and a CTE of 0.99995 results in retaining 99 percent rather than 93 percent of the original signal in the last pixel, following transfer to the output. With a larger array, say a  $2048 \times 2048$  pixel array, the last value will represent only 54 percent of the original signal at a CTE of 0.99995, but 88.4 percent at 0.99999. Work done by Janesick et al. indicates that at low signal levels, below 1000 detected electrons, CTE is often worse than specification [43].

## APPENDIX C DERIVATION OF NEA FOR COMMUTATING, CORRELATION TRACKER

In this appendix the noise equivalent angle (NEA) for a commutating, correlation tracker is derived in more detail. The analysis will be based upon the processing illustrated in Figure 17. The analysis is performed for the azimuth track channel only; the elevation channel is exactly analogous. For convenience the appropriate equations from Section 10 are repeated;

$$v_{c,I}(t) = \frac{2I m(\theta)}{\sqrt{\gamma}} \sin \omega t + n_C(t) \quad I \text{ channel} \quad (C-1)$$

$$v_{c,Q}(t) = \frac{2I m(\theta)}{\sqrt{\gamma}} \cos \omega t + n_C(t) \quad Q \text{ channel} \quad (C-2)$$

$$v_{\text{left}}(t) = L' \left[ m(0)I \cos(\omega t + \zeta) + n_L(t) \right] \quad \text{Az, left} \quad (C-3)$$

$$v_{\text{right}}(t) = R' \left[ m(0)I \cos(\omega t - \zeta) + n_R(t) \right] \quad \text{Az, right} \quad (C-4)$$

$$R' = \left( \frac{1}{2} + \sum_{k=1}^{\infty} B_k \cos(k\omega_s t) \right) \quad \text{right track commutation} \quad (C-5)$$

$$L' = \left( \frac{1}{2} - \sum_{k=1}^{\infty} B_k \cos(k\omega_s t) \right) \quad \text{left track commutation} \quad (C-6)$$

$$B_k = \frac{\sin \frac{k\pi}{2}}{\frac{k\pi}{2}} \quad (C-7)$$

$$I = \frac{e\eta}{h\nu} \sqrt{\gamma P_C P_{LO}} \quad (C-8)$$

where  $\omega$  is the heterodyne IF frequency, between 0.1 and 1 GHz in our system,  $\zeta \approx K_D \theta$  for small  $\theta$ , and  $\theta$  is the angular misalignment between the signal and LO beams in units of angular beamwidths corresponding to the full width, half maximum of the far field intensity profile of the signal beam. The commutated track signal is obtained by substituting Equations (C-5) to (C-7) into Equations (C-3) and (C-4) and then taking the sum of  $v_{\text{left}}(t)$  and  $v_{\text{right}}(t)$ . Following correlation with the I channel communications signal, bandpass filtering, and synchronous detection, the baseband output may be written in the following form

$$V_I(t) = V_{\text{SXS}}^I(t) + n_{\text{SxN}}(t) + n_{\text{Nxn}}(t) \quad (C-9)$$

Each of the three terms will be discussed separately.

## C.1 SIGNAL × SIGNAL

The signal portion of the  $v_{\text{track}}(t) = v_{\text{left}}(t) + v_{\text{right}}(t)$  is given by

$$\begin{aligned} v_{\text{track}}(t) &= \frac{m(0)I}{2} \{ \cos(\omega t + \zeta) + \cos(\omega t - \zeta) \} + \\ &\quad m(0)I \{ \cos(\omega t - \zeta) - \cos(\omega t + \zeta) \} \sum_{k=1}^{\infty} B_k \cos k\omega_{\text{sample}} t \\ &= m(\theta)I \cos \omega t + 2m(0)I \sin \zeta \sin \omega t \sum_{k=1}^{\infty} B_k \cos k\omega_{\text{sample}} t \end{aligned} \quad (\text{C-10})$$

where it is helpful to recall the definition in Equation (46) that  $\cos \zeta = m(\theta)/m(0)$  and  $\sin \zeta = q(\theta)/m(0)$ . Keeping only the terms at the sample frequency  $\omega_{\text{sample}}$ , the post-correlation signal may be written as

$$v_{\text{track}}(t) = \frac{4I^2}{\pi\sqrt{\gamma}} m(\theta)m(0) \sin \zeta \cos \omega_{\text{sample}} t \quad \text{post-correlation.} \quad (\text{C-11})$$

Following the bandpass filter centered at  $\omega_{\text{sample}}$ , and subsequent multiplication by  $2 \cos \omega_{\text{sample}} t$  for synchronous demodulation, the in-phase baseband output is

$$V_{\text{sxs}}^I(t) = \frac{4I^2 m(\theta)}{\sqrt{\gamma} \pi} \sin \zeta \quad (\text{I channel, after synch demod}). \quad (\text{C-12})$$

The quadrature correlation output is used for normalization. The quadrature communications channel is biphase modulated at the chopping frequency  $\omega_{\text{sample}}$ , because otherwise the product of the Q channel and the commutated track channel has negligibly small components at  $\omega_{\text{sample}}$  for small  $\theta$ . The biphase modulated Q channel communications signal (keeping only the term at  $\omega_{\text{sample}}$ ) is

$$v_{c,Q}(t) = \frac{8I m(\theta)}{\pi\sqrt{\gamma}} \cos \omega t \cos \omega_{\text{sample}} t \quad (\text{C-13})$$

Correlation of the chopped Q channel communications signal with the commutated track signal  $v_{\text{track}}(t)$ , and again keeping only the terms at the sample frequency  $\omega_{\text{sample}}$ , yields

$$V_{\text{sxs}}^Q(t) = \frac{4I^2 m^2(\theta)}{\pi\sqrt{\gamma}} \cos \omega_{\text{sample}} t \quad (\text{C-14})$$

Bandpass filtering to isolate the  $\omega_{\text{sample}}$  term and subsequent synchronous demodulation (multiplication by  $2 \cos \omega_{\text{sample}} t$ ) yields the following baseband term

$$V_{sxs}^Q(t) = \frac{4I^2 m^2(\theta)}{\pi\sqrt{\gamma}} \quad (C-15)$$

The normalization is performed by taking the square root of the sum of the squares of the I and Q channel outputs. If the small angle approximation  $K_D\theta \approx \sin(K_D\theta)$  is not made in the expression for the baseband I channel output, then the normalization voltage may be written as

$$V_{\text{normalization}}(t) = \sqrt{\left(V_{sxs}^Q(t)\right)^2 + \left(V_{sxs}^I(t)\right)^2} = \frac{4I^2 m(0)m(\theta)}{\pi\sqrt{\gamma}} \sqrt{\frac{m(\theta)^2}{m(0)^2} + \sin^2 \zeta} \quad (C-16)$$

Recall from Equation 46 that  $m(\theta)/m(0) = \cos\zeta$ , which makes it apparent that the square root term on the right side of Equation (C-16) is unity. Thus

$$V_{\text{normalization}}(t) = \frac{4I^2 m(0)m(\theta)}{\pi\sqrt{\gamma}} \quad (C-17)$$

and Equation (56) is obtained

$$\bar{V}_o(\theta) = K_D\theta + \frac{\pi\sqrt{\gamma}}{4m^2(0)I^2} \left\{ n_{sxn}(t) + n_{nxs}(t) \right\} \quad (C-18)$$

where the approximations  $m(\theta) = m(0)$  and  $\sin\zeta = K_D\theta$  have been made for small  $\theta$ .

## C.2 SIGNAL $\times$ NOISE

The dominant signal  $\times$  noise term,  $n_{sxn}(t)$ , is formed by the product of the communication signal,  $V_{c,f}(t)$ , and the commutated track noise, and may be written as

$$n_{sxn}(t) = \frac{2I m(\theta)}{\sqrt{\gamma}} \sin \omega t \left[ \left( n_{\text{left}}(t) + n_{\text{right}}(t) \right) \frac{1}{2} + \left( n_{\text{right}}(t) - n_{\text{left}}(t) \right) \sum_{k=1}^{\infty} B_k \cos k\omega_{\text{sample}} t \right] \quad (C-19)$$

It will be convenient to derive the power spectral density,  $N_{sxn}(f)$ , of  $n_{sxn}(t)$  and then find the variance by integrating  $N_{sxn}(f)$ . First it will be necessary to model the effects of the commutation on the track noise.

The noise in each track channel is white with power spectral density  $N_o/4$ . Recall that the communications channel noise  $n_c(t)$  or  $\tilde{n}_c(t)$  is also white, with spectral density  $N_o/2$ . The commutation process alternately connects first one track channel noise, and then the other, to the output of the commutation switch. If the two track channel noises are uncorrelated and white, alternating between them should yield the same spectral density, and hence the same variance as either channel alone. This is derived more rigorously as follows.

Note that multiplying wideband white noise (spectral density  $N_o$ , bandwidth  $W$ ) by a sinusoid  $A \sin \omega t$ , where  $\omega < W$ , produces noise with a low frequency spectral distribution that is still white, and a spectral density that is  $N_o A^2/2$ . Next, note that the spectral density of either the sum or difference of  $n_{\text{left}}(t)$  and  $n_{\text{right}}(t)$  is  $N_o/2$ . Recognizing that

$$B_k^2 = \left( \frac{2}{\pi k} \right)^2 \text{ for } k \text{ odd} \quad (\text{C-20})$$

and

$$\sum_{k=1}^{\infty} \left( \frac{2}{\pi k} \right)^2 = \frac{1}{2} \text{ for } k \text{ odd} \quad (\text{C-21})$$

the spectral density of  $n_{\text{sxm}}(t)$  may be written as

$$\begin{aligned} N_{\text{sxm}}(f) &= \frac{4I^2 m^2(\theta)}{\gamma} \frac{1}{2} \left[ \frac{N_o}{2} \frac{1}{4} + \frac{N_o}{2} \frac{1}{2} \sum_{k=1}^{\infty} B_k^2 \right] \\ &= \frac{4I^2 m^2(\theta)}{\gamma} \frac{1}{2} \left[ \frac{N_o}{4} \right] \end{aligned} \quad (\text{C-22})$$

which is the same as multiplying  $V_{c,1}(t)$  by the noise in either track channel alone, as expected. Note that this approximation for  $N_{\text{sxm}}(f)$  is only valid for  $f, \omega_{\text{sample}} \ll W$ .

Subsequent narrowband bandpass filtering at  $\omega_{\text{sample}}$  with single sided bandwidth  $F$  produces narrowband white noise, which may be approximated as  $n(t) = n_I(t) \cos \omega_{\text{sample}} t + n_Q(t) \sin \omega_{\text{sample}} t$ , where  $n_I(t)$  and  $n_Q(t)$  each have spectral density equal to twice that of the unfiltered noise. Synchronous demodulation and lowpass filtering (bandwidth  $F$ ) yields a baseband distribution that is white, bandlimited to bandwidth  $F$ , and has spectral density of

$$N_{\text{sxm}}(f) = \frac{I^2 m^2(\theta)}{\gamma} N_o \quad (\text{C-23})$$

The variance of  $n_{\text{sxm}}(t)$  within a single-sided bandwidth of  $F$  is then

$$\text{var} [n_{\text{sxm}}(t)] = \frac{2FI^2 m^2(\theta)}{\gamma} N_o \quad (\text{C-24})$$

### C.3 NOISE × NOISE TERM

The variance of the noise × noise term may be derived by first finding the spectral density of the commutated track noise term, convolving this with the spectral density of the noise in the communications channel, and then evaluating the integral of the post-bandpass noise to obtain the variance.

Recalling that the commutated track noise density is white with spectral density  $N_o/4$ , and bandlimited with bandwidth  $W$ , the convolution of the communication and commutated track noises yields a triangular distribution with spectral density at dc of  $N_o^2W/4$ . For frequencies much less than  $W$ , this distribution is approximated as rectangular with spectral density  $N_o^2W/4$ .

As before, the bandpass filtered noise is written as narrowband white bandpass noise  $n(t) = n_I(t) \cos \omega_{\text{sample}}t + n_Q(t) \sin \omega_{\text{sample}}t$ . The spectral density of both  $n_I(t)$  and  $n_Q(t)$  is  $2N_o^2W/4$ . Synchronous demodulation corresponds to multiplication by  $2 \cos \omega_{\text{sample}}t$ , and the spectral distribution of the post-demodulation noise × noise term is rectangular with spectral density  $N_o^2W/2$  for frequencies much less than  $W$ , which allows us to write the low frequency spectral density  $N_{\text{nxn}}(0)$

$$N_{\text{nxn}}(f) = \frac{N_o^2W}{2}, \quad f \ll W \quad (\text{C-25})$$

The variance of  $n_{\text{nxn}}(t)$  within the single-sided bandwidth  $F$  may now be expressed as

$$\text{var} [n_{\text{nxn}}(t)] = FN_o^2W \quad (\text{C-26})$$

### C.4 NEA FOR COMMUTATED CORRELATION PROCESSING

The NEA of the commutated correlation processor may be written as

$$\begin{aligned} \theta_{\text{NEA}} &= \left( E \left[ \left| \frac{\bar{V}_{\text{out}}}{K_D} - \theta \right|^2 \right] \right)^{\frac{1}{2}} \\ &= \frac{\left\{ \text{var} [n_{\text{sxn}}(t)] + \text{var} [n_{\text{nxn}}(t)] \right\}^{\frac{1}{2}}}{|Q|} \end{aligned} \quad (\text{C-27})$$

where  $Q = 4I^2K_D m^2(0) / \pi\sqrt{\gamma}$ . Substituting Equations (C-24) and (C-26) into (C-27) yields

$$\theta_{\text{NEA}} = \frac{\pi\sqrt{\gamma}}{4I^2m} \left( FN_o^2W + \frac{2FN_oI^2m^2}{\gamma} \right)^{\frac{1}{2}} \quad (\text{C-28})$$

For a quantum-shot-noise-limited system in which the LO optical power is much larger than the signal optical power,  $N_o = 2ei_{dc} = 2e^2\eta P_{LO}/h\nu$ . Substituting into Equation (C-28) for  $I$  [Equation (C-8)] and  $N_o$  obtains

$$\theta_{NEA} = \frac{\pi}{2K_D} \left( \frac{F}{\eta m^2 \gamma P_c} \right)^{1/2} \left( 1 + \frac{W}{\eta m^2 P_c} \right)^{1/2} \quad (C-29)$$

from which Equation (56) may be written.

## APPENDIX D LIST OF ACRONYMS AND SYMBOLS

$a$	radius for a truncated plane wave
$A_j(x,y)$	normalized E field distribution for LO ( $j = \text{LO}$ ) or signal beam ( $j = s$ )
acq	acquisition
ACTS	Advanced Communications Technology Satellite
ADC	analog-to-digital converter
AGC	automatic gain control
$B_k$	$k$ th Fourier coefficient for Fourier expansion of commutation signal
BER	bit error rate
bw	angular beamwidth, usually full width half maximum of the far field intensity profile
CCD	charge-coupled device
CDS	correlated double sampling
CNDR	carrier-to-noise density ratio
CNR	carrier-to-noise ratio
comm	communication
CMOS	complementary metal-oxide semiconductor
CPM	course pointing mirror
CTE	charge transfer efficiency
DAC	digital-to-analog converter
DPSK	differential phase shift keying
DN	digital number
DRAM	dynamic random access memory
$e$	electronic charge
$e^-$	electron
$E_j(x,y)$	electric field distribution for LO ( $j = \text{LO}$ ) or signal beam ( $j = s$ )
ESA	European Space Agency
F	single-sided noise bandwidth of heterodyne spatial tracker
FET	field effect transistor
FFT	fast Fourier transform

FOV	field of view
FSK	frequency shift keying
FSM	fast steering mirror
FWHM	full-width half-maximum
Gb/s	gigabit per second
GEO	geostationary earth orbit
GHz	gigahertz
$\gamma$	ratio of Az or El track signal power to communication signal power
$\Gamma_d$	dark current ( $e^-/s/pixel$ )
$\Gamma_s$	detected signal in photoelectrons/s
$\eta$	detector quantum efficiency
$h$	Planck's constant
IF	intermediate frequency
$J_n$	Bessel function of order $n$
$L'$	commutation signal, left channel
LEO	low earth orbit
LITE	Laser Intersatellite Transmission Experiment
LO	local oscillator
LOS	line of sight
LSB	least significant bit
$m^2(\theta)$	heterodyne mode matching efficiency
MAXBLOCK	location of $2 \times 2$ pixel group within CCD with largest detected signal
Mb/s	megabits per second
ms	millisecond
$N_f$	read noise ( $e^-/pixel$ rms)
$N_q$	ADC quantization noise ( $e^-/pixel$ rms)
$n_{n\alpha n}(t)$	noise term due to comm noise times track noise
$n_{s\alpha n}(t)$	noise term due to comm IF signal times track noise
$N_{n\alpha n}(f)$	spectral density of $n_{n\alpha n}(t)$
$N_{s\alpha n}(f)$	spectral density of $n_{s\alpha n}(t)$

$\nu$	optical frequency
NEA	noise equivalent angle
NEV	noise equivalent voltage or rms voltage
ns	nanosecond
OMS	opto-mechanical subsystem
OPD	optical path difference
$P_x$	optical power in channel $j$ for $j = \text{comm, track}$ ; optical power in LO or signal beam for $j = \text{LO, s}$
PMPCG	programmable multiphase clock generator
PPM	parts per million
PSD	power spectral density
PSK	phase shift keyed
$q(\theta)$	heterodyne discriminant function
$\theta$	angular misalignment between LO and signal beam
$\theta_{\text{NEA}}$	noise equivalent angle
$R'$	commutation signal, right channel
rad	radian
recvr	receiver
rms	root-mean-square
rss	root-sum-squa.
s	second
SNR	signal-to-noise ratio
SSB	single side band
T	CCD integration time
TMBS	torque motor beam steerer, also called a galvanometer
TTL	Transistor-Transistor Logic
$\bar{V}_o(\theta)$	normalized output of commutated, correlation processor
$W$	single-sided noise bandwidth of front end amplifiers in the heterodyne spatial tracker
$w$	radius for a Gaussian distribution
$\omega$	heterodyne IF frequency
$\omega_{\text{sample}}$	commutation or sampling frequency

## LIST OF REFERENCES

1. J.D. Barry, and G.S. Mecherle, "Communication channel burst errors induced by Gaussian distributed mispointing," *SPIE Proceedings*, Vol. 616, (1986), pp. 137-140.
2. G.A. Koepf et al., "Analysis of burst error occurrence on optical intersatellite link (ISL) design," *SPIE Proceedings*, Vol. 616, (1986), pp. 129-136.
3. A.F. Popescu et al., "Experimental investigation of the influence of tracking errors on the performance of free-space laser links," *SPIE Proceedings*, Vol. 885, (1988), pp. 93-99.
4. V.W.S. Chan, private communication.
5. R.S. Bondurant et al., "An Opto-Mechanical Subsystem for Space-based Coherent Optical Communications," *SPIE Proceedings*, Vol. 995, (1989), pp. 92-100.
6. J.E. Kaufmann and E.A. Swanson, private communication.
7. J.E. Kaufmann (memo, 1989).
8. E.A. Bucher (memo, 1987).
9. L. Jeromin (memo, 1987).
10. J. Sudey and J.R. Sculman, "In orbit measurements of Landsat-4," 35th Congress of International Astronomical Federation, Lausanne, Switzerland, (1984).
11. M. Wittig et al., "In orbit measurements of microaccelerations of ESA's communications satellite OLYMPUS," *SPIE Proceedings*, Vol. 1218, (1990), pp. 205-214.
12. S. B. Alexander, "Design of wide-band optical heterodyne balanced mixer receivers," *J. Lightwave Tech.*, Vol. LT-5, No. 4, 523-537 (1987).
13. G.L. Abbas et al., "A dual-detector optical heterodyne receiver for local oscillator noise suppression," *J. Lightwave Tech.*, Vol. LT-3, No. 5, 1110-1122 (1985).
14. E.A. Swanson et al., "Optical spatial tracking using coherent detection in the pupil plane," *Applied Optics*, Vol. 28, No. 18, 3918-3928, (1989).
15. D.J. Bernays et al., "Wideband heterodyne spatial tracking for optical space communications," MIT Lincoln Laboratory, Lexington, Mass. Technical Report TR-910, (8 February 1991).
16. K.A. Winick, "Cramer-Rao lower bounds on the performance of CCD optical position estimators," *Optical Society of America A3*, 1809-1815, (1986).
17. D.F. McDonough (memo 1986).
18. D.F. McDonough (memo, 1988).
19. K.A. Winick (memo, 1986).

20. E.P. Colagiuri (memo, 1987).
21. M.M. Blouke et al., "Large format, high resolution image sensors," *Opt. Eng.* 26(9), 837-843 (1987).
22. R.W. Leach, "Optimizing charge-coupled-device detector operation for optical astronomy," *Opt. Eng.* 26(10), 1061-1066 (1987).
23. W.H. McGonagle, private conversation.
24. E.P. Colagiuri (memo, 1986).
25. E.P. Colagiuri (memo, 1986).
26. K.A. Winick (memo, 1985).
27. J.M. Wozencraft and I.M. Jacobs, *Principles of Engineering*, New York: Wiley (1965) p. 83.
28. J.E. Kaufmann, private communication.
29. P.M. Epperson et al., "Electro-optical characterization of the Tektronix TK512M-011 charge-coupled device," *Opt. Eng.* 26(8), 715-723 (1987).
30. J.L. Massey, "The statistical significance of error probability as determined from decoding simulations for long codes," in *Proc. Modelling and Simulation*, Vol. 7, eds. W.G. Vogt, and M.H. Mickle, University of Pittsburgh, ISA (1976).
31. R.J. Parr (memo, 1989).
32. D.M. Hodson (memo, 1988).
33. J.E. Kaufmann (memo, 1989).
34. J.E. Kaufmann (memo, 1989).
35. S.B. Alexander and D. Welford, "Equalization of semiconductor diode laser frequency modulation with a passive network," *Elect. Lett.*, Vol. 21, No. 9, 361-362 (1985).
36. K.A. Winick and P. Kumar, "Spatial mode matching efficiencies for heterodyned GaAlAs semiconductor lasers," *Lightwave Tech.*, Vol. 6, No. 4, 513-520 (1988).
37. D.M. Hodson (memo, 1988).
38. J.E. Kaufmann (memo, 1989).
39. G.M. Carter (memo, 1980).
40. D.J. Bernays and G.M. Carter (memo, 1988).
41. J.R. Janesick et al., "Potential of CCDs for UV and x-ray plasma diagnostics," *Rev. Sci. Instrum.* 56, 796 (1985).
42. M.C. Peckerar, D.H. McCann, and L. Yu, "X-ray imaging with a charge-coupled device fabricated on a high resistivity silicon substrate," *Appl. Phys. Lett.* 39, 1 (1981).

43. J.R. Janesick et al., "Scientific charge-coupled devices," *Opt. Eng.* 26(8), 692-714 (1987).
44. K.P. Klaasen, M.C. Clary, and J. R. Janesick, "Charge-coupled device television camera for NASA's Galileo mission to Jupiter," *Opt. Eng.* 23(3), 334-342 (1984).
45. J.R. Janesick, J. Hyneczek, and M.M. Blouke, "Virtual phase imager for Galileo," in *Solid State Imagers for Astronomy*, J.C. Geary and D.W. Latham, eds., *Proc. SPIE 290*, pp. 165-173 (1981).
46. H.U. Keller et al., "Giotto multicolour camera," European Space Agency SP-1077, 149 (1986).
47. M.M. Blouke, J.R. Janesick, J.E. Hall, J.W. Cowens, and P.J. May, "800 × 800 charge-coupled device imager sensor," *Opt. Eng.* 22(5), 607-614 (1983).
48. J. Kristian and M. Blouke, "Microelectronics in astronomy," *Sci.Am.* 247(4), 48 (1982).
49. W.L. Wang, L.R. Hudson, and H.F. Tseng, "High performance visible and near-infrared charge-coupled-device array for spectroscopy applications," *Opt. Eng.* 26(9), 884-851 (1987).
50. P.M. Epperson et al., "Electro-optical characterization of the Tektronix TK512M-011 charge-coupled device," *Opt. Eng.* 26(8), 715-723 (1987).
51. J.R. Janesick, K.P. Klaasen, and T. Elliott, "Charge-coupled-device charge-collection efficiency and the photon-transfer technique," *Opt. Eng.* 26(10), 972-980 (1987).

# REPORT DOCUMENTATION PAGE

*Form Approved*  
OMB No. 0704-0188

Public reporting burden for this collection of information is estimated to average 1 hour per response, including the time for reviewing instructions, searching existing data sources, gathering and maintaining the data needed, and completing and reviewing the collection of information. Send comments regarding this burden estimate or any other aspect of this collection of information, including suggestions for reducing this burden, to Washington Headquarters Services, Directorate for Information Operations and Reports, 1215 Jefferson Davis Highway, Suite 1204, Arlington, VA 22202-4302, and to the Office of Management and Budget, Paperwork Reduction Project (0704-0188), Washington, DC 20503.

1. AGENCY USE ONLY (Leave blank)	2. REPORT DATE 3 December 1991	3. REPORT TYPE AND DATES COVERED Technical Report	
4. TITLE AND SUBTITLE  An Experimental Spatial Acquisition and Tracking System for Optical Intersatellite Crosslinks		5. FUNDING NUMBERS  C — F19628-90-C-0002 PE — 63789F, 33110F PR — 270	
6. AUTHOR(S)  D.J. Bernays and E.P. Colagiuri-Cafarelli		8. PERFORMING ORGANIZATION REPORT NUMBER  TR-923	
7. PERFORMING ORGANIZATION NAME(S) AND ADDRESS(ES)  Lincoln Laboratory, MIT P.O. Box 73 Lexington, MA 02173-9108		10. SPONSORING/MONITORING AGENCY REPORT NUMBER  ESD-TR-91-090	
9. SPONSORING/MONITORING AGENCY NAME(S) AND ADDRESS(ES)  PL/SWC Kirtland AFB, New Mexico		11. SUPPLEMENTARY NOTES  None	
12a. DISTRIBUTION/AVAILABILITY STATEMENT  Approved for public release; distribution is unlimited		12b. DISTRIBUTION CODE	
13. ABSTRACT (Maximum 200 words)  <p style="text-align: center;">Optical intersatellite communications crosslinks will operate with much higher antenna gains and hence more stringent pointing and tracking requirements than do present RF and microwave-based systems. The design and experimental demonstration of an optical heterodyne communications receiver that includes an integrated 2-axis spatial acquisition subsystem and heterodyne tracker are presented. Requirements for the acquisition and tracking system are derived from the Laser Intersatellite Transmission Experiment (LITE). The acquisition subsystem employs a parallel search algorithm using a direct detection, charge-coupled device (CCD) array. The heterodyne spatial tracker is based upon angle detection in the pupil plane. It uses a commutating, correlation demodulation scheme to reduce front-end-noise-induced biases relative to those from square law detection in the track channel alone. A robust handoff algorithm is presented for the transition between CCD-based acquisition and heterodyne spatial tracking. Results from a laboratory demonstration system are presented.</p>			
14. SUBJECT TERMS heterodyne tracker acquisition and tracking pupil plane CCD		optical communications spatial acquisition satellite communications	15. NUMBER OF PAGES 140
17. SECURITY CLASSIFICATION OF REPORT Unclassified		18. SECURITY CLASSIFICATION OF THIS PAGE Unclassified	16. PRICE CODE
17. SECURITY CLASSIFICATION OF REPORT Unclassified		19. SECURITY CLASSIFICATION OF ABSTRACT Unclassified	20. LIMITATION OF ABSTRACT SAR